DISSERTATION

AEROSOL AND LAND SURFACE IMPACTS ON TROPICAL CONVECTIVE PROCESSES

Submitted by

Gabrielle R. Leung

Department of Atmospheric Science

In partial fulfillment of the requirements

For the Degree of Doctor of Philosophy

Colorado State University

Fort Collins, Colorado

Summer 2025

Doctoral Committee:

Advisor: Susan C. van den Heever

Sonia M. Kreidenweis
Shantanu Jathar
Steven D. Miller

ABSTRACT

AEROSOL AND LAND SURFACE IMPACTS ON TROPICAL CONVECTIVE PROCESSES

In this three-part dissertation, we investigate the dynamical and microphysical processes that determine how tropical convective clouds respond to changes in aerosols and land surface properties. We focus on the variability in such processes across thermodynamic environments and cloud types. Using a combination of large eddy simulations (LES), long-term satellite observations, and Lagrangian object-tracking, we explore the physical mechanisms underlying these interactions.

First, we investigate how aerosol–cloud–precipitation interactions influence convective transport and aerosol removal. We run a suite of sixteen LES with varying aerosol loadings and chemical compositions using the Regional Atmospheric Modeling System (RAMS). We find that increasing aerosol loading leads to increased convective transport of aerosol to the mid-troposphere and decreased aerosol removal through rainout. This means that in more polluted environments, not only is the aerosol loading larger than in pristine environments, but clouds are less able to regulate aerosol loadings via rainout. We further use *tobac* (tracking and object-based analysis of clouds), a cloud object-tracking algorithm, to explore shifts in the cloud population as a function of aerosol loading and type. We describe contrasting aerosol effects on rainfall from shallow cumulus and congestus clouds, leading to non-monotonic trends in domain rainfall. Decomposing these trends into cloud type-specific effects highlights the utility of Lagrangian approaches in elucidating processes driving varied aerosol–cloud interactions.

Second, we explore the impact of widespread anthropogenically driven deforestation on cloud properties in the tropics. We use two decades of satellite data and statistical attribution methods to demonstrate that long-term deforestation in Southeast Asia robustly alters cloud properties. We also provide the first observational evidence that the magnitude of the cloud response to deforestation depends on the atmospheric environment, specifically on moisture and aerosol loading. These results emphasize that regional differences in climatology must be considered when assessing deforestation impacts on clouds and the climate system.

Finally, we investigate the mechanisms driving land surface–cloud interactions using LES and cloud object-tracking. We conduct two sets of simulations over Borneo with identical atmospheric initial and boundary conditions but differing land cover to explore how land surface changes impact convection. We discuss how conversion of tropical forests to palm oil plantations influences the surface energy budget, driving robust decreases in sensible heat flux but enhanced evapotranspiration. We identify and track tens of thousands of clouds and show deforestation decreases region-wide shallow cloud cover but enhances cloudiness along deforestation boundaries via mesoscale vegetation breezes. We also discuss deforestation-driven changes to the sea breeze, deep convection, and precipitation. Our results demonstrate that shallow and deep convection are coupled to the surface through processes acting on different spatiotemporal scales. These findings emphasize that deforestation impacts vary spatially as well as diurnally.

The research in this dissertation has advanced our understanding of the physical processes driving land–aerosol–cloud interactions and quantified how cloud populations shift in response to aerosol and land cover changes. Moreover, we have assessed when and where these shifts are the greatest and thus where perturbations to the aerosol environment and the land surface have the most significant impact for clouds, precipitation, and the broader Earth system.

ACKNOWLEDGEMENTS

There are many people who have helped me on the path to getting my Ph.D. I want to start with acknowledging Dr. Gemma Narisma (†), without whom I would have never embarked on this journey. Gemma was one of my earliest research mentors, and was one of the most brilliant and compassionate scientists I have ever known. She showed me there was a place for me in science—and if there wasn't, that I could make one for myself. I wish she were here today, but I know that she lives on in the work of the many scientists whose lives she has touched.

The biggest thanks are due to my advisor, Dr. Sue van den Heever. Sue has been, in her own words, my biggest critic and my biggest cheerleader. I am so grateful for all she has taught me about what the scientific community knows about clouds (and maybe more importantly, what we *don't* know yet) and what it means to do science well.

Thank you to the members of my doctoral committee: Dr. Sonia Kreidenweis, Dr. Shantanu Jathar, and Dr. Steve Miller, who have been generous with their support, expertise, and time. I am so lucky to come out of every meeting with them full of energy and new questions.

I thank all my co-authors for their valuable contributions to the papers that comprise this dissertation: Dr. Sue van den Heever, Dr. Sean Freeman, Dr. Alex Sokolowsky, Steve Saleeby, and Dr. Leah Grant.

The van den Heever group's tough questions and equally firm support have made me the scientist I am today. This is a very long list, but I thank each and every one of you for your insight and companionship: Dr. Alex Sokolowsky, Dr. Aryeh Drager, Ben Ascher, Dr. Bowen Pan, Dr. Brenda Dolan, Charles Davis, Christine Neumaier, Dr. Emily Riley Dellaripa, Dr. IT Singh, Dr. Jennie Bukowski, Kristen van Valkenberg, Dr. Leah Grant, Dr. Minnie Park, Dr. Nick

Falk, Phoebe Lin, Dr. Peter Marinescu, Rachael Auth, Dr. Randy Chase, Dr. Rick Schulte, Dr. Sean Freeman, Steve Saleeby, and Dr. Yasutaka Murakami.

I'm fortunate that field campaigns have made up a big part of my grad school experience: thank you to the science teams of NASA Cloud, Aerosol, and Monsoon Processes Philippines Experiment (CAMP^{2}Ex), NSF BioAerosols and Convective Storms (BACS), and NASA Testing INCUS Methods Experiment – Suborbital preLaunch Investigations of Convective Evolution (TIME-SLICE). I especially thank Leah and Sean for their trust and mentorship as I learned the ropes of being an operations manager during BACS. I also thank Sue and the rest of the NASA INCUS science team for letting me get involved with INCUS as a grad student. Seeing INCUS come together has been inspiring; I am even more excited to see the great research that comes out of this mission in the years to come.

I am incredibly indebted to the CSU Atmospheric Science front office staff. I especially want to thank Noel Bryan, Dinara Khakimova, Sam Reynolds, Heidi Hammond, Amanda Davey, Nate Gronlund, and Sarah Tisdale, who have helped solve every crisis, from complicated international conference travel to urgent field campaign purchasing and beyond.

Dr. Obie Cambaliza invited me to do research with her all the way back in 2015. I thank her for giving me my first chance to do science, for ten (!) years of support, and for still making time to get dinner whenever I'm in town.

My friends at CSU—Marc, Allie, Charles, Sean, Minnie, Alex, Jennie, Lilly, Chloe, Emily, Ann Casey, Nick, and many more I don't have space to mention—ensured grad school was full of adventures, karaoke, and joy (and not just banging my head against Fortran code).

The Fort Collins Pottery Studio keeps me sane.

My friends back home, especially Martina and Oey, always made time for middle-of-the-night phone calls and put up with my often-slow responses whenever I was in the field or had my head in the clouds (ha!).

My dad (JP), my grandparents (Tami, Nelson, and Nita), and my brothers (Mao, Tobi, and Tommy) have supported me and cheered me on from oceans and continents away. To my dad, JP, I'm finally a doctor! Admittedly, I'm still not the kind that is useful in an emergency—unless the emergency is that you need someone to identify a picture of a cloud, which I will gladly do for you any time.

Finally, endless thanks to my partner, Miguel Hilario, the calm to my never-ending panic. His love makes me both a better scientist and a better person. Miguel: from Quezon City to Clark to Fort Collins to Tucson to Pituffik, Greenland to Nunn, Colorado and to all the places this life takes us next—I'll be there.

My graduate work was supported by NASA through the Future Investigators in NASA Earth and Space Science and Technology program (80NSSC22K1446), the CAMP^{2}Ex field project (80NSSC18K0149), and the INCUS satellite mission (80LARC22DA011). My summers on BACS were supported by the NSF (AGS-2105938). Computing resources supporting the work in Chapter 2 and 4 were provided by the NASA High-End Computing (HEC) Program through the NASA Advances Supercomputing (NAS) division at Ames Research Center. This research has also benefited greatly from the generous work of open-source package developers, including but not limited to: pandas, xarray, dask, jug, scipy, cartopy, metpy, satpy, and *tobac*.

TABLE OF CONTENTS

ABSTRACT ii

ACKNOWLEDGEMENTS iv

Chapter 1: Introduction 1

1.1 Tropical convection 1

1.2 Aerosol–cloud interactions 3

1.3 Land surface impacts on convection 4

1.4 Dissertation overview 6

Chapter 2: Aerosol–Cloud Impacts on Aerosol Detrainment and Rainout in Shallow Maritime Tropical Clouds 8

2.1 Introduction 8

2.2 Model description and analysis approach 10

2.2.1 Model description and configuration 10

2.2.2 Experiment set-up 12

2.2.3 Cloud identification and tracking 13

2.3 Aerosol impacts on domain properties 15

2.3.1 Domain-wide aerosol budget 15

2.3.2 Cloud and rain microphysics 18

2.4 Aerosol impacts on cloud population distributions 20

2.4.1 Trends in cloud numbers and median cloud properties 20

2.4.2 Shifts in cloud population distribution 21

2.5 Influence of aerosol type 24

2.6 Summary and discussion 26
2.7 Tables 30
2.8 Figures 32
Chapter 3: Deforestation-Driven Increases in Shallow Clouds are Greatest in Drier, Low-Aerosol Regions of Southeast Asia 40
3.1 Introduction 40
3.2 Data and Methods 43
3.3 Results 44
3.3.1 Estimated cloud response to deforestation 44
3.3.2 Modulation by precipitable water 46
3.3.3 Modulation by aerosol optical depth 47
3.4 Conclusions 48
3.5 Figures 51
Chapter 4: Deforestation Impacts on Clouds and Precipitation Over Borneo Vary Across the Diurnal Cycle 54
4.1 Introduction 54
4.2 Methods 56
4.2.1 Model description and configuration 56
4.2.2 Experiment set-up 58
4.2.3 Cloud object identification and tracking 59
4.3 Deforestation impacts on the surface energy budget 60
4.4 Cloud responses to deforestation 63
4.4.1 Overview of cloud evolution 63

4.4.2 Mean shallow cloud responses 63
4.4.3 The role of mesoscale circulations 64
4.4.4 Impacts to sea breeze and deep convection 65
4.5 Implications for precipitation 66
4.6 Conclusions 67
4.7 Tables 71
4.8 Figures 72
Chapter 5: Conclusions 83
5.1 Summary and implications of key findings 83
5.2 Future work 85
References 89
Appendix 1: Supplemental Figures for Chapter 2 103
Appendix 2: Supporting Information for Chapter 3 105
A2.1 Detailed methods 105
A2.1.1 Data sources 105
A2.1.2 “Difference-in-differences” statistical analysis 106
A2.1.3 Environmental analysis 108
A2.2 Supplemental figures 109

CHAPTER 1: INTRODUCTION

1.1 Tropical convection

Convective clouds are ubiquitous across much of the Earth's surface, particularly in the tropics (Houze Jr. et al., 2015). At the most basic level, convective clouds are simple: their life begins as warm, moist, and buoyant air from near the surface is transported upwards. The air parcel cools as it is lifted until water vapor condenses into liquid droplets that reflect light and thus comprise what is visible to the human eye as "cloud". The phase change involved in forming cloud droplets warms the atmosphere through the release of latent energy, which in turn increases the parcel's buoyancy and strengthens the updraft. The parcel thus keeps rising—potentially triggering the formation of ice if it reaches sufficiently cool temperatures—until reaching its level of neutral buoyancy, at which point the cloud ceases to grow vertically and shifts to horizontally detraining air into the environment. There are, obviously, many factors that contribute and hence complicate this basic description of cloud processes but, to first order, the life cycle of all convective clouds proceeds in this general manner.

Despite the same basic physics governing their development, convective clouds span a wide range of sizes and morphologies: from an individual isolated shallow cumulus, to extensive fields of cumuli aligned in cloud streets, to towering cumulus congestus, to deep cumulonimbus thunderstorms with their detraining anvils and updrafts that reach all the way to the tropopause (and sometimes beyond). Different environments tend to produce different cloud morphologies. Decades of work has attempted to quantify how cloud macrophysical properties are impacted by environmental properties like mid-level moisture, convective available potential energy, wind shear, and cloud condensation nuclei/CCN concentrations (dating as far back as e.g., Malkus,

1952; Albrecht, 1989). However, these environment–cloud relationships are often not linear and do not exhibit a one-to-one correspondence. A given environment can support multiple types of convection, often at the same time, with many cloud types coexisting in the same scene. This is the case in the classic trimodal distribution of tropical convection (Johnson et al., 1999).

Understanding what types of cloud ultimately form within a given environment depends on many interlinking processes. There is a delicate balance between how much initial buoyancy thermals have (surface forcing), how much latent heat they release through phase changes (microphysics), how much and what types of hydrometeors they form (hydrometeor loading, cold pool processes), how the cloud absorbs and scatters light (radiation), and even how they interact with environmental air (entrainment) and other clouds forming around them. These processes span many orders of magnitude in spatiotemporal scale and are thus a challenge to both measure and to represent in numerical models.

Despite these challenges, there is a great deal of scientific interest in understanding the processes that govern convection (NASA Decadal Survey, 2017). Tropical convection is important for its controls on the weather experienced by the almost half of the global population living in the tropics (Kummu & Varis, 2011), many of whom rely on rainfall for agriculture and freshwater availability (Rodell et al., 2018). Furthermore, tropical convection is important for vertically mixing the atmosphere (Kuang & Bretherton, 2006; Takayabu et al., 2010) and for driving global circulations like the Hadley cell (Riehl & Malkus, 1958). Finally, a significant fraction of scientific uncertainty regarding climate change lies in understanding how cloud processes respond to a warming climate (Rowell, 2012; Ceppi et al., 2017). A better understanding of convective processes is essential for being able to better parameterize these processes in numerical weather prediction (NWP) models, global climate models (GCMs), and

even in state-of-the art kilometer-scale global models; these parameterizations are crucial for making accurate predictions of convection on both weather and climate timescales (Randall et al., 2019; Villalba-Pradas & Tapiador, 2022; Segura et al., 2025).

The primary goal of this dissertation is to better understand cloud processes in order to assess full extent of human impacts on the Earth system. We focus on two specific anthropogenic perturbations, namely: changes to aerosol emissions and to the land surface. Aerosol–cloud and land surface interactions are among the most uncertain drivers of convection, but changes to these processes may have substantial implications for cloud properties—and subsequently for precipitation, global circulations, and the Earth's energy budget.

1.2 Aerosol–cloud interactions

Aerosols are suspensions of tiny particles (1nm-100μm) in the atmosphere. These particles have a variety of sources ranging from natural (e.g., salt from sea spray, lofted dust, secondary organic aerosol production from biogenic emissions) to anthropogenic sources (e.g., sulfates from transport and industrial emissions). Aerosol particles serving as CCN are essential to cloud formation (Aitken, 1917), and changes to aerosol concentrations, composition, and distribution can thus impact cloud microphysics. To first order, increasing aerosol loadings leads to more, smaller cloud droplets which tends to delay the onset of warm rain processes thereby extending cloud lifetimes (Twomey, 1977; Albrecht, 1989). Furthermore, by scattering or absorbing radiation, aerosols can change the thermodynamic profile of the atmosphere, thus impacting cloud development (Ackerman et al., 2000).

Though some aspects of aerosol–cloud interactions (Rosenfeld et al., 2008; Fan et al., 2016) are indisputable, many of these interactions are still contested, particularly those related to

microphysical feedbacks on convective dynamics (Igel & van den Heever, 2021; Varble et al., 2023). The downstream impacts of these microphysical changes on precipitation processes are also uncertain, appear to depend on spatiotemporal scale (Stier et al., 2024) and may be non-monotonic (Dagan et al., 2017; Liu et al., 2019). As we show in this dissertation, the overall signal of aerosol perturbations on precipitation processes is complex because mean signals are often superpositions of many opposing effects.

Despite the lack of consensus, it is widely accepted that aerosols do impact clouds. It is furthermore important to remember that clouds, in turn, also impact aerosols. Clouds play an important role in vertically transporting boundary layer aerosols into the free troposphere (Cotton et al., 1995; Herbener et al., 2016; Leung & van den Heever, 2022). Furthermore, through the formation of precipitation which scavenges aerosol particles, clouds are also responsible for a substantial fraction of aerosol removal from the atmosphere via rainout / wet deposition (Radke et al., 1980; Kipling et al., 2016).

These two perspectives (aerosol impacts on clouds and cloud impacts on aerosols) have traditionally been considered separately. Comparatively little work has looked at the downstream impacts of aerosol–cloud interactions on the aerosol lifecycle. We explore such feedbacks in Chapter 2 of this dissertation.

1.3 Land surface impacts on convection

The land surface is tightly coupled to the atmosphere through exchanges of energy, moisture, and momentum (Mahmood et al., 2014). These exchanges are governed by numerous different surface properties, including albedo, evaporative resistance, and surface roughness. In the tropics, many of these surface properties have changed extensively as a result of

urbanization, agricultural expansion, and deforestation (D.-H. Kim et al., 2015a; Turubanova et al., 2018; Winkler et al., 2021). These changes impact convective initiation and development by altering the turbulent heat fluxes (sensible and latent heat flux) that generate boundary layer thermals and give surface-driven convective clouds their initial source of lift (Rabin et al., 1990; Gentine et al., 2013). Changes to these surface fluxes also impact the growth and thermodynamic properties of the boundary layer atmosphere; this controls the moisture and stability of the low-level atmosphere in which convection develops (Eltahir & Bras, 1993; Findell & Eltahir, 2003; Cioni & Hohenegger, 2017). In turn, convective responses to land surface perturbations impact the net radiative flux incident on the land surface, which again causes the surface energy budget to be repartitioned (Gentine et al., 2019).

Understanding how land cover change impacts convection is further complicated by the need to consider landscape heterogeneity—changes to the land surface are rarely uniform and often have substantial spatial structure on mesoscales (Zipperer, 1993; de Filho & Metzger, 2006). As a result, a significant proportion of research on convective responses to land cover change has focused on impacts to mesoscale circulations driven by contrast in surface properties, which can provide additional lift and mix background air across land surface types (F. Chen & Avissar, 1994b; Saad et al., 2010; Khanna et al., 2017; J. Chen et al., 2023; Ascher et al., 2025; Falk et al., 2025). Such mesoscale impacts on convection are especially important in the tropics where much convection is driven by mesoscale flows (Yang & Slingo, 2001).

As with aerosol–cloud interactions, the coupling between the land surface and convection incorporates feedbacks from many opposing processes that are in a delicate balance. This has led to disagreement among modeling studies focused on cloud responses to land cover changes (H. G. Takahashi et al., 2010; Tölle et al., 2017; C.-C. Chen et al., 2019), and many challenges in

observationally quantifying and attributing these effects (Durieux et al., 2003; Ten Hoeve et al., 2011). We explore new approaches to untangling this tight coupling and quantifying the net impact of land cover changes on convection in Chapter 3 and 4 of this dissertation.

1.4 Dissertation overview

The broad aim of this dissertation is to improve our process-level understanding of how aerosol and land surface perturbations impact convective clouds in the tropics. There remain many outstanding questions surrounding these topics, most fundamentally: what is the sign and magnitude of the cloud response to changes in aerosol emissions and land use? In this dissertation, we focus on how aerosol–land surface–cloud interactions vary as a function of cloud type (e.g., cloud top height), perturbation properties (e.g., aerosol chemical composition), and environmental conditions (e.g., atmospheric moisture profile). Understanding this variability—particularly the variability driven by microscale, convective-scale, and mesoscale processes that are not adequately resolved in general circulation models (GCMs)—will inform a better conceptual model for such interactions. Such an understanding is essential to being able to better parameterize these processes and represent them in large-scale models, and thus being able to accurately estimate the long-term and global impacts of aerosol and land surface perturbations.

In Chapter 2, we explore aerosol impacts on rainfall from tropical convection across aerosol types and cloud modes. We then discuss subsequent implications for aerosol convective transport and removal processes, including under-appreciated feedback pathways by which high aerosol concentrations can hinder aerosol removal through wet deposition. In Chapter 3, we turn our attention to observationally quantifying deforestation impacts on clouds over Southeast Asia, a major frontier for tropical deforestation. We use two decades of satellite data and statistical

attribution techniques to produce observational estimates for the deforestation impact on clouds, as well as how these signals vary across regions depending on background moisture and aerosol loading. In Chapter 4, we use high-resolution, large-domain simulations to understand the physical mechanisms driving cloud responses to deforestation and the variability in this response across the diurnal cycle. We focus on how shallow and deep convection are coupled to the surface via boundary layer processes and mesoscale processes like vegetation and sea breezes. Finally, Chapter 5 presents a summary of the findings in this dissertation. We discuss the major implications of these results for our scientific understanding of aerosol–land surface–cloud interactions, new questions raised by these findings, and potential avenues for future research.

CHAPTER 2: AEROSOL–CLOUD IMPACTS ON AEROSOL DETRAINMENT AND RAINOUT IN SHALLOW MARITIME TROPICAL CLOUDS[1]

2.1 Introduction

Clouds play an important role in governing the atmospheric aerosol budget through a number of simultaneous processes that transport, modify, and remove aerosols. One example of such a process occurs when aerosols are transported between the boundary layer and the free troposphere in cloud updrafts and downdrafts (Bardakov et al., 2022; G. Chen et al., 2012; Cotton et al., 1995; Engström et al., 2008; Savre, 2021; Twohy et al., 2017). Another such process involves aerosol particles being removed from the free atmosphere and undergoing heterogeneous chemistry when they are activated as cloud condensation nuclei (CCN) or are otherwise intercepted by hydrometeors (i.e. impaction; (Ervens et al., 2018; Feingold & Kreidenweis, 2000; Hegg et al., 2004). Cloud processes near cloud tops and cloud edges may further impact the aerosol budget through the evaporation of hydrometeors, which detrains aerosol particles and impacts aerosol number concentrations and vertical distributions (Herbener et al., 2016; Corr et al., 2016; Leung and van den Heever, 2022). Alternatively, in regions where different microphysical processes are dominant, hydrometeors may grow to become precipitation-sized and fall to the surface, thus removing aerosol particles from the atmosphere via wet deposition (i.e. rainout or washout; Radke et al., 1980; Kipling et al., 2016).

[1] This work, entitled "Aerosol–cloud impacts on aerosol detrainment and rainout in shallow maritime tropical clouds", has been published in *Atmospheric Chemistry and Physics* (Leung et al., 2023).

While clouds transport and remove aerosols, aerosols can in turn influence cloud properties both directly and indirectly. Aerosol particles scatter and/or absorb radiation (direct effect), which can alter cloud development through changes to surface fluxes and atmospheric stability (McCormick and Ludwig, 1967; Atwater, 1970; Kim et al., 2014; Grant and van den Heever, 2014; Lee et al., 2014; Park and van den Heever, 2022; Sokolowsky and Freeman et al., 2022). Aerosol particles have also been found to influence the microphysical properties of clouds (indirect effect), with impacts on cloud lifetimes, cloud types, and the overall cloud fraction (Albrecht, 1989; Tao et al., 2012; Twomey, 1977), as well as precipitation efficiency (Dagan et al., 2015; H. Jiang et al., 2010). Perturbations to the aerosol environment can also drive changes in the atmospheric circulation, with local, regional, and global impacts on cloud regimes (van den Heever et al., 2011; Haywood et al., 2013; Grant and van den Heever, 2014; Kim et al., 2016; Herbert et al., 2021; Williams et al., 2022; Dagan, 2022; Park and van den Heever, 2022; Leung and van den Heever, 2023).

Assessing the overall change to the aerosol budget for a given perturbation to aerosol–cloud interactions is complex. Aerosols may induce changes to clouds and precipitation, however these changes to clouds and precipitation may, in turn, influence the aerosol field, although findings in the literature appear to be mixed. For example, Cui and Carslaw (2006) found that increases in aerosol loading led to decreases in the efficiency of both precipitation and wet scavenging by deep convective clouds. On the other hand, while Lee and Feingold (2010) found similar trends for stratiform clouds, they determined that aerosol loading had only a minor impact on convective precipitation and scavenging efficiencies. Discrepancies such as these are difficult to resolve given the numerous cloud and aerosol processes involved. Furthermore, differences in simulated environment, aerosol type, and cloud types may also influence aerosol–cloud interactions (Altaratz

et al., 2014; Dagan & Stier, 2020; Fan et al., 2009; Glassmeier & Lohmann, 2016; Grant & van den Heever, 2014; Gryspeerdt et al., 2014; van den Heever et al., 2011; J. H. Jiang et al., 2018; Khain et al., 2008). Despite these uncertainties, understanding how aerosol–cloud interactions impact the many processes controlling the aerosol budget—as well as which of those impacts are most relevant for a given cloud scene—is essential for representing realistic aerosol distributions and thus for assessing the ultimate aerosol impacts on weather and climate (Boucher et al., 2013; James M. Haywood & Boucher, 2000; Samset & Myhre, 2011).

In this work, our goal is to examine how aerosol impacts on shallow maritime tropical clouds feed back to the aerosol budget via changes to aerosol rainout and aerosol detrainment. More specifically, we aim to answer the following two questions: (1) how does the proportion of aerosol particles that are rained-out versus those that are detrained aloft change as aerosol loading increases? And (2) how do the changes to the aerosol budget arising from rainout and detrainment vary as a function of aerosol type? We address these questions using a large set of high-resolution simulations of an idealized cloud field under a range of aerosol loadings and types, as described in **Section 2.2**. Trends in domain-wide aerosol budget, cloud properties, and microphysical process rates are presented in **Section 2.3**, while a state-of-the-art cloud-tracking package is used to separate trends among different cloud types in **Section 2.4**. Finally, the role of aerosol type is discussed in greater detail in **Section 2.5**.

2.2 Model description and analysis approach

2.2.1 Model description and configuration

The Regional Atmospheric Modelling System (RAMS; version 6.3.03) is a three-dimensional, non-hydrostatic, cloud-resolving model with a two-moment bin-emulating

microphysics scheme (Cotton et al., 2003; Pielke et al., 1992; Saleeby & van den Heever, 2013). Details of the model grid configuration, initial conditions, and parameter settings are described in **Table 2.1**. The RAMS model configuration used here was identical to that in Leung and van den Heever (2022), though the vertical grid is extended to reach from the surface to ~23 km in altitude. The high horizontal, vertical, and temporal resolution ($\Delta x = 100m$, $\Delta z = 50 - 300m$, $\Delta t = 0.75s$) allowed the model to resolve large turbulent eddies and represent a wide range of convection over the two diurnal cycles (48 hours) that were simulated. The domain was located entirely over the ocean, and the simulation was initialized using a combination of dropsonde observations from the Cloud, Aerosol, and Monsoon Processes Philippines Experiment (CAMP^{2}Ex; Reid et al. 2023) and ECMWF Reanalysis-5 (ERA-5) data as described in Leung and van den Heever (2022). After initialization, the model was allowed to evolve freely without additional large-scale forcing, though the solar insolation varied according to the diurnal cycle. As such, these simulations serve as an idealized representation of the microphysical, dynamical, and radiative processes driving maritime tropical convection.

The aerosol field was initialized homogenously in the horizontal direction at the first model time step but decays exponentially in the vertical direction with a scale height of 7 km. In all simulations, ice-nucleating particles (INPs) were also initialized with concentrations starting at 0.01 particles cm^{-3} at the surface and with the same vertical structure as the aerosol field. Both aerosol–radiation and microphysics–radiation interactions (liquid and ice phase) were included in the simulation. The aerosol budget capabilities in RAMS allowed for the tracking of aerosol number and mass in the following categories: (1) unactivated, (2) in-hydrometeor, (3) regenerated, and (4) wet-deposited or rained-out aerosol (Saleeby & van den Heever, 2013). A schematic depicting the processes governing the exchange between these categories is shown in

Figure 2.1. Upon initialization, all aerosol particles were initially categorized as unactivated aerosol, i.e. aerosol particles which have not yet been activated in cloud droplets. Over time, the aerosol number and mass concentration fields changed freely as particles were advected around the domain. If the aerosol particles were entrained into an updraft and encountered sufficient supersaturations to activate and serve as CCN and/or INPs, they were transferred to the in-cloud aerosol category. As water mass was transferred between hydrometeor species (i.e. cloud, drizzle, rain, ice, snow, aggregates, hail, graupel), a corresponding fraction of aerosol was also transferred. Under subsaturated conditions, the hydrometeors evaporated, and the aerosol particles acting as CCN and/or INPs were returned to the environment as regenerated aerosol. Finally, if aerosol particles were contained within raindrops which fell to the ground (either because they were activated as CCN or because they were intercepted by a hydrometeor), they were transferred to a category tracking the accumulated aerosol mass reaching the surface via wet deposition or rainout.

2.2.2 Experiment set-up

The full set of simulations presented here consists of 16 simulations in which four aerosol loadings and four aerosol types were varied (**Table 2.2**). The four aerosol loadings tested span the observed range of aerosol loadings during the CAMP^{2}Ex field campaign, from clean to highly polluted environments (Reid et al., 2022). Throughout the rest of this paper, the different aerosol loading runs are denoted by the initial aerosol number concentration at the surface (which was also the maximum aerosol number concentration initialized in each column), namely 100, 500, 1000, and 1500 cm^{-3}. The four aerosol types tested were ammonium sulfate, sea salt, mineral dust, and absorbing carbon. These aerosol types have varying median particle sizes,

solubility and hygroscopicity, and radiative properties. The aerosol size distribution was represented as a single log-normal mode with a shape factor of 1.8 (Reid et al., 2022), with the median particle size depending on the aerosol type as specified in **Table 2.2**. Other key properties of the different aerosol types are also listed in **Table 2.2**, and corresponding aerosol optical depths (AODs) are provided in **Figure S2.1**.

2.2.3 Cloud identification and tracking

Individual cloud updrafts in each simulation were identified and tracked using the Tracking and Object-Based Analysis of Clouds (*tobac* version 1.5.0 release candidate 1) package (Heikenfeld et al., 2019; Sokolowsky and Freeman et al., 2022). We provide a basic description of how *tobac* works (feature identification, tracking, and segmentation), but for a more comprehensive description, we direct readers to the two papers cited above. We use the term "feature" to refer to an updraft region at a given time step, and "cell" to refer to a given cloud feature tracked across time. First, updraft features were identified at each analysis time step (at a frequency of 5 minutes) based on the three-dimensional vertical velocity field. Regions of local maximum vertical velocity were identified as features at three threshold values (1, 3, and 5 m s^{-1}), and a centroid position was assigned to each feature. Secondly, features in subsequent time steps were linked based on their inferred motion to create a cell with a trajectory over time. Any cells which had a lifetime of less than 5 minutes (i.e. cells which were tracked for only a single analysis time step) were excluded from the analysis as part of the quality control (QC). Finally, a contiguous three-dimensional cloudy region (where cloud condensate was above 0.01 g kg^{-1}) was identified around each updraft feature using the *tobac* watershed segmentation technique. We excluded any updraft features that were not associated with a cloudy region as part of the QC.

Cloud top and base altitudes, as well as cloud areas and volumes, were calculated based on the size of this cloudy region. Similar segmentation was performed on the two-dimensional surface precipitation and aerosol rainout rates in order to identify the size of the raining and/or rainout area associated with each cloud. Based on these identified features and cells, the mean and maximum values for variables such as rain rate, aerosol rainout rate, and updraft velocity were calculated for each cloud over a given time step and over its entire lifetime. Other studies have used previous versions of *tobac* to effectively track cloud objects in a similar manner (e.g. Marinescu et al., 2021), but recent improvements to *tobac* (Sokolowsky and Freeman et al., 2022) have specifically allowed for cloud objects to be identified and tracked in three dimensions and across periodic boundaries, as was necessary for this study.

It should be noted that, in this work, we are tracking on updrafts, meaning that clouds at the very beginning or end of their life cycles with updrafts weaker than 1 m s^{-1} are necessarily excluded from the analysis. This is a limitation of tracking packages that use a physically informed threshold to detect features; however, since *tobac* allows for setting multiple thresholds, we have set a fairly low minimum threshold in order to capture the majority of the cloud lifetime. Although there are numerous updrafts with maximum vertical velocities below 1 m s^{-1} present in the simulation, we found that such weak updrafts do not contribute significantly to the precipitation or aerosol budget, accounting for less than 2% of precipitation and aerosol rainout. Furthermore, after applying all our QC thresholds, we found that a vast majority of the falling-rain and rained-out aerosol (75-80%) could be attributed to the remaining features and that this was consistent across all these simulations.

2.3 Aerosol impacts on domain properties

In this section, we examine the differences in domain-wide properties as a function of aerosol loading and type. Qualitatively similar cloud fields develop in all 16 simulations (**Figure S2.1**), consisting primarily of shallow cumulus (with cloud tops ~2-4 km a.g.l.) and congestus (with cloud tops ~4-7 km a.g.l.). Clouds begin to form in the simulations after 6-7 hours and the cloud field develops a variety of cloud morphology and degrees of organization over the next 48 hours (e.g., linear groups, scattered or isolated clouds, arc clouds associated with cold pools). Deep convection (with cloud tops >7 km a.g.l.) occurs only sporadically in a handful of the simulations and does not persist in any of them. An example of the cloud scenes typically simulated is shown in **Figure 2.2**.

2.3.1 Domain-wide aerosol budget

The domain-wide trends in the aerosol mass budget are presented in **Figure 2.3**. For each simulation, we integrate the amount of aerosol mass in each of the four budget categories (namely unactivated, in-hydrometeor, regenerated, and rained-out) after 48 hours of simulation time, and then we normalize this mass by the total initial mass at the beginning of the model run. In this manner, we quantify the percentage of aerosol mass that is apportioned to each budget category, thus providing a fairer comparison between simulations of different initial aerosol loading. If changes to the aerosol loading have no impacts on the cloud field and cloud processes impacting aerosol particles, then we would expect the same distribution of aerosol mass across the budget categories, irrespective of aerosol loading. We have chosen here to present an aerosol mass budget rather than a number budget, since aerosol mass is conserved after activation and subsequent regeneration of aerosol particles whereas all aerosol number is not conserved when

multiple aerosol particles are collected by a single hydrometeor (i.e. it is assumed that interstitial aerosol particles that are collected by a droplet cohere with the original activated particle). Considering aerosol mass therefore allows us to specifically account for all the transfers between aerosol budget categories. Over the course of the simulation, we found that less than 5% of the aerosol mass is not tracked and is treated as a residual that is lost due to dry deposition (which is represented in RAMS, but not tracked in the RAMS aerosol budget) and/or numerical diffusion; this residual proportion is very similar across all our simulations (**Figure S2.2)**.

Across all the simulations about half of the initial aerosol mass serves as CCN at some point in time, while the other half remains unactivated (**Figure 2.3a**) for the duration of the simulation. As aerosol loading increases, the fraction of unactivated aerosol generally decreases (the fraction of activated aerosol increases), though changes are fairly small compared to the trends in the other aerosol budget categories. At first glance, this appears to contradict classic cloud parcel theory, wherein the activated fraction decreases (unactivated fraction increases) as aerosol number concentration goes up for a given updraft speed (Reutter et al., 2009). In this scenario, the increased CCN number concentrations lead to increases in cloud droplets competing to consume the available supersaturation. Thus, that parcel's maximum supersaturation is lower compared to a parcel with fewer aerosol particles and an identical updraft speed, and it is therefore unable to activate the smallest aerosol particles, which subsequently drives down the activated aerosol fraction. However, it is important to note that the results we present in **Figure 2.3** are not from a single cloud parcel, but rather are integrated over the whole cloud field and therefore incorporate any aerosol effects that lead to changes in the updraft speed, ambient relative humidity, and cloud types. We discuss these changes to the broader cloud population in greater detail in **Sect. 2.4**. There is also a slight decrease in the

aerosol mass found inside cloud droplets or embedded in drizzle or raindrops (**Figure 2.3b**), though the trend is non-monotonic and inconsistent between aerosol types. However, the in-hydrometeor category comprises a relatively small percent of the overall aerosol budget at any given time step and the trends in this category vary temporally (**Figure S2.2**), since aerosol particles are only apportioned to it temporarily before being transferred to the regenerated or rained-out category.

The clearest and most temporally persistent trends in the domain-wide aerosol budget as a function of aerosol loading are seen in the proportion of aerosol mass that is regenerated (**Figure 2.3c**) or rained-out (**Figure 2.3d**). It is clear from these figures that the proportion of regenerated aerosol mass is enhanced, while the proportion of rained-out aerosol mass is decreased with increasing aerosol loading. While **Figure 2.3** shows a snapshot in time, these trends are largely consistent throughout the course of the simulation (full time series shown in **Figure S2.2**). The opposing trends between the increases in regenerated aerosol and decreases in rained-out aerosol with increasing aerosol loading have similar magnitudes and are on the order of 7-10% of the initial aerosol mass. These trends are remarkably consistent with aerosol type, as will be discussed further in **Sect. 2.5**. We emphasize here that the aerosol mass budgets we present are normalized by the initial aerosol loading—in the highest-aerosol-loading case, there is not only a greater absolute mass of aerosol that is regenerated and detrained back into the environment but also actually a larger percentage of mass involved. The changes to rainout, which is the only major aerosol sink in the budget examined here, suggest a positive feedback mechanism by which increases in aerosol loading may actually inhibit the removal of aerosol particles by clouds.

2.3.2 Cloud and rain microphysics

To investigate the mechanisms by which increased aerosol loading leads to aerosol regeneration being favoured over rainout, we examine trends in the cloud and rain droplet size distributions (**Figure 2.4**). For all aerosol types, increasing the aerosol loading produces more numerous and smaller cloud droplets (**Figure 2.4a-b**), which is consistent with the first indirect effect that has been demonstrated in many observational and modelling studies (Tao et al., 2012; Twomey, 1977). On the other hand, increasing aerosol loading produces fewer and larger raindrops (**Figure 2.4c-d**). This effect has been demonstrated in multiple modelling studies (Altaratz et al., 2014; Berg et al., 2008; X. Li et al., 2013; Sheffield et al., 2015) with more limited observational support (Berg et al., 2008; May et al., 2011).

These trends in the droplet size distributions can be more easily connected to the aerosol budget by examining trends in the microphysical process budget, as shown in **Figure 2.5**. Each term in this figure represents a different sink for cloud water and is given as an efficiency relative to the mass of water vapour transferred to liquid in cloud droplets. The value given is the percent of condensed water vapour that ends up in a particular cloud water sink. As aerosol loading increases, the cloud droplets are smaller and thus evaporate more readily (**Figure 2.5a**) and are also less likely to be collected into rainwater (**Figure 2.5b**). This explains the trends in the aerosol budget under increased aerosol loadings to first order: although a similar proportional mass of aerosol particles is activated and enters cloud droplets, those cloud droplets are smaller and tend to evaporate more quickly, which favours regeneration. Simultaneously, those smaller cloud droplets are less likely to be collected as rainwater, and thus the CCN contained within them are less likely to be washed out within precipitation.

In the polluted aerosol environment, although cloud water is less likely to be collected by rain, the cloud water which is collected is distributed among fewer raindrops. These raindrops are thus larger in size (**Figure 2.4d**) and have a lower surface-area-to-volume ratio compared to raindrops that form in pristine aerosol environments, in keeping with past model results (Altaratz et al., 2014; Saleeby et al., 2015; Storer & Heever, 2013). As a result, even though increasing aerosol loading leads to less-efficient collection of cloud water into rainwater, it also leads to decreases in rainwater evaporation (**Figure 2.5c**). These two trends partially offset one another, leading to mixed trends in the percentage of cloud water that falls to the surface as rain (**Figure 2.5d**), sometimes defined as the precipitation efficiency (Cui & Carslaw, 2006; H. Jiang et al., 2010; S.-S. Lee & Feingold, 2010; R. L. Li et al., 2022; Lutsko et al., 2021). These decreases with increasing aerosol loading are not monotonic for all aerosol types, and it is a smaller relative trend compared to those of cloud evaporation and collection. Although increasing the aerosol loading in the domain causes clouds to become less efficient at removing aerosol via rainout (**Figure 2.3d**), it does so without necessarily impacting the precipitation efficiency itself (**Figure 2.5d**). Earlier results by Cui and Carslaw (2006) and Lee and Feingold (2010) showed similar decreases in the aerosol rainout efficiency (or aerosol precipitation efficiency or scavenging efficiency, as they respectively referred to it), but these decreases were closely coupled with decreases in precipitation efficiency. That is to say, they showed that increased aerosol loading caused less-efficient rain formation and therefore less-efficient aerosol removal through rainout. Our results add to this and show that the reduced efficiency in aerosol removal through rainout can occur even without changes to the domain-wide precipitation efficiency.

2.4 Aerosol impacts on cloud population distributions

2.4.1 Trends in cloud numbers and median cloud properties

Given the complexity surrounding the number of processes impacting rain formation, which often have opposing trends as a function of aerosol loading, we find that increasing aerosol loading does not necessarily lead to decreases in precipitation efficiency (**Figure 2.5d**) or the domain-wide accumulated precipitation (**Figure 2.6a**). For some aerosol types (e.g., mineral dust), the increase in aerosol loading actually leads to an increase in the accumulated precipitation between the lowest and highest aerosol loadings tested in our set of simulations. The trends in the total number of tracked clouds are similarly non-monotonic and mixed, as shown in **Figure 2.6b** and suggest that aerosol loading does not have a clear impact on domain cloudiness for these simulations of maritime tropical clouds. That being said, tracking the clouds over their full lifetime with the use of *tobac* allows us to further subdivide clouds into those that precipitate and those which do not (**Figure 2.6c-d**). To differentiate raining and non-raining clouds, we find the area-mean rain rate associated with each cloud feature at each point in its lifetime, and then we take the lifetime maximum of those rain rates such that non-raining clouds are those which never reach an area-mean rain rate of 0.0001 mm hr^{-1}. Clearly, the mixed trend in the total number of clouds as a result of increasing aerosol loading arises as a result of the following two opposing trends: increases in the number of non-precipitating clouds and decreases in the number of precipitating ones. This is, furthermore, consistent with the general picture of aerosol impacts on the cloud field from the process rates, as described above: although clouds still do form in environments with higher aerosol loadings, the cloud droplets evaporate more readily before the cloud is able to produce precipitation-sized particles, and thus a greater fraction of clouds never rain throughout their whole lifetime. Non-raining clouds still activate

aerosol particles and regenerate them aloft as the cloud dissipates, but they do not remove them from the domain via rainout, which contributes to aerosol regeneration at the expense of rainout.

We can use *tobac* to aggregate the raining clouds (**Figure 2.7**) to see how the median properties of these clouds evolve under different aerosol environments. Although increasing aerosol loading leads to fewer raining clouds, those which do rain are invigorated with higher rain rates (**Figure 2.7a**). This is further compounded by the decrease in the median area covered by each raining cloud (**Figure 2.7b**). Overall, we find that under higher aerosol loadings, surface rainfall becomes more concentrated amongst fewer clouds with a higher median rain rate. However, this is contrasted by the trends in aerosol rainout rate (**Figure 2.7c**). The aerosol impact is non-monotonic, but there is a decrease in the strength of aerosol rainout between the lowest and highest aerosol loadings for all aerosol types. We conclude that *the median cloud rains more under higher aerosol loadings but rains out less aerosol.* Shifts in the behaviour of the overall cloud population, as well as potential explanations for this behaviour, are discussed in the following subsection.

2.4.2 Shifts in cloud population distribution

An advantage of cell tracking over prior analysis methods is the ability to examine trends and characteristics of evolving cloud population distributions as opposed to merely aggregating properties. We construct two-dimensional histograms according to cloud top height (CTH) and either rain rate (**Figure 2.8**) or normalized aerosol rainout rate (**Figure 2.9**), such that the value in each bin is the number of raining clouds with a given CTH and rain rate and/or rainout rate. The CTH, rain rate, and normalized aerosol rainout rate are defined by taking the lifetime maximum value for each tracked cloud cell, such that they represent the peak maturity for a

given cloud. This approach has the benefit of being able to separately identify cloud modes according to different CTHs; in this case, the shallow cumulus mode is clearly visible as a hotspot of clouds with CTHs of ~2 km, as is the congestus mode with CTHs of ~4 km (e.g. **Figure 2.8a**) This is particularly important due to our focus on tropical convection, which is known to consist of three separate cloud modes (Johnson et al., 1999; Posselt et al., 2008).

Generally, there is a positive correlation between CTH and precipitation rate, with taller clouds tending to have stronger rain rates than shallower clouds do (Adler & Mack, 1984; Smalley & Rapp, 2020). Moving from left to right in each row in **Figure 2.8** allows one to see the impact of increasing aerosol loadings on the CTH–rain-rate distribution, such that negative values (blue regions) are portions of the cloud population that become less frequent with increasing aerosol loading and vice-versa for positive values (red regions). Notably, increased aerosol loadings impact shallow cumulus and congestus clouds in opposite ways, emphasizing that median cloud properties over all types of clouds are insufficient for quantifying the magnitude of the aerosol effect. Shallow cumulus clouds tend to grow taller, with the modal CTH being closer to 3 km in the highest aerosol simulations, but they do so with reduced rain rates (e.g. **Figure 2.8d**) in a manner that is similar to the precipitation suppression effect described in many past studies (e.g. Xue et al., 2008; Spill et al., 2019). On the other hand, congestus clouds also grow slightly taller but have much stronger modal rain rates, which is consistent with previous findings on the warm-phase invigoration of this tropical-cloud mode (X. Li et al., 2013; Sheffield et al., 2015). These results suggest that the smaller shallow cumulus clouds are more sensitive to the increase in evaporation (**Figure 2.5a**), whereas congestus clouds with larger areas are more able to protect the interior of the cloud core from evaporation, thereby benefitting from the increase in latent heating or warm-phase invigoration associated with

increased cloud droplet formation (**Figure 2.4a**). Furthermore, this shows that the impact of increasing aerosol on precipitation efficiency is dependent on cloud type. This may explain differences between this study and recent studies such as that of Dagan (2022), which saw monotonic increases in precipitation efficiency with increasing aerosol. The latter study used a coarser grid spacing that did not resolve the shallow cumulus cloud field which we find in this work to have decreasing precipitation efficiency with increasing aerosol.

The CTH–aerosol-rainout-rate distribution in **Figure 2.9** clearly shows deeper clouds being associated with more aerosol rainout compared to shallower clouds. This relationship is consistent with trends in rain rate with cloud top height as discussed previously. For shallow cumulus, increased aerosol loading leads to a decrease in their ability to remove aerosol via rainout, which follows closely with the decrease in their rain rates. However, although congestus clouds tend to produce stronger rainfall in higher-aerosol environments, they do not see a corresponding increase in their ability to rainout aerosol, which has no change or even decreases slightly for the highest aerosol loadings. These results suggest that, unlike rain rates, which can be enhanced by warm-phase invigoration, there is something of a saturation effect for rainout. At a certain point, stronger rain rates can no longer increase the amount of aerosol being rained-out since the aerosol available to rainout in those areas has already been removed to the surface. Because the surface rainfall from these clouds becomes concentrated over smaller horizontal areas where the cloud droplets are sufficiently protected from the environment such that they can form precipitation-sized hydrometeors, there are increasing areas of clear-sky or very light precipitation that is not sufficient to remove aerosol particles to the surface. Thus, the overall aerosol impact on rainout is dominated by the decrease in rainout from shallow clouds which either have weaker rain rates or stop raining altogether. These findings provide strong process-

level evidence for a potential mechanism to explain recent results from GCMs showing that frequent, light precipitation is more important than strong precipitation in regulating the amount of wet-deposited aerosols (Y. Wang, Xia, Liu, et al., 2021; Y. Wang, Xia, & Zhang, 2021).

2.5 Influence of aerosol type

We have shown throughout this paper that the influence of aerosol type on the overall aerosol budget and cloud populations is relatively small. Regardless of aerosol type, increasing aerosol loading leads to similar trends in cloud microphysics, precipitation rates, and the domain-wide aerosol budget, varying only in terms of magnitude. The different aerosol median sizes and hygroscopicities (**Table 2.2**) do influence the magnitude of the aerosol rainout, although only minimally, and they do not affect the overall trends. For example, the cloud field overall tends to be more efficient at raining out ammonium sulfate and sea salt (**Figure 2.3d**), both of which have larger particle sizes, which is consistent with these particles having a higher activation fraction all else being equal (Reutter et al., 2009). Note that comparing among the median cloud in each simulation (**Figure 2.7c**) shows lower normalized aerosol rainout rates for ammonium sulfate and sea salt. This is driven by the tail of the distribution shown in **Figure 2.9**—since the clouds are more efficient at raining out ammonium sulfate and sea salt, cumulus clouds with low rainout rates are still able to show appreciable and trackable values. However, the integrated impact of all clouds in the field is more accurately shown in **Figure 2.3d** or by looking at the full distribution in **Figure 2.9**, which emphasizes the importance of evaluating changes across the whole cloud distribution and not merely in medians or means across different cloud modes.

We found that cloud properties depend more strongly on the magnitude of aerosol loading rather than on the aerosol type. The lack of variation in the cloud population distribution as a

function of aerosol type (as can be observed by comparing across each column in **Figure 2.8** and **2.9**) was observed despite the strong differences in clear-sky radiative-heating rates as a function of aerosol type (**Figure 2.10**). The differences in heating rates are driven by differences in the absorbing and scattering properties of each aerosol type, with more scattering aerosol, like ammonium sulfate or sea salt, driving cooling trends with increased aerosol, and more absorbing aerosol, like absorbing carbon and mineral dust, driving warming and stronger stratification of the stable layers in the domain. However, these differences in radiative heating do not appear to feed back on cloud properties within the domain—at least not on the timescales of our simulation (48 hours) — as there is not sufficient time for these differences in direct aerosol effects to influence the overall cloud field. These differences may eventually lead to divergence between aerosol types as the system moves towards radiative–convective equilibrium (RCE), though there is some debate about whether the relatively short lifetimes of these shallow cumulus and congestus clouds allow for such equilibration, and longer-term and realistically forced simulations would be necessary to test this (Dagan et al., 2018). Some past research also suggests that this may be sensitive to the update timescale used for the radiation parameterization (Matsui et al., 2020). We would also expect that the radiative differences between aerosol types would be amplified over a land surface where aerosol-induced differences in the feedbacks to the surface fluxes could play a role; this is in contrast to the ocean surface (here, we have fixed the SST, though we would not expect large aerosol-induced changes in SST over the 48 hours of simulation time, even if a fully interactive ocean surface were utilized).

2.6 Summary and discussion

Aerosol–cloud interactions are a key uncertainty in terms of both the overall climate forcing and weather. They are especially challenging to unravel given the large number of processes and feedbacks involved. Here, we have aimed to examine how aerosol impacts on shallow maritime tropical clouds (cumulus and congestus) subsequently modify the aerosol budget, specifically through the removal of aerosol via rainout versus the regeneration of aerosol particles via detrainment aloft. By combining a suite of high-resolution simulations with a comprehensive apportionment of an aerosol budget facilitated by the *tobac* tracking package, we were able to track both domain-wide trends and the processes driving those trends in different modes of the tropical-cloud population as a function of aerosol loading and aerosol type.

First, we examined trends in the domain-wide aerosol budget and cloud microphysical processes. We found that, regardless of aerosol type, increasing the aerosol loading enhances aerosol regeneration at the expense of rainout. This effectively hinders the cloud field's ability to remove aerosol, and thus represents a positive feedback by which increased aerosol loadings may strengthen with time. The increased aerosol regeneration is driven by a decrease in the size of cloud droplets and thus an increase in evaporation. Cloud droplets are therefore increasingly likely to evaporate before the cloud has the chance to form rain and hence remove aerosol through surface deposition. Although there are fewer raindrops that form, each droplet that does form through stochastic collisions with other droplets then has more cloud water available for collection, since a similar amount of cloud water is being divided among fewer raindrops. As a result, these raindrops can be larger and thus experience less evaporation. Previous work has shown increasing aerosol loadings to be associated with decreases in precipitation efficiency and aerosol rainout efficiency (Cui & Carslaw, 2006; S.-S. Lee & Feingold, 2010)—here, we show

that the decrease in the cloud field's efficiency at removing aerosol via rainout can occur even without a corresponding decrease in the overall precipitation efficiency. In other words, even when clouds produce a similar amount of precipitation under higher aerosol loadings due to compensating changes to cloud and rain microphysics, the ability of clouds to remove aerosol via rainout is still hampered because it depends primarily on changes to cloud water collection. Instead, the aerosol particles are regenerated aloft, where they form an aerosol detrainment layer (or potentially, in the case of multilayer clouds, detrainment layers) that can serve as an aerosol source for future midlevel and multilayer clouds (Leung & van den Heever, 2022).

Additionally, we used *tobac* to track clouds over the course of their lifetime and to generate statistics of cloud properties. We found that increases in aerosol loading lead to more non-raining clouds and fewer raining clouds; this, again, is in keeping with the idea that precipitation is suppressed and that clouds tend to dissipate before they can form rain. Those clouds which do rain tend to have stronger rain rates over a smaller horizontal area, such that precipitation is increasingly concentrated among fewer clouds that are warm-phase invigorated under high-aerosol conditions. Although these clouds then have stronger rain rates, this does not lead to more aerosol rainout overall due to the smaller horizontal area covered by rain leaving a larger clear-sky region where aerosol particles can remain in the atmosphere. This further validates our initial domain-wide analysis showing decreases in aerosol rainout efficiency without changes to precipitation efficiency.

Finally, we examined changes caused by varying aerosol environments as a function of different cloud types and found that a mixed domain-wide trend in rain amounts is driven by contrasting aerosol effects in shallow cumulus and congestus clouds. With increasing aerosol loading, shallow cumulus clouds tend to grow taller and rain less or not at all, whereas congestus

clouds only grow slightly taller and tend to have higher rain rates. These changes in rain intensity lead to shallow cumulus clouds being less able to remove aerosol via rainout. Despite congestus having higher rain rates with increased aerosol, there is a saturation effect, such that the more-intense rain no longer increases the efficiency with which aerosol is rained-out, since the rainfall depletes most of the available aerosol even before the rain rates intensify. As a result, the decreases in shallow cumulus precipitation dominate the aerosol effect on the overall amount of aerosol which is removed by rainout. Furthermore, these results underscore that aerosol–cloud interactions can be highly dependent on cloud type, given that the balance between susceptibility to evaporation and warm-phase invigoration depends on the cloud size and dominant microphysical processes, and ultimately determines the sign of the precipitation response.

In general, we found that the magnitude of aerosol loading tested in our simulations had a stronger impact on aerosol–cloud impacts than did the aerosol type, despite the clear differences in the radiative-heating rates brought about by the latter. We suggest that the differences in the aerosol direct effect between different aerosol types may pose a stronger impact over longer timescales and/or over land surfaces that have more rapid surface flux feedbacks, and we recommend that future work be undertaken to investigate these scenarios. We also caution that, while these results are robust over this set of simulations with varied aerosol environments, the simulated meteorology only captures a particular maritime tropical environment, and the strength of the aerosol budget response may depend on other factors, including the large-scale meteorology. However, the consistent trends in aerosol impacts on the microphysical processes, the whole cloud population distribution, and the domain aerosol budget suggest that the aerosol–cloud interactions described here may be significant. These interactions represent a pathway by which a polluted environment not only has higher aerosol loadings than a pristine one, but is

actually less able to regulate those loadings by removing aerosol—instead, the aerosol is convectively transported from the boundary layer to the free troposphere, where aerosol particles remain available for reactivation and further aerosol–cloud interactions.

2.7 Tables

Table 2.1. RAMS model parameters used in the simulation.

Model aspect	**Setting**
Grid	Arakawa C grid
	1000 x 1000 points, $\Delta x = \Delta y = 100m$
	Centered on 8.75ºN, 119.75ºE
	120 vertical levels, $\Delta z = 50 - 300\ m$
Time integration	48-hour simulation duration, $\Delta t = 0.75s$
	2019-09-16, 00:00:00 UTC, to 2019-09-18, 00:00:00 UTC
Initialization	Horizontally homogenous thermodynamic and wind profile, averaged from ERA-5 and CAMP^{2}Ex dropsonde (between 8-9ºN, 119-120ºE)
	Random potential temperature perturbations within the lowest 500m above ground level (AGL) of the domain, with a maximum perturbation of 0.1K
Surface scheme	All-ocean surface with spatially and temporally uniform sea surface temperature (SST=29ºC)
	Land Ecosystem–Atmosphere Feedback 3 (LEAF-3; Walko et al., 2000)
Boundary conditions	Periodic in zonal and meridional directions
Microphysics scheme	Two-moment bulk microphysics (Meyers et al., 1997)
	Eight hydrometeor classes (Saleeby & Cotton, 2004)
	Heterogeneous ice nucleation (DeMott et al., 2010)
Radiation scheme	Two-stream, hydrometeor sensitive (Harrington, 1997)
	Updated every 5 minutes
	Solar insolation varied with diurnal cycle
Aerosol treatment	Maximum concentration at the surface, exponentially decreasing with altitude with a scale height of 7km
	Aerosol–radiation interactions

	Aerosol sources and sinks, with full aerosol budget tracking (Saleeby and van den Heever 2013)

Table 2.2. Key aerosol parameters for different aerosol types in RAMS. Radiative parameters are given for RH 80%, size bin 14 (particle diameter 0.16 mm), radiation band 3 (visible; 245-700nm, band midpoint 472.5nm).

Aerosol type	**Median particle diameter (μm)**	**Solubility fraction**	**Density (kg m^{-3})**	**Hygroscopicity**	**Qext**	**Qscat**	**SSA**
Ammonium sulfate	0.18	0.9	1857.1	0.651	2.07630	2.01450	0.97
Sea salt	0.2	1	2165	1.334	2.06070	2.06070	1
Absorbing carbon	0.1	0.05	2605.95	0.053	2.08970	1.13680	0.544
Mineral dust	0.1	0.05	2463.45	0.050	2.09050	1.43280	0.685

2.8 Figures

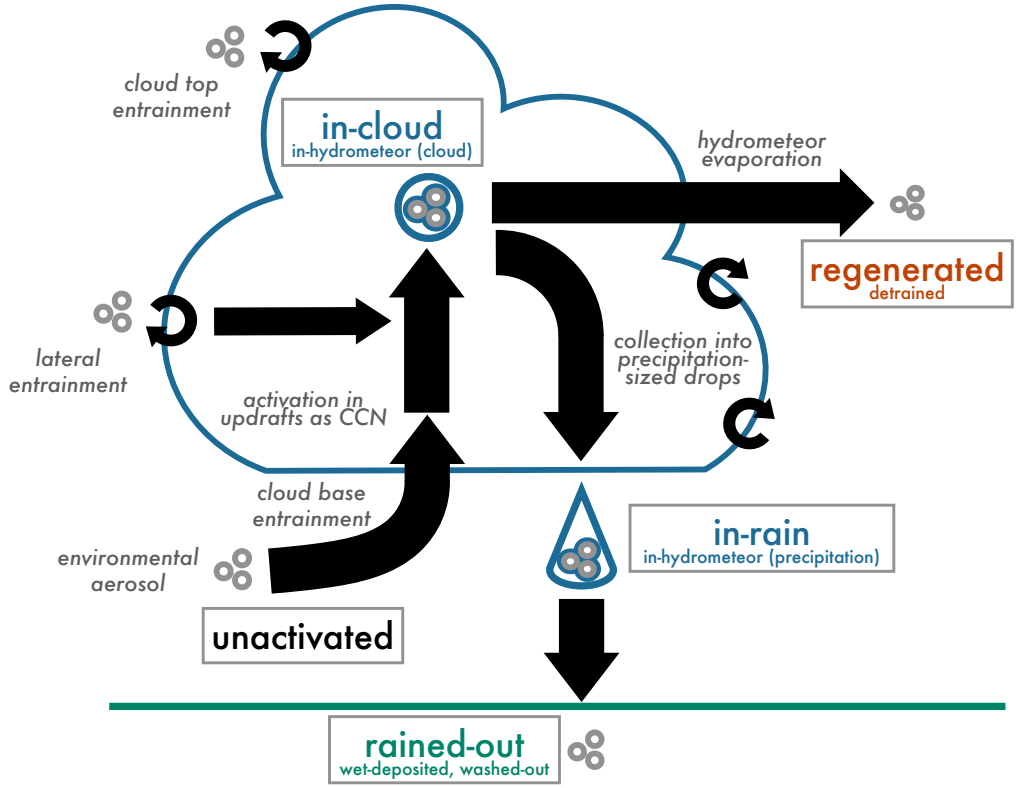

Figure 2.1. Schematic of processes involving aerosol transfer represented in the set of RAMS simulations. The aerosol budget terms described in text are depicted in grey boxes. Black arrows depict the transfer of aerosol number and mass between the different budget terms.

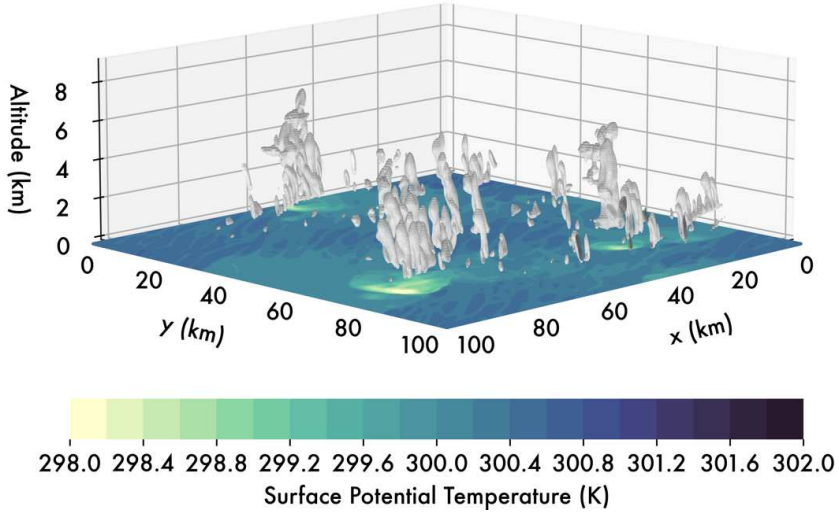

Figure 2.2. Three-dimensional rendering of simulated cloud field at 23:00UTC (7:00 LT) for the control sea salt simulation (initial number concentration of 100 cm^{-3} at the surface). Grey isosurfaces are 0.01 g kg^{-1} of cloud condensate. Surface colours are the potential temperature (K) at the lowest model level above the surface, with lighter colours highlighting the development of cold pools associated with the clouds.

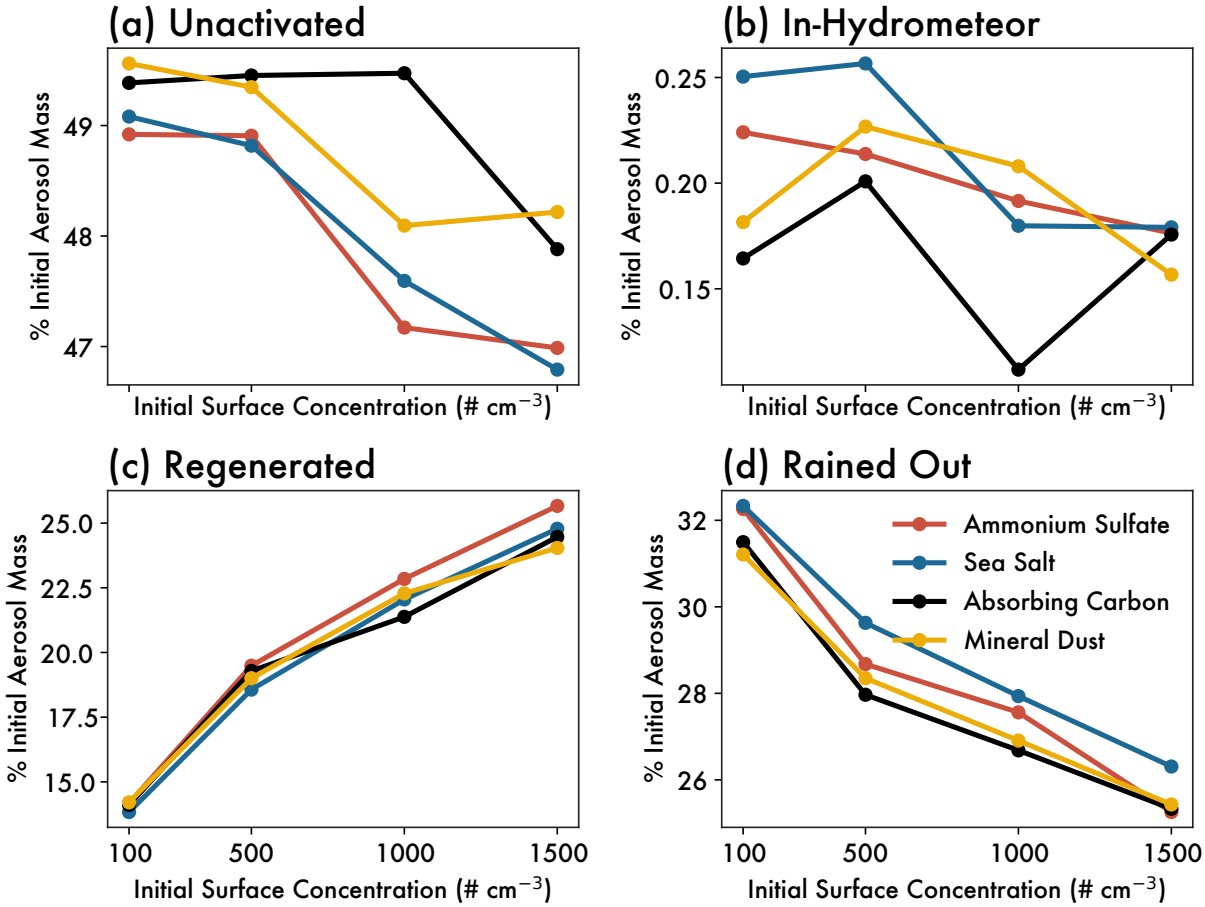

Figure 2.3. Domain aerosol mass budget after 48 hours of simulation time represented as a function of the initial aerosol surface concentration (# cm^{-3}) and aerosol type. Each aerosol budget term is the domain-integrated aerosol mass in a given category normalized by the total aerosol mass at initialization time, shown for (a) unactivated, (b) in-hydrometeor, (c) regenerated, and (d) rained-out aerosol. See the text for explanations of each aerosol category.

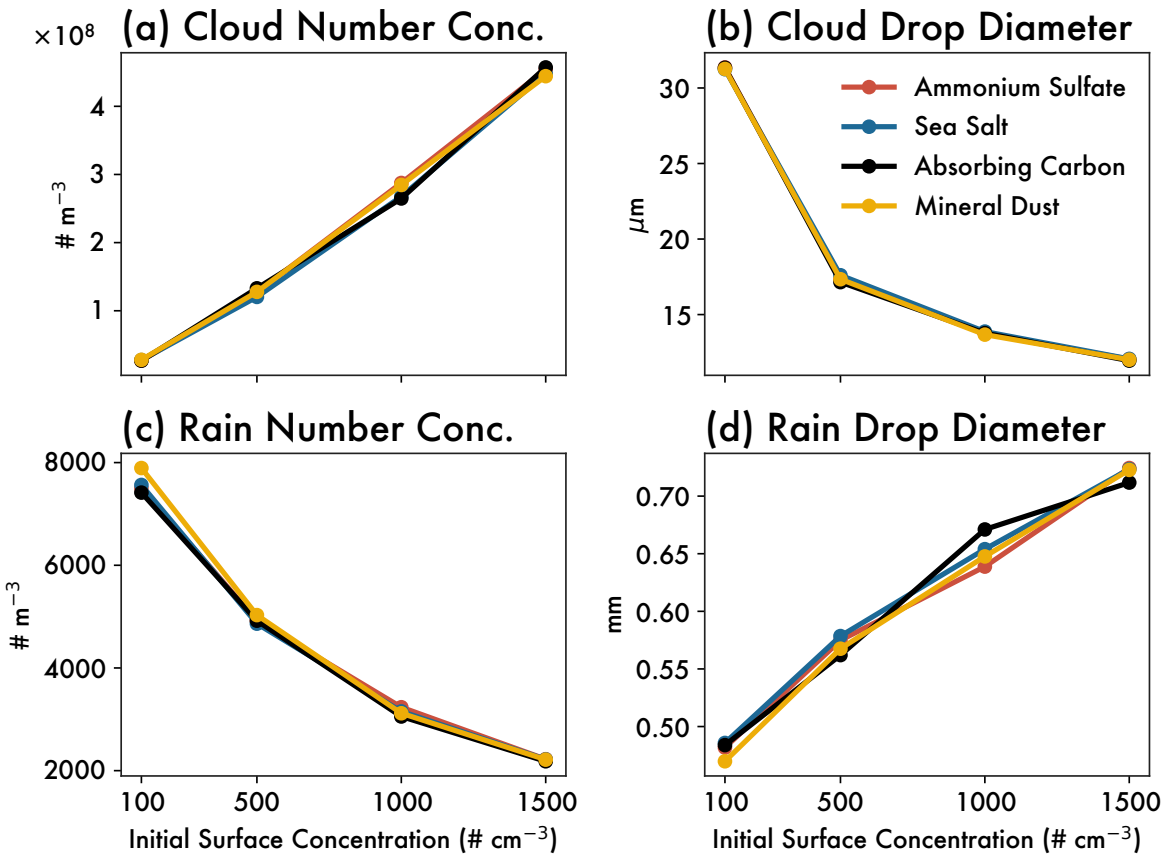

Figure 2.4. In-cloud mean microphysical size distribution properties as a function of initial aerosol surface concentration (# cm^{-3}) and aerosol type: (a) cloud droplet number concentration (# m^{-3}), (b) cloud droplet diameter (μm), (c) rain drop number concentration (# m^{-3}), and (d) rain drop diameter (mm). Values are spatially and temporally averaged over cloudy (cloud condensate > 0.01 g kg^{-1}) updraft (vertical velocity > 1 m s^{-1}) grid points.

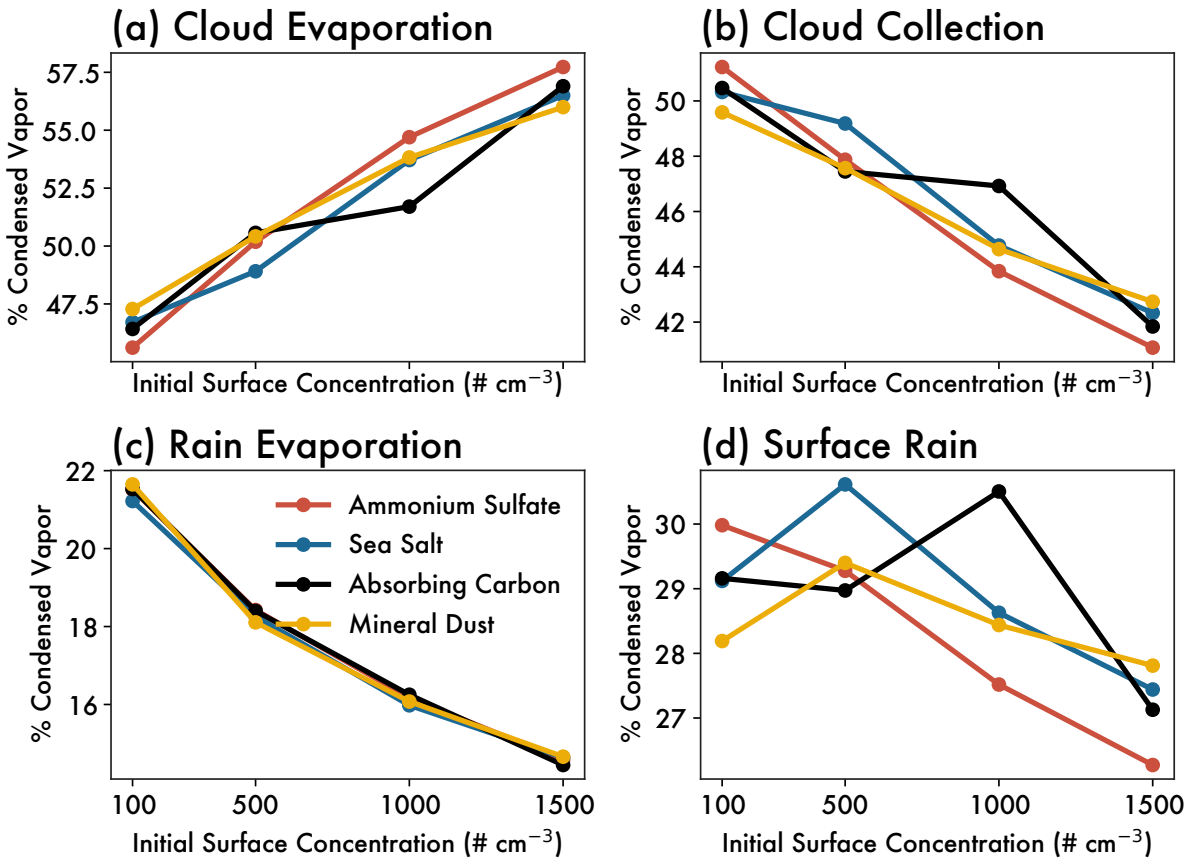

Figure 2.5. Domain total microphysical process rates as a function of initial aerosol surface concentration (# cm^{-3}) and aerosol type. Each panel shows the process efficiency (in %), defined as the domain- and time-integrated process rate normalized by the domain- and time-integrated condensation rate (water vapour to liquid water), shown for (a) cloud water evaporation, (b) cloud water collection into rain, (c) rainwater evaporation, and (d) surface-accumulated rain (i.e. precipitation efficiency).

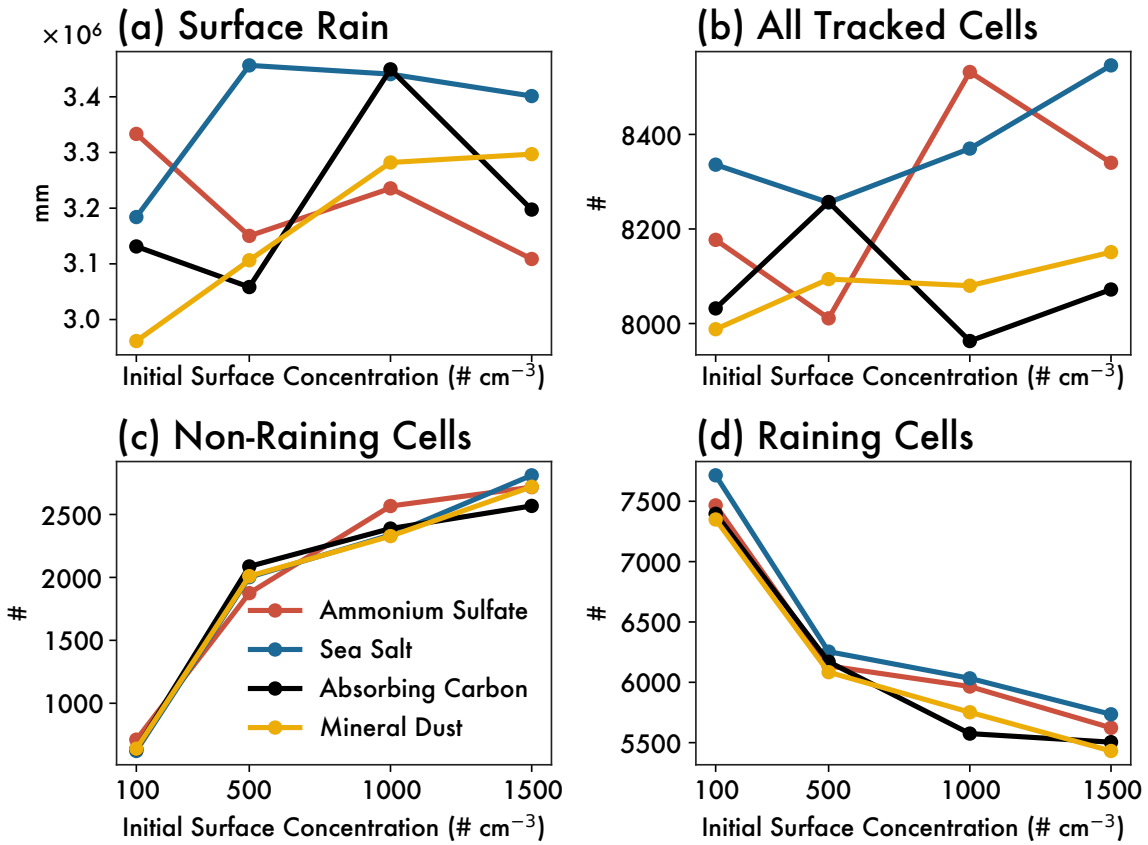

Figure 2.6. (a) Total accumulated rain and (b-d) number of updraft cells tracked over 48 hours of simulation using *tobac* as a function of initial aerosol surface concentration (# cm^{-3}) and aerosol type. Total numbers of tracked cloud cells are shown in (b), while (c) shows only non-raining updrafts and (d) shows only raining updrafts. Raining updrafts are defined as those which have a mean rain rate of at least 0.0001 mm/hr for any time step during their lifetime.

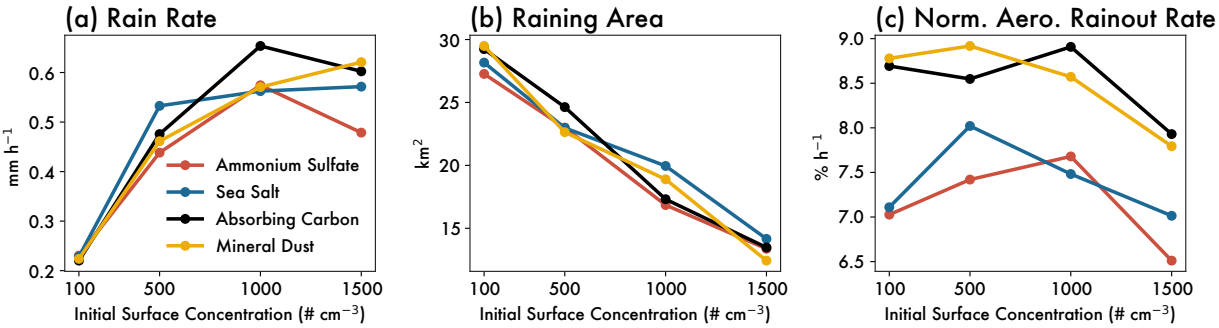

Figure 2.7. Median updraft properties for raining updrafts as a function of initial aerosol surface concentration (# cm^{-3}) and aerosol type. Panels show (a) rain rate (mm hr^{-1}), (b) raining area (km^2), and (c) normalized wet deposition rate (% hr^{-1}). The normalized wet deposition rate is the percent of initial aerosol mass integrated over a given column that is lost to rainout over a given time period.

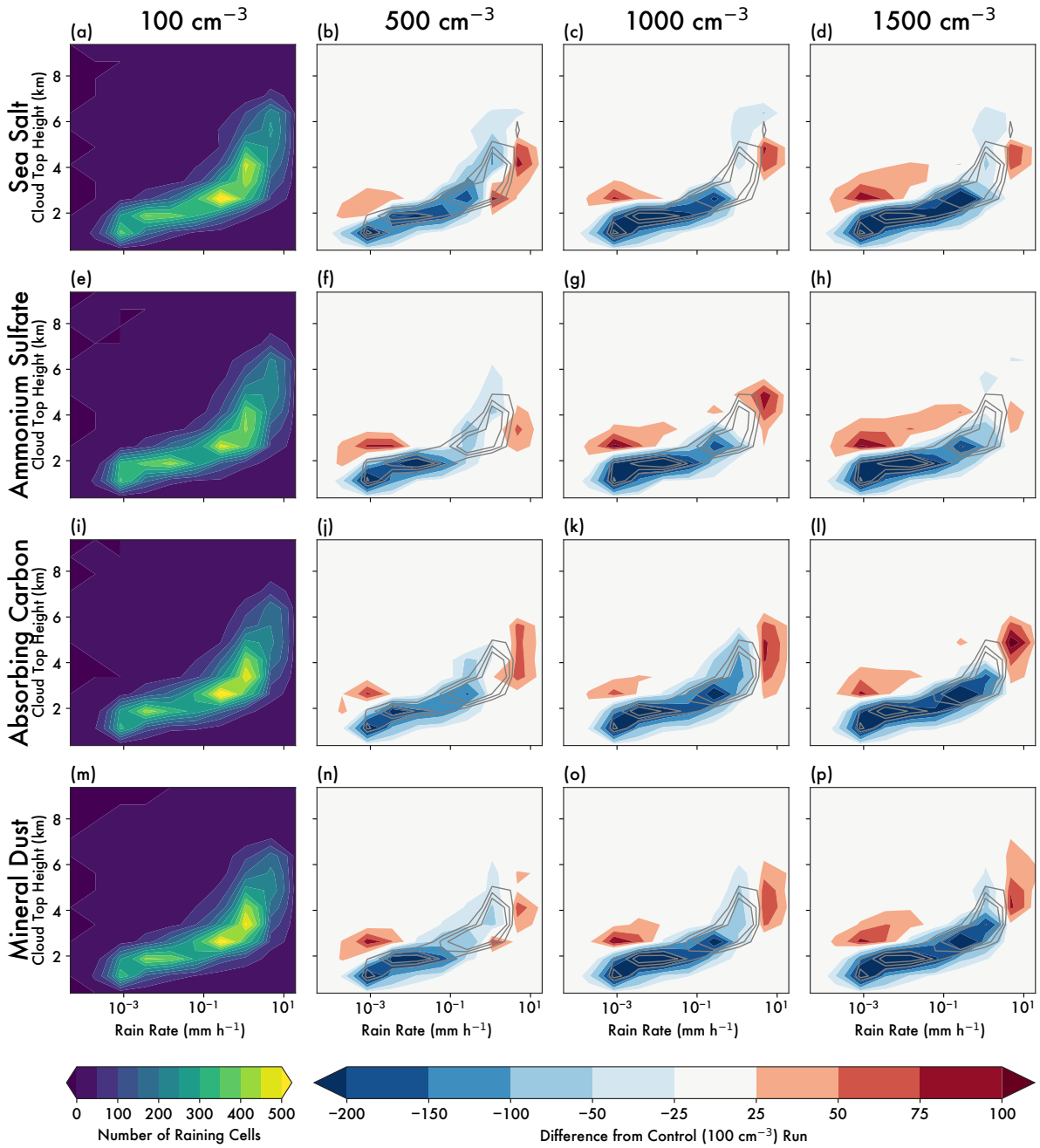

Figure 2.8. Two-dimensional histogram of cloud top height (km) and rain rate (mm hr^{-1}) for all tracked raining clouds. Each row is a different aerosol type: (a-d) sea salt, (e-h) ammonium sulfate, (i-l) absorbing carbon, and (m-p) mineral dust. The leftmost column (a,e,i,m) is the control run with the lowest aerosol loading, and coloured contours indicate the number of raining cloud cells in each joint probability bin. The other three columns are given as a difference in the number of cloud cells relative to the control run of the same aerosol type. The overlaid grey contours correspond to n=250, 300, and 350 in the respective control runs, and are drawn to facilitate comparison between the different simulations.

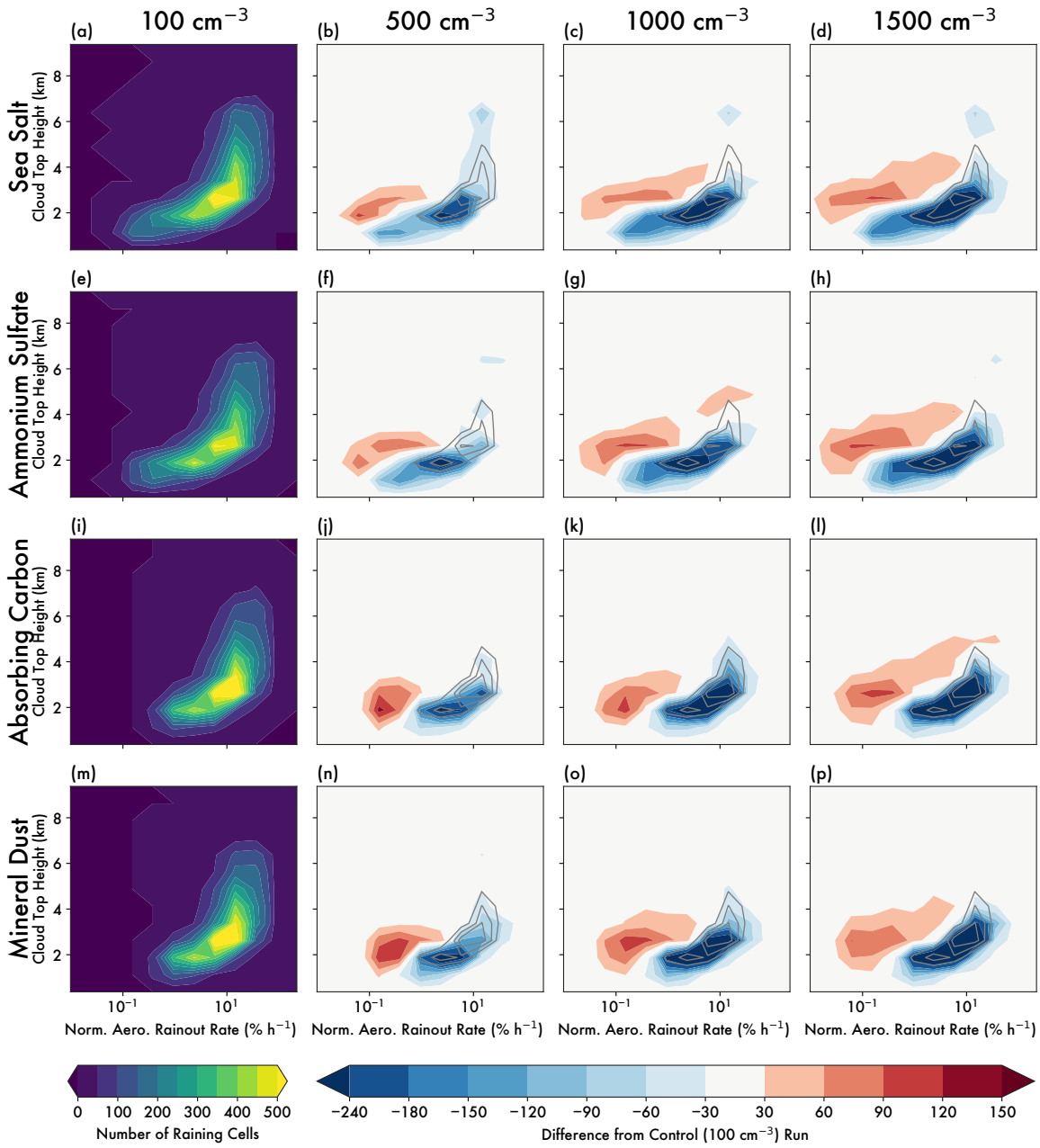

Figure 2.9. As in Figure 2.8 but for normalized aerosol rainout rate. The normalized aerosol rainout rate is the percent of initial aerosol mass integrated over a given column that is lost to rainout over a given time period. The overlaid grey contours in the three rightmost columns are n=300, 400, and 500 in the respective control runs.

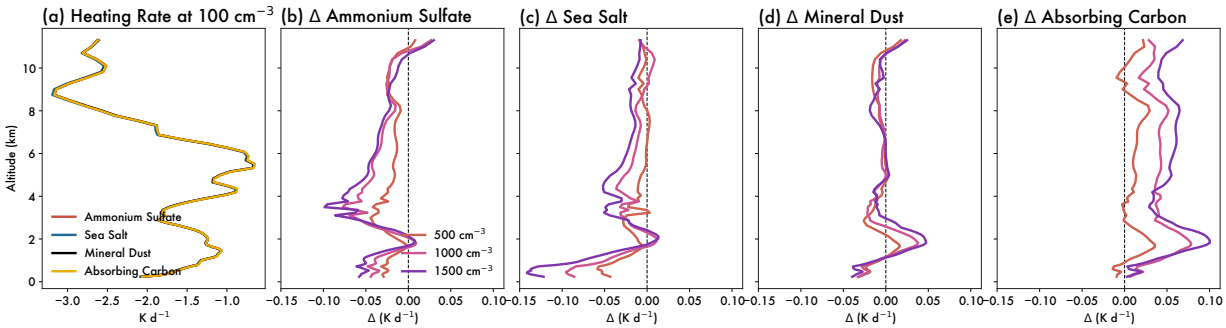

Figure 2.10. (a) Vertical profile of domain-mean clear-sky radiative-heating rates for the lowest-aerosol-loading simulation (initial concentration of 100 # cm^{-3} at the surface). Differences relative to the lowest-aerosol-loading simulation are given for each aerosol type: (b) ammonium sulfate, (c) sea salt, (d) mineral dust, and (e) absorbing carbon. Coloured lines indicate different initial aerosol concentrations.

CHAPTER 3 : DEFORESTATION-DRIVEN INCREASES IN SHALLOW CLOUDS ARE GREATEST IN DRIER, LOW-AEROSOL REGIONS OF SOUTHEAST ASIA[2]

3.1 Introduction

Tropical forests are a key ecosystem component through their roles in carbon storage, the water cycle, and biodiversity (Gibson et al., 2011). However, these forests are at increasing risk of clearing or fragmentation across the globe due to anthropogenic activity (D.-H. Kim et al., 2015b; Song et al., 2018). Among the frontiers of tropical deforestation, Southeast Asia has had the most spatially pervasive and highest proportional rate of deforestation in recent years (Turubanova et al., 2018). Widespread logging and palm oil plantations in the region drove 16% forest cover loss between 2000 and 2020 (calculated as the percent difference in total forest cover fraction between the 2 years, **Figure 3.1**), despite increased government regulation of forest clearing (Margono et al., 2014).

Apart from the many damaging ecosystem and societal effects caused by deforestation, forest loss alters the biogeophysical properties of the land surface (Gentine et al., 2019). These land surface perturbations can propagate via surface fluxes to the atmosphere on local, regional, and even global scales (Gentine et al., 2019; Mahmood et al., 2014). Extensive prior studies show that deforestation leads to increases in near-surface temperatures by reducing evapotranspiration, increasing albedo, and reducing surface roughness (Crompton et al., 2021;

[2] This work, entitled "Deforestation-driven increases in shallow clouds are greatest in drier, low-aerosol regions of Southeast Asia", has been published in *Geophysical Research Letters* (Leung et al., 2024).

Davin & de Noblet-Ducoudré, 2010). The impact of land surface changes on near-surface temperatures can be a similar magnitude to changes in global CO_2 concentrations in regions where land-atmosphere coupling is particularly strong, like in the tropics (Avila et al., 2012; Pitman et al., 2012). Land surface changes also impact the hydrological cycle — evaluating the local impacts of forest loss on clouds and precipitation is therefore crucial for managing water availability, especially given that almost half the global population lives in the tropics (Kummu & Varis, 2011). Furthermore, tropical clouds drive large-scale circulations and impact global weather through teleconnections with other regions, which means changes in local convection due to deforestation in regions like Southeast Asia can have global consequences for weather and climate (van der Molen et al., 2006; Riehl & Malkus, 1958; Schneck & Mosbrugger, 2011).

Although the impact of deforestation on atmospheric temperature is broadly agreed upon, there remains uncertainty around the net impact of deforestation on convective clouds and precipitation (F. Chen & Avissar, 1994a; Laguë et al., 2021). Many fine-scale processes driving land surface-convection feedbacks are not yet well-understood nor explicitly represented in climate models (Spracklen et al., 2018). As a result, the magnitude and even sign of reported deforestation impacts on clouds varies across model types and regions (Lawrence & Vandecar, 2015; A. Takahashi et al., 2017). In Southeast Asia, contrasting modeling studies have shown that deforestation leads to less clouds due to local drying (Tölle et al., 2017) or that deforestation leads to more clouds due to strengthened moisture transport (C.-C. Chen et al., 2019). Observational evidence of these land surface-convection feedbacks has been difficult to obtain due to relative sparsity of data (Lawrence & Vandecar, 2015) and difficulties in attributing measured impacts to land cover changes specifically. For example, rain gauge networks over parts of Southeast Asia have observed decreases in precipitation since the 1950's (Kanae et al.,

2001), but there is debate about whether these changes are driven by deforestation or by other large-scale impacts on the regional climate (Tokinaga et al., 2012).

More recently, large satellite datasets have been used to estimate the cloud response to global forest losses (Teuling et al., 2017; Duveiller et al., 2021; Xu et al., 2022). For example, Xu et al. (2022) found a net increase in regional cloudiness over Southeast Asia associated with forest loss. However, in both these satellite-based studies and global modeling studies (Davin & de Noblet-Ducoudré, 2010; Findell & Eltahir, 2003; Winckler et al., 2017), the cloud response to deforestation varies seasonally and regionally. The exchanges of energy, moisture, and momentum that drive land-atmosphere interactions can be modulated by environmental properties (e.g., moisture availability, wind regimes) (Findell & Eltahir, 2003). The presence of aerosol particles absorbing and/or scattering radiation also alters the amount of radiation reaching the surface, and thus the partitioning of the surface energy budget (H. Jiang & Feingold, 2006; Leung & van den Heever, 2023). This can either dampen or strengthen cloud responses to surface perturbations depending on the aerosol loading (Grant & van den Heever, 2014; Park & van den Heever, 2022). In addition, aerosol particles can also interact with cloud microphysics, leading to synergistic or competing impacts in cloud properties relative to surface perturbations alone (Tao et al., 2012). The uncertainty surrounding the impact of deforestation on clouds is thus compounded by region-to-region variability in thermodynamic and aerosol environments.

In this paper, we use observations to demonstrate the impacts of long-term deforestation on cloud properties over Southeast Asia, and for the first time, examine the variability of these impacts as a function of environmental factors. This provides insight into which regions are at highest risk of deforestation-induced changes in convective clouds. As forest loss continues to accelerate in Southeast Asia and tropical forests around the globe, understanding the subsequent

changes to clouds is essential to a fuller assessment of how future deforestation may impact humans and the broader earth system.

3.2 Data and Methods

We take forest cover observations from the Landsat-derived Global Forest Cover (GFC) dataset (Hansen et al., 2013), which provides annual estimates of forest loss ($\Delta x \sim 30m$). We utilize measurements of cloud fraction, cloud top height ($\Delta x \sim 1km$), precipitable water (PWAT) vapor ($\Delta x \sim 1km$), and aerosol optical depth (AOD, $\Delta x \sim 3km$) from the Moderate Resolution Imaging Spectroradiometer (MODIS) (Platnick et al., 2017). MODIS observations are from the Terra and Aqua satellites with overpass times of ~10:30 a.m./p.m. and ~1:30 a.m./p.m. respectively, though PWAT and AOD are only available during daytime overpasses. To facilitate comparisons between the GFC and MODIS datasets, we resample and reproject the GFC data onto the same grid and resolution as the MODIS data and take annual averages of MODIS data to be at the same temporal resolution as the GFC data.

Changes in the cloud field from one year to another are driven by deforestation or by other sources of interannual variability (e.g., changes in the El Niño Southern Oscillation phase). Our approach leverages the large number of sample points using the "difference-in-differences" method (Crompton et al., 2021) to separate potential drivers of the observed cloud response. For each deforestation event, we take the change in cloud property between the year before and after the forest loss occured. We compare the temporal change in cloud properties over deforested regions to the temporal change over a control intact forest group, which is near enough to experience the same interannual variability but far enough away so as not to experience any direct impacts from the surface deforestation-induced perturbation (**Figure A2.1**). The difference

between the response in deforested and control regions (represented by ε) can thus be interpreted as the response attributable to the forest loss alone. We then bootstrap an estimate of the mean ε over all sample points, aligning the response in time relative to the year in which the forest loss took place (**Figures A2.2, A2.3**). The same response ε can be calculated for subsamples of the full population (**Figure A2.3b,c**), which we group based on quartiles of environmental parameters, namely PWAT and AOD. Additional details can be found in **Appendix 2.**

Cloud response metrics are calculated at an annual timescale, given that forest cover is only available annually. Though this does not allow us to detect deforestation impacts on clouds at finer temporal scales (e.g., seasonal patterns), it does capture the integrated annual impact, which is most relevant to the radiative budget and the overall impact of deforestation on the climate system. We calculate the cloud response separately for each of the four overpass times to provide a picture of the diurnal variability in cloud responses to deforestation.

3.3 Results

3.3.1 Estimated cloud response to deforestation

During the daytime (10:30 a.m. and 1:30 p.m.), increasing forest loss leads to an increase in the annual cloud fraction and a decrease in the mean cloud top height (**Figure 3.2**). In regions facing total forest loss, the annual mean afternoon cloud fraction in the year following the deforestation event increases by up to 5% while the annual mean afternoon cloud top height is 200m lower. Taken together, these changes indicate that the removal of forest cover leads to a local increase in coverage of shallow clouds. These results are generally consistent with findings from recent global satellite-based estimates of cloud responses to deforestation (Duveiller et al., 2021; Xu et al., 2022).

The magnitude of the cloud response to deforestation is largest during the afternoon (1:30 p.m.) and close to negligible at nighttime (10:30 p.m. and 1:30 a.m.) (**Figure 3.2**). This diurnal variation supports the hypothesis that changes in the cloud field following deforestation are driven by differential solar heating between forested and deforested regions. In the afternoon, the cloud response is largest, since surface heating has had sufficient time to drive strong mesoscale circulations and moisture transport. At night, the circulations and associated moisture transport into the deforested region is shut down and local moisture sources are no longer sufficient to support additional cloud development.

The daytime shift to more widespread shallow clouds following deforestation provides observational evidence for previously hypothesized mechanisms involving differential heating-driven mesoscale circulations and increased moisture transport (C.-C. Chen et al., 2019). Following a conversion from forest to bare soil, the reduction in soil moisture and evapotranspiration drives local drying (Werth & Avissar, 2005), which tends to hamper cloud formation. Deforestation may also lead to a reduction in biogenic volatile organic compound emissions, thereby reducing a potential source of cloud condensation nuclei (Duveiller et al., 2021). However, the anomalous local heating due to a combination of albedo, roughness, and moisture effects (Crompton et al., 2021) can induce mesoscale circulations that provide additional lift and transport moisture into the deforested area (Durieux et al., 2003; J. Wang et al., 2009). If the additional moisture source is sufficient, the combination of increased sensible heat fluxes due to a warmer surface and additional moisture due to mesoscale transport can support increased cloud formation. This has been demonstrated using models and observations for more well-studied regions like the Amazon (Khanna et al., 2017; J. Wang et al., 2009), but it has still been recently debated (C.-C. Chen et al., 2019; T.-H. Lee & Lo, 2021) whether the same

applies for Southeast Asia where land covers a much smaller fraction of the surface. This work provides observational evidence that deforestation in Southeast Asia causes more widespread and shallower clouds through effects on mesoscale circulations. Our findings support the more general hypothesis that tropical deforestation leads to increases in shallow clouds (Duveiller et al., 2021), at least for areas where there is an adequate moisture source nearby. Further work is still needed to explore the generality of this result for other tropical forests such as the inland Congo where moisture may be less readily available.

3.3.2 Modulation by precipitable water

To better understand the variability in cloud responses to deforestation, we segment the regional mean response (**Figure 3.2**) into environmental regimes (detailed in **Appendix 2**). **Figure 3.3** explores deforestation-induced changes to cloud properties as modulated by PWAT, the integrated amount of water vapor in the atmospheric column. Areas within the lowest PWAT quartile (~48mm) are generally inland or blocked by terrain, while regions in the highest PWAT quartile (~57mm) are typically coastal (**Figure A2.4a** and **A2.4c** in **Appendix 2**). It should be noted that the low and high PWAT divisions used here are relative terms, since even areas of Southeast Asia with lower PWAT are still in the humid tropics and have more moisture than arid continental areas.

We find the overall sign of cloud responses to deforestation do not depend on PWAT. That is, across all PWAT quartiles, regions with more forest loss tend to have higher cloud fractions and lower cloud top heights, and this effect is strongest in the afternoon. However, we do find that PWAT modulates the *magnitude* of the cloud response: the response to deforestation is stronger in dry regions than in moist regions or in Southeast Asia overall. Deforestation in drier

inland Southeast Asia is thus expected to perturb cloudiness more than it would in the moist coastal areas.

The net deforestation impact on convection depends on a combination of local changes to moisture availability and mesoscale changes in lifting and moisture transport (Mahmood et al., 2014). We can assess the relative importance of these two processes based on the modulation of deforestation impacts by PWAT. The land surface in dry regions heats up faster than in moist regions, since less energy is needed to evaporate liquid water and drive latent heat fluxes. This leads to stronger thermal contrasts between forested and deforested regions, and thus stronger mesoscale circulations and increased mesoscale moisture transport. Although the deforested area sees a decrease in moisture available from local evapotranspiration, this is apparently outweighed by increased moisture from mesoscale transport. Because we see the cloud response to forest loss is strongest in low PWAT areas, our findings support that mesoscale transport is the dominant process by which deforestation impacts convection in Southeast Asia.

3.3.3 Modulation by aerosol optical depth

In addition to the role of moisture in deforestation-cloud impacts, we examine the modulating role of aerosol loading. **Figure 3.4** shows the cloud response to deforestation according to AOD, the integrated amount of light extinction by aerosol particles in the atmospheric column, which here serves as a satellite-observable proxy for aerosol loading. We focus here on AOD only, though we note that other factors more difficult to quantify from satellite data, such as aerosol type and spatial distribution, may also play a role. Areas in the low aerosol category have AODs below ~0.2, while those in the high aerosol category have AODs above ~0.4 (**Figure A2.4b** and **A2.4d** in **Appendix 2**). A higher AOD would result in less solar

radiation reaching the surface, thus reducing the importance of surface perturbations on the overall circulation (Park & van den Heever, 2022).

Unlike with PWAT, we find the response of cloud *fraction* to deforestation is not strongly modulated by AOD. In both the morning and afternoon, low and high AOD categories are not statistically distinguishable from each other or the mean trend. This suggests that—for the range of AODs observed here—we do not expect a significant difference in deforestation impacts on cloud fraction between pristine and polluted environments.

On the other hand, AOD does modulate the sign and magnitude of the cloud top *height* response to forest loss, albeit to a lesser degree than PWAT (**Figure 3.3**). In the regional mean, annual cloud top height decreases with increasing forest loss, indicating a shift to shallower clouds. We find this is still true for the low AOD category. However, negligible or even positive increases in cloud top height are evident when AOD is high. Aerosol loading could therefore offset or mask the impacts of deforestation on cloud top heights. This modulation is consistent with past work showing that the presence of more numerous aerosol particles shifts the shallow cloud distribution towards higher cloud top heights (van den Heever et al., 2011; Leung et al., 2023; Spill et al., 2019). Though changes to cloud microphysics are difficult to ascertain from satellite measurements of AOD alone, these trends suggest that aerosol loading is an important modulator for deforestation-convection interactions.

3.4 Conclusions

In conclusion, these results demonstrate there is a robust and detectable cloud response to deforestation in Southeast Asia on annual timescales and provides the first observational evidence that the magnitude of cloud responses depends on background atmospheric conditions.

Mesoscale circulations between forested and deforested areas are likely the dominant mechanism for providing lift and transporting moisture, particularly in Southeast Asia where deforested areas are in close proximity to the ocean (**Figure 3.5a** and **3.5b**). This study resolves past debates arising from regional modeling studies regarding whether cloudiness increases or decreases following deforestation. The increases in low cloud cover demonstrated here, to first order, exert a net cooling effect on the planet (L'Ecuyer et al., 2019). Through their influence on the radiative budget and the water cycle, these perturbations to tropical clouds can drive downstream climatic and societal impacts.

Moreover, we show for the first time that the magnitude of the observed cloud response to deforestation is strongly modulated by environmental factors like moisture and aerosol loading. Dry regions experience a stronger cloud response than moist regions (**Figure 3.5c**). Meanwhile, high aerosol loadings may mask the impact of deforestation on cloud top heights via offsetting impacts from the land surface changes and aerosol indirect effects (**Figure 3.5d**).

Future work should explore the sensitivity of the cloud response to deforestation to other environmental parameters that vary spatially, such as prevailing wind, atmospheric stability, differences in aerosol composition and vertical distribution, and soil type. Non-linear interactions between multiple parameters (e.g., simultaneously high PWAT and AOD) may further modulate the cloud response to deforestation. The current dataset is insufficiently large to explore such multivariate relationships **(Figure A2.3d),** though we recommend future work investigate such interactions once more data are available. Though this paper examined the cloud response to deforestation on annual timescales, once forest cover data are available at finer temporal resolutions, we also recommend that future analysis focus on understanding the seasonal variability of these impacts. We are currently exploring these complex land-atmosphere

interactions using high-resolution numerical simulations, which also better allow for more certainty in the causal mechanism linking land cover changes and cloud responses.

The results we describe here emphasize that the local signature of forest loss is not uniform, and that some areas are particularly susceptible to deforestation-driven changes in clouds due to climatological factors. Though often overlooked, taking variability in cloud responses to deforestation into account is essential for accurately assessing the impacts of deforestation on weather, hydrology, and future climates, especially as the rate of forest loss continues to accelerate in Southeast Asia and in tropical forests around the world.

3.5 Figures

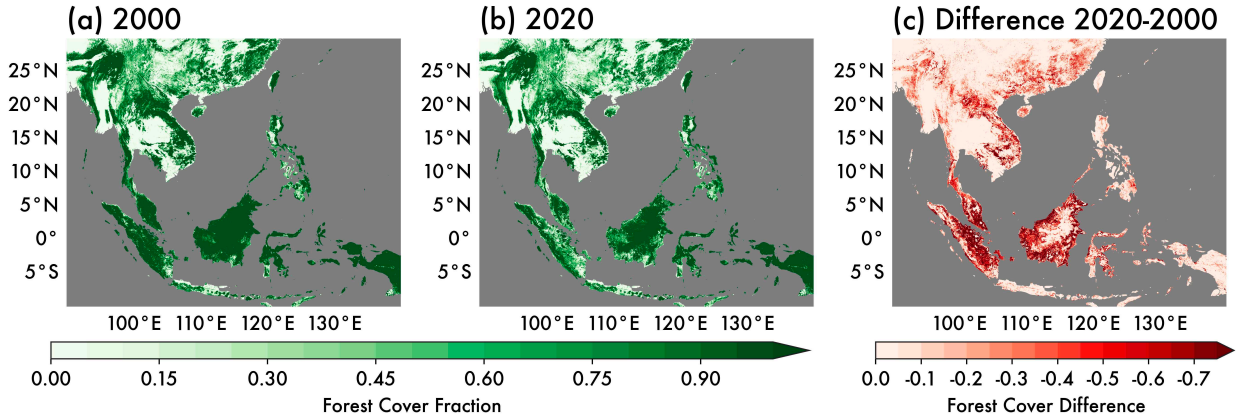

Figure 3.1. The fraction of forest cover in Southeast Asia in (a) 2000 and (b) 2020. (c) The difference in forest cover fraction (i.e., forest loss) between 2000 and 2020. Forest cover data are taken from the Global Forest Cover dataset, as described in Section 3.2.

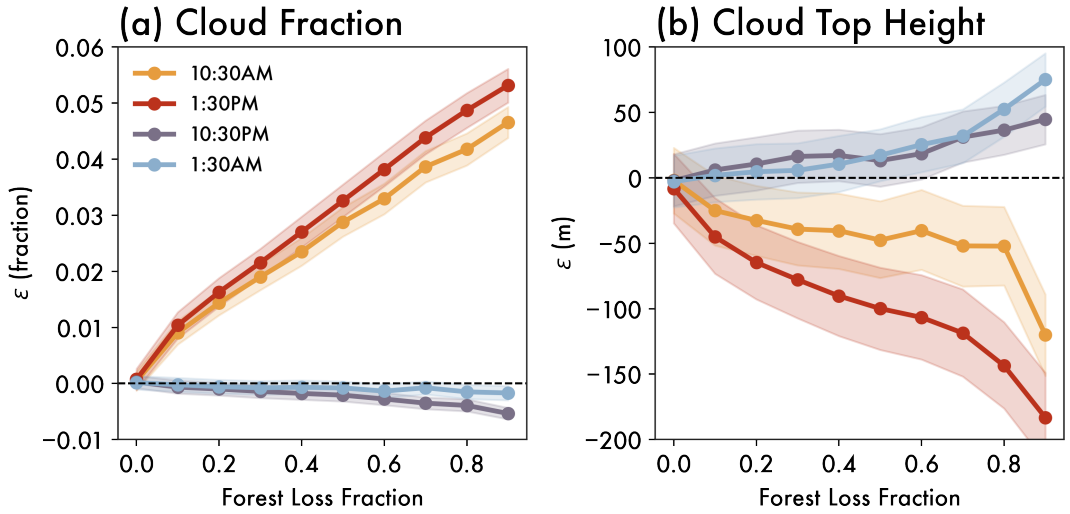

Figure 3.2. Estimated cloud response (ε) to mean forest loss for the annual mean (a) cloud fraction and (b) cloud top height (m). Different colored lines indicate different overpass times. Solid lines indicate the bootstrapped mean (n=1,000), and shaded areas span the 25th to 75th percent confidence interval.

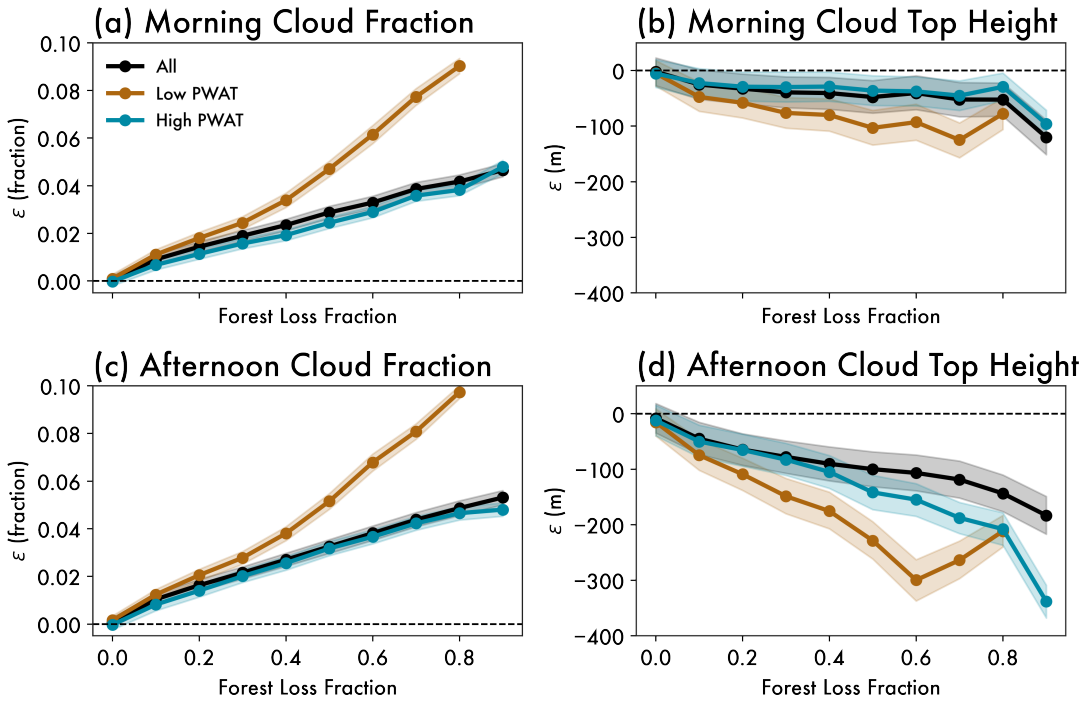

Figure 3.3. Dry regions experience enhanced deforestation impacts on cloud fraction and cloud top height. Data are segmented according to precipitable water quartile. (a,b) Show the Terra daytime overpasses (10:30 a.m.), and (c,d) show the Aqua daytime overpasses (1:30 p.m.). Lines and shading as in Figure 3.2.

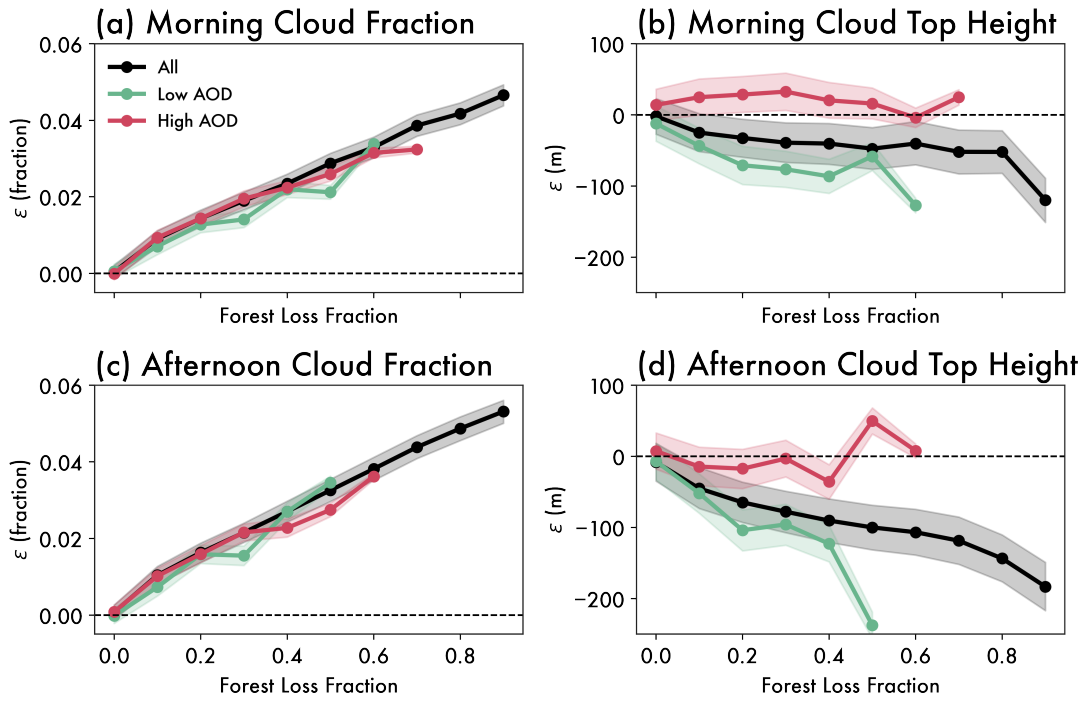

Figure 3.4. High aerosol loadings dampen deforestation impacts on cloud top height, but do not modulate deforestation-induced changes in cloud fraction. As in Figure 3.3, but segmented by aerosol optical depth quartile. Lines and shading as in Figure 3.2.

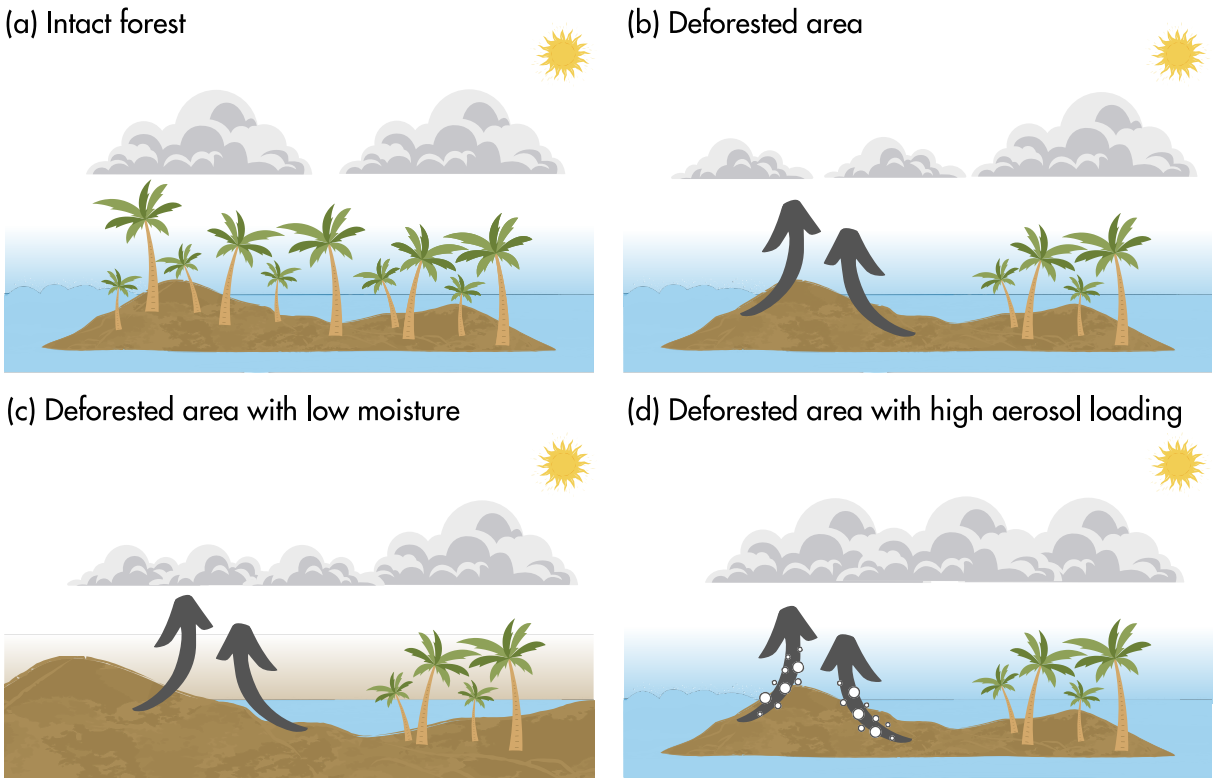

Figure 3.5. Schematic summarizing the impacts of deforestation on cloud properties in Southeast Asia, and modulation by moisture and aerosols. (a) Clouds forming over intact forest during daytime. (b) When an area is deforested, mesoscale circulations form (gray arrows) supporting shallow cloud development (more widespread coverage, but shallower on average in deforested areas compared to forested ones) by transporting moisture from nearby sources, such as oceans. (c) In an inland region with low atmospheric moisture locally available (represented by brown background gradient) but still in proximity to larger moisture sources such as the ocean, the impact of deforestation on clouds is magnified (even more widespread coverage and shallower clouds compared to panel (b)). (d) In a region with high aerosol loadings (white circles), the impact of deforestation on cloud fraction is the same (same coverage as panel (b)), but impacts on cloud top height are dampened (cloud top heights are similar between forested and deforested areas).

CHAPTER 4 : DEFORESTATION IMPACTS ON CLOUDS AND PRECIPITATION OVER BORNEO VARY ACROSS THE DIURNAL CYCLE[3]

4.1 Introduction

Anthropogenic activities drive widespread deforestation in the tropics (Kim et al., 2015; Winkler et al., 2021). Southeast Asia—particularly the island of Borneo—is a hotspot of tropical deforestation, with extensive forest clearing in recent decades driven primarily by oil palm and rubber plantations (S. Chen et al., 2024; Jamaludin et al., 2022; Parker et al., 2024). It is widely accepted that these changes to land surface properties impact the atmosphere through their effects on fluxes of heat, moisture, and momentum between the surface and atmosphere (Mahmood et al., 2014). However, how this translates to impacts on convective clouds and rainfall remains uncertain (Gentine et al., 2019).

The coupling between land surface properties and clouds involves simultaneous changes to the surface energy budget, and boundary layer moisture and temperature responses. At times, thermodynamic changes act in opposition: switching from a vegetated surface to bare ground leads to low-level warming and drying, which have opposite impacts on convection (C.-C. Chen et al., 2019). The net impact of these contrasting feedbacks appears to depend on background meteorology (Findell & Eltahir, 2003) and cloud type (Baidya Roy & Avissar, 2002; Cioni & Hohenegger, 2017), both of which vary across the course of the day. Changes in clouds caused by land cover changes in turn drive shifts in the energy budget. Moreover, the surface energy

[3] This work, entitled "Deforestation impacts on clouds and precipitation over Borneo vary across the diurnal cycle", is in preparation for submission to the *Journal of Geophysical Research: Atmospheres* (Leung and van den Heever, in prep).

budget itself changes over the day as the balance between radiation, turbulent fluxes, and surface heating is repartitioned in response to diurnal changes in insolation. These interactions between the surface and convection further complicate the cloud response to deforestation, particularly since this land-atmosphere coupling evolves on diurnal timescales.

Recent satellite-based estimates suggest deforestation in Southeast Asia locally enhances cloud cover (Xu et al., 2022; Leung et al., 2024), though the magnitude of the cloud response appears to depend on background meteorology and time of day. Although such observational quantifications are essential, it is challenging to extract information about the mechanisms driving cloud responses from these long-term estimates. This observational work must thus be complemented with process-oriented modeling studies.

Most modeling-based investigations of deforestation impacts over Southeast Asia have used global or regional climate models, which allow for long integration times to assess the climatic implications of these widespread changes in land cover (Werth & Avissar, 2005; Schneck & Mosbrugger, 2011; A. Takahashi et al., 2017; Tölle et al., 2017; C.-C. Chen et al., 2019; H.-C. Chen & Lo, 2023). However, disagreements remain about the sign of deforestation impacts on cloud cover. This is perhaps to be expected, given that processes driving convection (especially shallow clouds) are not explicitly resolved in large-scale models and are thus sensitive to how models parameterize convective responses to these compensating deforestation impacts on moisture and temperature (C.-C. Chen et al., 2019). This uncertainty highlights the need to improve our understanding of land surface-convection interactions at scales where convective processes can be more accurately resolved, especially in regions like Southeast Asia where much convection is driven by diurnally reversing mesoscale flows (e.g., sea breezes, terrain flows) that are sensitive to surface properties (Qian, 2008; Yang & Slingo, 2001).

Despite these challenges in quantifying cloud responses to forest loss, doing so is essential to fully characterizing deforestation impacts on weather, hydrology, and the Earth's energy balance (Boysen et al., 2020; Laguë et al., 2021). Such impacts may also vary between different types of convection (Gentine et al., 2019). Thus, we must understand how different cloud types and associated precipitation rates respond to changes in the land surface.

This research aims to quantify the impacts of deforestation on a range of tropical convection morphologies, as well as elucidate the physical mechanisms driving these impacts. Specifically, we address the following two science questions: (1) how does deforestation impact different cloud types across the diurnal cycle? and (2) what is the impact of those cloud responses on surface precipitation? We address these questions using cloud object-tracking techniques applied to a pair of high-resolution simulations with forested and deforested land cover, described in **Sect. 4.2**. We quantify how these land surface changes impact the surface energy budget and near-surface atmosphere in **Sect. 4.3**. In **Sect. 4.4**, we quantify impacts of the initiation of tracked cloud objects across the diurnal cycle. We discuss how these deforestation-driven shifts in the cloud distribution impact precipitation in **Sect. 4.5**. Finally, we summarize our findings and discuss broader implications of this work in **Sect. 4.6**.

4.2 Methods

4.2.1 Model description and configuration

We conducted large eddy simulations (LES) using the Regional Atmospheric Modeling System (RAMS version 6.3.04) (Pielke et al., 1992; Cotton et al., 2003; Saleeby & van den Heever, 2013). Full information about the model settings is provided in **Table 4.1**, but we describe key aspects of the model set-up below.

Our simulations reproduce the diurnal cycle of convection (**Figure 4.1**), including the daytime transition from shallow to deep convection during synoptically benign conditions when convection is primarily driven by local thermodynamics rather than large-scale forcing. The simulation domain encompasses a large area (~322x334km) in northwestern Borneo, around the city of Kuching, Malaysia (red shading; **Figure 4.2**). We selected this region due to the extensive land cover changes over the past few decades (discussed in **Section 4.2.2**). The morphology, timing, and distribution of clouds in our simulations are similar to observed cloud patterns (**Figure 4.1**). We note, however, that we analyze these simulations in a statistical manner to examine land-convection interactions in the region, rather than as a case study intended to recreate specific meteorology from a specific day.

To adequately resolve fine-scale atmospheric features driving the initiation and development of shallow cumuli, we used a fine spatiotemporal resolution ($\Delta x = \Delta y = 150$m, $\Delta z = 50$-300m, $\Delta t = 1.5$s). This, in combination with our large model domain integrated over three diurnal cycles (72 hours, 17-20 September 2019) allowed us to extensively sample the trimodal distribution of tropical convection (Johnson et al., 1999). Our simulation period was directly before the transition from the southwest to northeast monsoon (Reid et al., 2023). We initialized and nudged the lateral boundary conditions using ERA-5 reanalysis (Hersbach et al., 2020), which constrained the synoptic scale environment while ensuring that convective and mesoscale features within the domain could evolve freely.

Two-way land-atmosphere exchanges were parameterized using the Land Ecosystem Atmosphere Feedback (LEAF-3) (Walko et al., 2000) surface model. LEAF-3 represents turbulent and radiative exchange between the soil/ground, vegetation, and a canopy layer, which then exchanges energy, water, and momentum with the lowest atmospheric layer.

4.2.2 Experiment set-up

We conducted two simulations, which were constrained with the same atmospheric initial and boundary conditions but differed in land cover. Using the same large-scale atmospheric forcing allows us to compare how land-atmosphere interactions impact local convective development.

Land cover was taken from the Historic Land Dynamics Assessment+ (HILDA+) dataset (Winkler et al., 2021), which combines remote sensing and long-term statistical datasets to estimate land cover ($\Delta x,y=1km$) from 1960-2019. We matched HILDA+ land cover types with relevant LEAF-3 classes based on spatial coincidence with default RAMS land cover and present-day MODIS land cover (Friedl et al., 2002). Land surface properties key to this study are shown in **Figure 4.2**.

We ran one simulation with land cover from 1960 (VEG1960) and one with land cover from 2019 (VEG2019) (**Figure 4.2**). By using a realistic distribution of land cover rather than total deforestation or an idealized checkerboard-type pattern, we can examine the effects of realistic scales of deforestation and patterns of landscape heterogeneity.

The primary land cover change between 1960 and 2019 is a widespread shift from "evergreen broadleaf forest" representing intact tropical rainforests to "wooded grassland" and "cropland" representing plantations of oil palm, rubber, and other agricultural uses. Increases in "urban surface" are also evident. We refer to these three predominant non-forest land cover types as "deforested". Compared to intact rainforests, deforested land has a lower surface roughness / shorter canopy height and larger albedos. Deforested areas also have lower evaporative resistance, since forest vegetation retains more water for a given temperature increase.

Unlike other modeling studies examining deforestation in Southeast Asia that replace forest with C4-type grass (Tölle et al., 2017; C.-C. Chen et al., 2019), forest is primarily replaced by "wooded grassland" in our simulations. This surface type best matches observations of oil palm and rubber plantations in terms of land surface properties such as vegetation height (June et al., 2018) and evaporative resistance (Giambelluca et al., 2016). In contrast to regions like the Amazon where deforestation is primarily driven by conversion to cropland or pastureland, transitions from tropical forest to palm oil and rubber plantations are unique in that they do not necessarily reduce evapotranspiration (Spracklen et al., 2018).

4.2.3 Cloud object identification and tracking

We tracked individual convective clouds across their entire lifecycles using the Tracking and Object Based Analysis of Clouds (*tobac* version 1.5) algorithm (Heikenfeld et al., 2019; Sokolowsky and Freeman et al., 2024). Below is a brief description of how we have used *tobac.* We direct readers to the cited papers for a full algorithm description.

First, we identified updrafts as contiguous three-dimensional regions with local vertical velocity maxima >1 m s^{-1} (with additional thresholds every 2 m s^{-1} between 2 and 50 m s^{-1} to separate updrafts of varying intensities) over a volume >64 grid points. Second, we connected updrafts across timesteps by linking their projected trajectories in time. Any updrafts with lifetimes <15 minutes were excluded from our analysis to ensure we only analyze clouds that are well-captured across their life cycle. Third, we used watershedding to identify contiguous regions around each updraft that have vertical velocities >1 m s^{-1} and cloud condensate mixing ratios >0.01 g kg^{-1}. Regions which have updrafts collocated with condensate are considered "clouds", which allows us to separately analyze cloudy updrafts and dry boundary layer

thermals. Finally, we calculated key properties for each cloud object, including cloud lifetime, cloud base height (CBH), cloud top height (CTH), cloud footprint area, CTH growth rate, and mean precipitation rates.

The large dataset of identified clouds (>75,000 per simulation) allows for robust statistical assessment of a range of cloud modes, each of which may be coupled to the land surface via different processes. We exclude high clouds originating offshore or outside of our domain from our analysis. High cirrus is ubiquitous in the region, but not directly impacted by the surface perturbations we test here. We require all clouds to have initiated from within the boundary layer (with their initial centroid at the time of first detection <2km).

The specific thresholds utilized here are ultimately subjective, but testing these parameters shows qualitatively similar results. *tobac*-tracked cells account for >80% of the total surface precipitation in the domain, which adds confidence that our methods capture most convective clouds of interest to our science questions. Examples of cloud masks and tracks generated using *tobac* are shown in **Figure 4.2c,f**.

4.3 Deforestation impacts on the surface energy budget

We begin by examining the diurnal surface energy budget, averaged over land points for all three simulation days (**Figure 4.3**). We use a sign convention of negative values indicating terms which cool the surface (energy transferred from surface to atmosphere or ground). The magnitude of radiative and turbulent heat fluxes in our simulations compare favorably with flux measurements over rainforests and oil palm plantations in Borneo (Fowler et al., 2011; Takanashi et al., 2010; Tang et al., 2019). The magnitude of latent heat fluxes (LHF) is larger than that of sensible heat fluxes (SHF), due to abundant moisture. Prior to the onset of clouds,

the mean Bowen ratio (B=SHF/LHF) ranges from 0.3-0.5 between 7-9a.m. (here and throughout the text, times are given in local time UTC+8).

Deforestation from VEG1960 to VEG2019 (solid versus dashed lines; **Figure 4.3a**) drives robust shifts in the surface energy budget (**Figure 4.3b**). Positive changes in **Figure 4.3b** indicate deforestation leads to more energy transfer *into* the surface (or less transfer *out* of the surface). Similar trends are evident across all simulation days.

Changes to the surface energy budget between the two simulations are dominated by SHF impacts (red lines; **Figure 4.3**). Deforestation reduces energy transfer from the surface to the atmosphere via SHF (decrease in SHF magnitude). This is driven by the reduced surface roughness associated with changes from tall rainforest to shorter palm oil plantations. The smoother deforested surface is less efficient at transmitting energy into the atmosphere through turbulent fluxes.

As a result of the less efficient turbulent exchange, more energy accumulates at the surface and goes into heating the vegetation canopy and the ground (gray lines; **Figure 4.3**). We confirm this by examining vegetation canopy and near-surface (~25m a.g.l.) air in **Figure 4.4**. Indeed, the increased heat storage results in warmer land surface temperatures and warmer air at canopy level throughout the day (**Figure 4.4c**), consistent with satellite-based observations (Sabajo et al., 2017; Crompton et al., 2021) and field measurements (Hardwick et al., 2015). However, this energy is not efficiently transmitted from the smooth surface into the atmosphere, resulting in a more modulated near-surface temperature diurnal cycle in VEG2019 compared VEG1960 (**Figure 4.3b**). Rather than transferring energy through turbulent fluxes, the smooth deforested surface radiates more energy as outgoing longwave radiation (OLR) (green lines; **Figure 4.3c**).

The warmer canopy air in VEG2019 enhances evapotranspiration (ET), with most of the energy stored in the canopy going into latent heating. Deforested areas have lower evaporative resistance, meaning for a given temperature, they release more moisture into the atmosphere than forested regions. Deforestation thus moistens canopy air (**Figure 4.4c**). LHF, like SHF, depends on the efficiency of turbulent surface-atmosphere exchange and is hampered by the smoother deforested surface. However, since there is a larger moisture source due to enhanced ET, LHF is enhanced in the deforested scenario after 9a.m. (blue lines; **Figure 4.3**) once the canopy heats up sufficiently for ET to counteract reduced turbulence. This response reflects deforestation in moist, tropical environments where forests are primarily converted to oil palms or other agricultural lands that retain high soil moisture (van der Molen et al., 2006)—if deforestation instead converted the forested area to bare soil (or moisture-limited vegetation) LHF would likely differ (C.-C. Chen et al., 2019; Drager et al., 2020; H.-C. Chen & Lo, 2023).

Changes in the surface energy budget following deforestation are dominated by non-radiative properties (surface roughness and evaporative resistance) rather than radiative properties (albedo) (**Figure 4.3**). This is consistent with past work showing changes in tropical surfaces do not have as large an impact as in middle and high latitudes (Davin & de Noblet-Ducoudré, 2010; Duveiller et al., 2021). We observe only ~2% increases in the net shortwave (SW) flux following deforestation due to the more reflective surface. Once clouds develop after 9a.m., there is a bigger deforestation impact on SW (yellow line; **Figure 4.3**). However, changes due to reduced cloud cover (more downwelling SW) and increased albedo (more upwelling SW) act in opposite directions, such that the SW contribution to surface energy budget changes is secondary compared to changes in SHF.

4.4 Cloud responses to deforestation

4.4.1 Overview of cloud evolution

Our simulations capture the trimodal tropical convection distribution (Johnson et al., 1999) and shallow to deep convection transition in the Maritime Continent (Renggono et al., 2001; Argüeso et al., 2020; Marzuki et al., 2022). **Figure 4.5** shows the mean distribution of cloud number and area binned by CTH across the diurnal cycle. We also show the mean cloud development (white arrows; **Figure 4.5a,b**), calculated as the mean change in CTH over five minutes for all cells within a given bin. The surface heats up after sunrise (6:15a.m.) until shallow cumulus fields develop around 9a.m. These shallow cumuli (1km<CTH<3km) are mostly non-precipitating and organize in cloud streets. By 12p.m., the sea breeze has propagated onshore, and congestus (4km<CTH<10km) have formed along the convergence zone ahead of the sea breeze. These convective cells precipitate more strongly and produce cold pools that collide, creating more areas of low-level convergence. Some collisions result in deeper cumulonimbus (CTH>10km, a small number of clouds but a large cloud area) between 4p.m. and sunset (6:30p.m.), while other less favorably located congestus only reach maximum CTHs of ~8km before dissipating. This division between congestus which eventually become deep convection (transient congestus) and those which do not (terminal congestus) (Luo et al., 2009; Leung & van den Heever, 2022) is evident as the bifurcation in the mean cloud development (white arrows; Figure 5a,b).

4.4.2 Mean shallow cloud responses

Deforestation-driven changes in surface-atmosphere interactions manifest as shifts in the cloud distribution (**Figure 4.5c,d**). In terms of cloud number, deforestation dampens the diurnal

cycle over land. Due to weaker SHFs (**Figure 4.3**), there are fewer dry boundary layer thermals and the planetary boundary layer (PBL) deepens more slowly in VEG2019 than in VEG1960. The lifted condensation level (LCL) is lower following deforestation (**Figure 4.6a,c**), meaning parcels lifted from the surface should form clouds at lower altitudes. However, the weakened SHFs limit the ability of thermals to penetrate the LCL and form clouds. Deforestation thus shifts the peak in the cloud diurnal cycle later in the day, once the PBL is sufficiently developed.

The cloud response to lower SHFs following deforestation is counteracted by increased LHFs and enhanced evapotranspiration (**Figure 4.3**). Although the near-surface atmosphere is indeed moister in the deforested scenario (**Figure 4.6b,d**), this enhanced moisture does not extend vertically given the limited turbulent mixing over smoother deforested surfaces. As a result, the lower LCL in VEG2019 coincides with an increased distance between the LCL and the level of free convection (LFC), meaning more convective inhibition (**Figure 4.6a,c**). Even if parcels reach the LCL more easily in VEG2019, they are not positively buoyant and therefore less likely to become active shallow cumuli (Stull, 1988; Gentine et al., 2013).

4.4.3 The role of mesoscale circulations

Mesoscale circulations are found to locally impact cloud frequency in **Figure 4.7**, which shows the deforestation-driven change in amplitude of the cloud number diurnal cycle. We calculate the mean cloud diurnal cycle based on the number of clouds occurring in each 6x6km box at each time of day, averaged over the three simulated days. For each point, we then find the diurnal maximum number of clouds and compare this peak for VEG2019 and VEG1960. In this manner, **Figure 4.7** accounts for temporal offsets in the diurnal cycle (e.g., if the peak of cloud development happens slightly later / earlier in the day). **Figure 4.7a** is smoothed using a rolling

12x12km triangle-weighted window for clarity. For most regions, there is a decrease in peak cloud number, consistent with our earlier findings that deforestation suppresses shallow cumuli (**Figure 4.5c**). However, there are some areas where cloudiness is enhanced following deforestation (red points; **Figure 4.7a**). In these regions, cloud number and cloud area are greater at midday following deforestation (**Figure 4.7c,d**).

The spatial pattern of deforestation-induced cloud changes comprises dipole structures of cloudiness aligned along regions of forest loss from VEG1960 to VEG2019. Regions where cloudiness is enhanced tend to be located on the side of the deforestation boundary with less forest loss, suggesting the influence of mesoscale solenoidal circulations. **Figure 4.8** shows regions of enhanced cloudiness coincide with areas where turbulent heat fluxes and near-surface virtual potential temperature are enhanced relative to area means. Local enhancements in cloudiness along the interface between pristine and perturbed land cover regions are driven by the ascending branch of these circulations on the warmer, drier side of the gradient. These mesoscale circulations—referred to as vegetation breezes (Saad et al., 2010; Khanna et al., 2017; J. Chen et al., 2023)—transport low-level moist air from more deforested regions (where LHFs are higher) to less deforested regions where air is positively buoyant and the circulations provide the lift for cloud formation. This results in local increases in forced cumuli around the deforestation boundary (Ascher et al., 2025; Falk et al., 2025).

4.4.4 Impacts to sea breeze and deep convection

Across the domain, there is a reduction in deep convection following deforestation (**Figure 4.5b,d**). In part, this follows from reduced shallow cumuli earlier in the day (**Section 4.4.1**). Even once the decrease in midday shallow cumuli is accounted for, we still observe a further

decrease in the proportion of clouds that develop into deep convection after deforestation. Taking the relative proportion of cloud area between 4p.m. and 8p.m. (the peak of deep convective activity), 10% more cloudy area in VEG2019 is associated with terminal congestus when compared to VEG1960. These differences are due to changes in the large-scale moisture convergence associated with changes in the sea breeze.

The SSTs in the simulations are nearly identical. Alongside this, there is a near-surface cooling over land in VEG2019, which leads to a weakening of the sea breeze compared to VEG1960. **Figure 4.9** shows the diurnal average of low-level moisture flux convergence (MFC; vertically integrated from the surface to 1km) as a function of distance from the coastline. The sea breeze does not penetrate as far inland (~2km closer to the coastline) and generally fluxes less moisture inland (maximum MFC is ~1 kg m^{-2} hr^{-1} lower) following deforestation. This is consistent with past work on surface roughness and evapotranspiration impacts on sea breeze strength and propagation (Gero & Pitman, 2006; Grant & van den Heever, 2014).

As a result of the reduced onshore moisture flux following deforestation, fewer deep convective cells initiate in the late afternoon (**Figure 4.5d**) along the sea breeze front (black contours; **Figure 4.9a,b**) in VEG2019 compared to VEG1960. The development of the few deep convective clouds in the VEG2019 simulation is shifted to later in the evening (**Figure 4.7c**).

4.5 Implications for precipitation

The changes to convection across the diurnal cycle caused by widespread deforestation have substantial implications for precipitation at the surface. **Figure 4.10** shows changes in the diurnal cycle of clouds across the domain, as in **Figure 4.7**, but only for clouds with appreciable rain at the surface (rain rate > 0.01mm hr^{-1}). The area with positive changes (i.e., more raining

clouds) is more evenly distributed across **Figure 4.10a** compared to **Figure 4.7a**. Although mesoscale circulations support increased convection along the deforestation boundary, the change in *raining* cumuli is more spatially uniform. This suggests the increase in shallow cumulus rainfall is driven by domain-wide changes in low-level moisture rather than lifting driven by surface heterogeneities, though these may still play a secondary role. Fewer active shallow cumuli form, but those which do have access to more near-surface moisture and trigger the onset of precipitation earlier in the day (**Figure 4.10b,c** and **Figure 4.11a,c**). Although these precipitating shallow cumuli comprise a small number and a limited integrated contribution to the overall water budget, these deforestation-driven changes happen during a time of day when very little precipitation occurs in general. Thus, any shifts have a large relative contribution to when and where rainfall occurs (10% increase in raining area and 5% increase in rain from shallow cumuli between 10a.m.–1p.m.).

In contrast to the aforementioned changes in rainfall from shallow cumulus, we find that deforestation suppresses deep convection associated with sea breeze convergence, thereby leading to a decrease in the magnitude of the diurnal rainfall peak (**Figure 4.11d**). A majority of rainfall in our simulations is driven by deep convection that forms after 3 p.m. (**Figure 4.11b**), and thus the net deforestation impact is a decrease in overall precipitation.

4.6 Conclusions

The acceleration of deforestation in many regions of the world, including tropical Southeast Asia, motivates an urgent need to understand what impact these land cover changes have on clouds and precipitation. Disagreement among global and regional climate models on the sign of deforestation-induced cloud feedbacks demonstrates a gap in our understanding of the

convective and mesoscale processes involved. In this study, we use a set of high-resolution large eddy simulations with varied land cover but identical atmospheric initial and boundary conditions to elucidate the mechanisms by which deforestation impacts clouds over Borneo. We focus on how land surface-convection interactions are influenced by changes to mean thermodynamics and mesoscale features like vegetation breezes and sea breezes. **Figure 4.12** illustrates the major processes governing these interactions.

Overall, we find that deforestation induces robust changes to the surface energy budget and thermodynamic responses in the near-surface atmosphere. The shift from rainforest to palm and rubber plantations reduces surface roughness and makes turbulent land-atmosphere exchanges less efficient. This leads to a decrease in sensible heat fluxes that is primarily compensated for by a warming of the ground and vegetation canopy. Unlike in other regions where the conversion of forest to pasture or bare soil decreases latent heat fluxes, we find that under these moisture-rich conditions deforestation enhances evapotranspiration due to warmer canopies and weaker evaporative resistance. This unique surface response is consistent with observations (Fowler et al., 2011; Giambelluca et al., 2016; Spracklen et al., 2018), but has typically been neglected in regional climate modeling studies for this region (A. Takahashi et al., 2017; Tölle et al., 2017; C.-C. Chen et al., 2019). These changes to the surface energy budget lead to a cooler and moister near-surface atmosphere, and increases in convective inhibition following widespread deforestation, thereby changing the thermodynamic environment convection develops in.

Despite these clear energetic shifts, we find deforestation impacts on clouds are not homogeneous: changes to convection vary spatially and diurnally. Deforestation drives a decrease in late morning shallow cloudiness across the region via reduced sensible heat fluxes and enhanced convective inhibition. Yet, we find shallow cloudiness is locally enhanced by

mesoscale vegetation breezes in areas with substantial forest loss. Local and regional deforestation impacts can therefore be in opposition. Quantifying the net deforestation impact on shallow clouds—which may have strong radiative implications for climate (Gentine et al., 2019)—may depend on how extensive these vegetation-driven mesoscale circulations are, and thus on the spatial pattern of deforestation and the degree of land surface heterogeneity. Furthermore, we find that in spite of this region-wide suppression of shallow cumuli, the increased low-level moisture drives more of the shallow cumuli that do form to start raining earlier in the day. This leads to shifts in the diurnal timing and coverage of precipitation, which motivates the need for further observational validation that disaggregates deforestation impacts on clouds and rainfall at different times of day (Leung et al., 2024; Ruijsch et al., 2025)

Deep convection is strongly impacted by deforestation-induced changes in large-scale moisture flux convergence. Deforestation dampens the land-ocean contrast in low-level temperatures, thereby weakening the sea breeze. This reduces moisture advection and limits development from shallow to deep convection, resulting in proportionally more clouds remaining as terminal congestus (4km<CTH<10km) instead of developing into deep convection (CTH>10km). The deep convection that does develop under the deforested scenario tends to be shifted beyond sunset, with corresponding shifts in the diurnal precipitation maxima. Changes to diurnal timing may impact the net radiative effects of deep convective clouds and their anvils, since the shortwave cooling effects associated with deep convective anvils becomes more muted as their timing is shifted past sunset, but their longwave warming effects remain similar (Jones et al., 2024).

Compared to more-studied deforestation hotspots like the Amazon, the region of Southeast Asia we focus on is unique both in terms of the prevailing land use (with the transition to oil

palm and rubber plantations meaning evapotranspiration remains relatively high) and background meteorology (highly moist, with strong mesoscale influences on convection). We speculate the processes we discuss here are broadly applicable to other tropical deforestation regions with nearby moisture sources (e.g., Central America, coastal West Africa) (D.-H. Kim et al., 2015a; Taylor et al., 2022). That said, the *net* deforestation response is highly dependent on relative contributions from the local and regional processes we discuss in this paper, and thus may varies across regions and even seasons. For example, mesoscale breezes might become relatively more important compared to regional changes during the dry season (Leung et al., 2024). Deforestation impacts may further be modulated by other properties like aerosol emissions from forest clearing-related biomass burning (as visible in smoke in **Figure 4.1a,d**, but not included in our simulations). Such aerosol–land surface–cloud feedbacks have been shown to impact mesoscale circulations like the sea breeze (e.g., Grant and van den Heever 2014; Park and van den Heever 2022) and are the subject of a future set of planned investigations.

In conclusion, we demonstrate in this work that shallow and deep convection are coupled to the land surface through processes acting on different spatiotemporal scales. Shallow convection is more sensitive to regional changes in thermodynamics and local changes in mesoscale vegetation breezes, while deep convection is more sensitive to changes in moisture convergence associated with the sea breeze. There is therefore both a strong diurnal structure and mesoscale heterogeneity in the signal of deforestation-driven changes in clouds and precipitation. Though typically unresolved in large-scale models, our findings emphasize that these convective and mesoscale processes must be carefully incorporated into assessments of the impacts of land cover changes on clouds, hydrology, and climate.

4.7 Tables

Table 4.1. RAMS model parameters relevant to this study

Model aspect	Description
Grid	Arakawa-C grid
	2150 x 2230 points, $\Delta x = \Delta y = 150$m
	106 vertical levels, Δz=50-300m with a stretch ratio of 1.04
Timestep	Δt = 1.5s
	Output every 5 minutes
Integration time	6 hours spin-up time (excluded from analysis) + 72 hours (3 diurnal cycles)
Initialization	Initialized from ERA-5 (Hersbach et al., 2020)
Boundary conditions	Nudged with hourly ERA-5 data at lateral (25 grid points from side) and top (above 22km) boundaries with nudging timescale = 900s (15 mins)
Surface scheme	Land Ecosystem-Atmosphere Feedback (LEAF-3) (Walko et al., 2000)
	Land cover taken from HILDA+ (Winkler et al., 2021) matched to LEAF-3 land cover classes
	Soil classes taken from UN FAO dataset (FAO United Nations, 1974)
	11 soil layers extending to 0.5m below the surface, with soil moisture and temperature initialized from ERA-5
Turbulence scheme	Smagorinsky (1963) with modifications from Lilly (1962) and Hill (1974)
Microphysics scheme	RAMS two-moment bin-emulating microphysics (Meyers et al., 1997; Saleeby & Cotton, 2008)
Radiation scheme	RTE-RRTMGP (Pincus et al., 2019)
	Radiation tendencies updated every 5 minutes
Aerosol treatment	Aerosol number concentration = 600 cm^{-3} at surface, exponentially decreasing with height with scale height of 7km
	Fixed aerosol concentrations (no sources, sinks, or advection)
	Aerosol-radiation interactions are represented

4.8 Figures

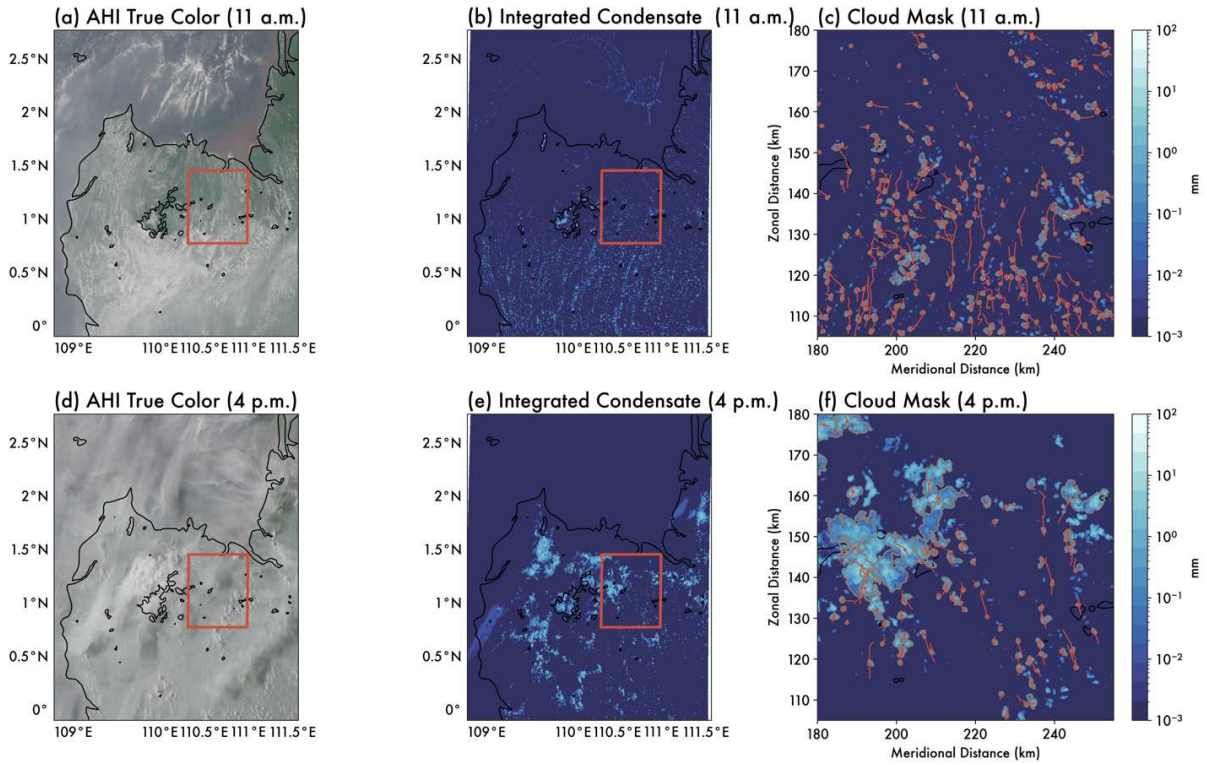

Figure 4.1. Simulations reproduce the observed diurnal cycle and distribution of convection, shown for 11:00a.m. (a-c) and 4:00p.m. (d-f) on 17 September 2019. Advanced Himawari Imager (AHI) true color imagery (left) compared to integrated condensate from the VEG2019 simulation (center). Black (a,d) and white (b,c,e,f) contours show coastline and 500m a.s.l. The red boxes in (a,b,d,e) indicate the region in (c,f), used to demonstrate the *tobac* cloud identification approach including the center of each cloud object (red circles), trajectory (red lines), and outlines of the cloud masks (gray contours).

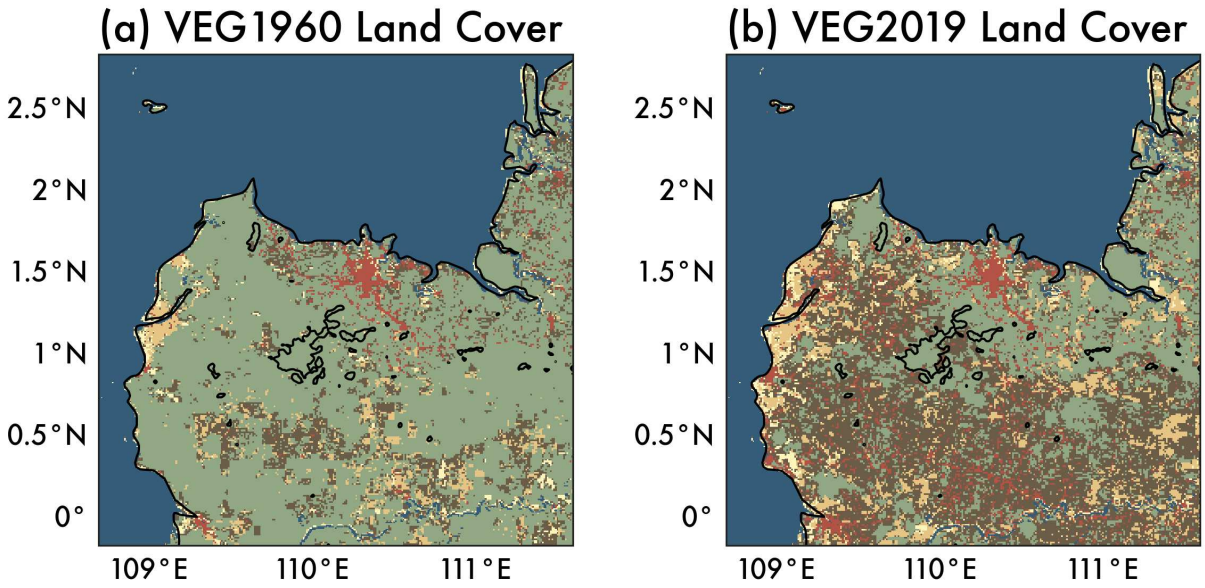

Land Cover Type	Vegetation Height (m)	Albedo	Min. Evaporative Resistance (s m^{-1})
Ocean	–	–	–
Evergreen broadleaf forest	32	0.15	500
Wooded grassland	7	0.18	100
Crop/mixed farming	1	0.18	100
Short grass	0.3	0.26	100
Urban	6	0.18	500

Figure 4.2. Model land cover set-up for (a) VEG1960 and (b) VEG2019. Black contours show the coastline and topography at 500m a.s.l. Legend shows land surface properties in LEAF-3 relevant to this study.

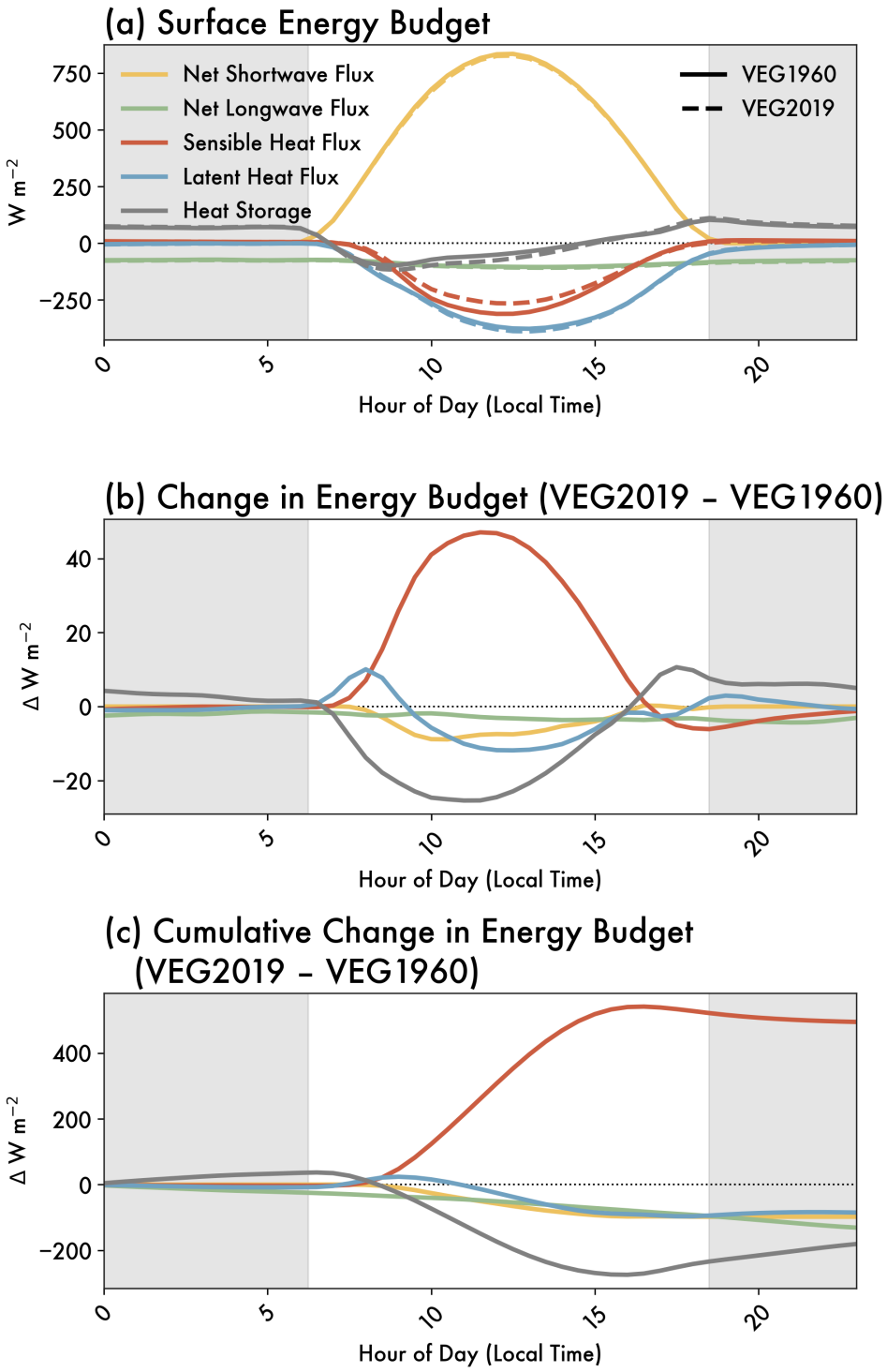

Figure 4.3. Diurnal evolution of the surface energy budget. (a) shows the surface energy budget (averaged over all 3 simulation days), where positive terms heat the surface and negative terms cool the surface. Solid lines are VEG1960, and dashed lines are VEG2019. Differences between VEG2019 and VEG1960 are shown as (b) instantaneous and (c) cumulative changes. Gray shading shows nighttime.

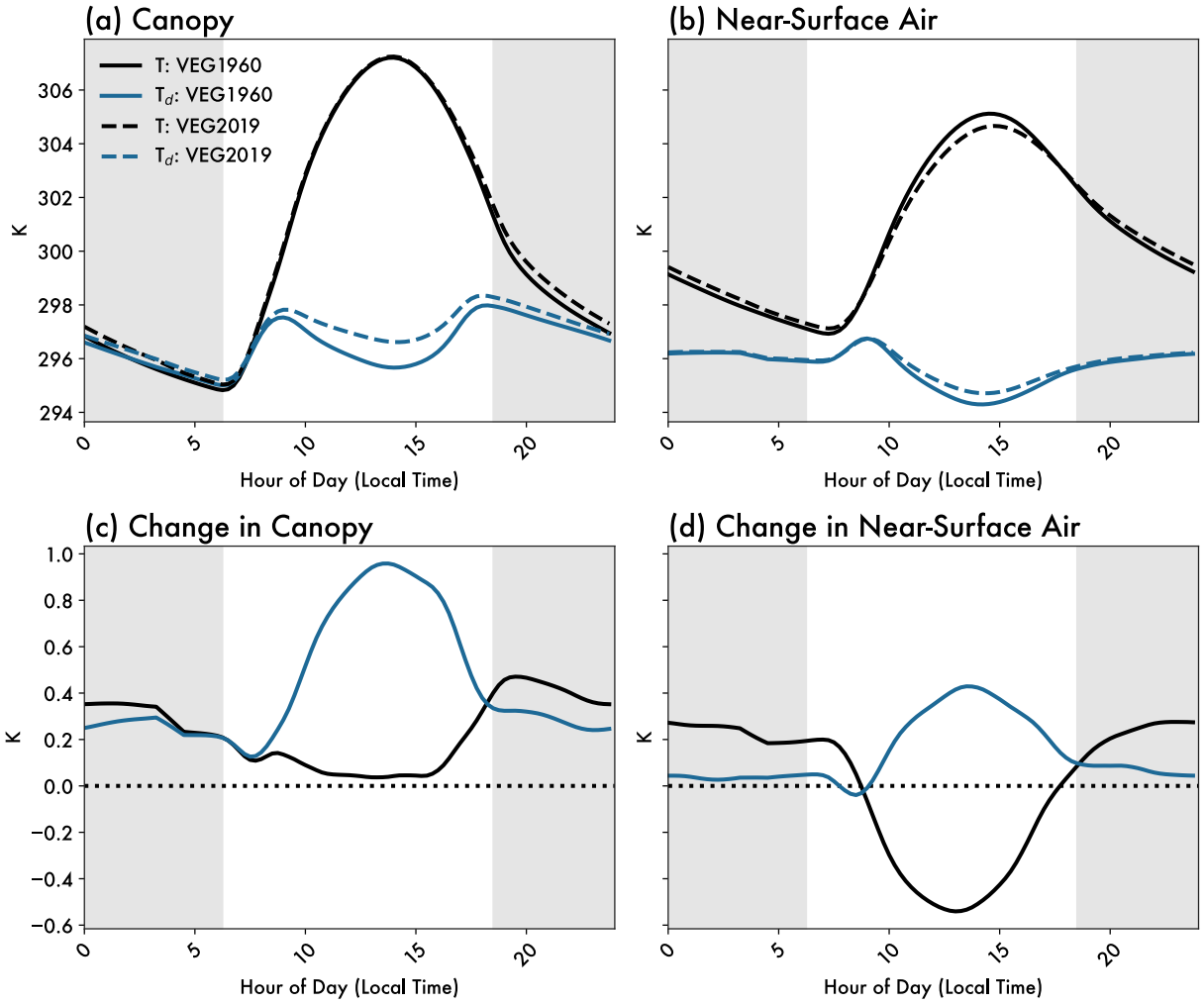

Figure 4.4. Diurnal evolution of air in (a) the vegetation canopy and (b) at the lowest atmospheric level above the surface for temperature (black) and dewpoint (blue). Solid lines are VEG1960, and dashed lines are VEG2019. Differences between VEG2019 and VEG1960 are shown for (c) canopy and (d) near-surface air. Gray shading shows nighttime.

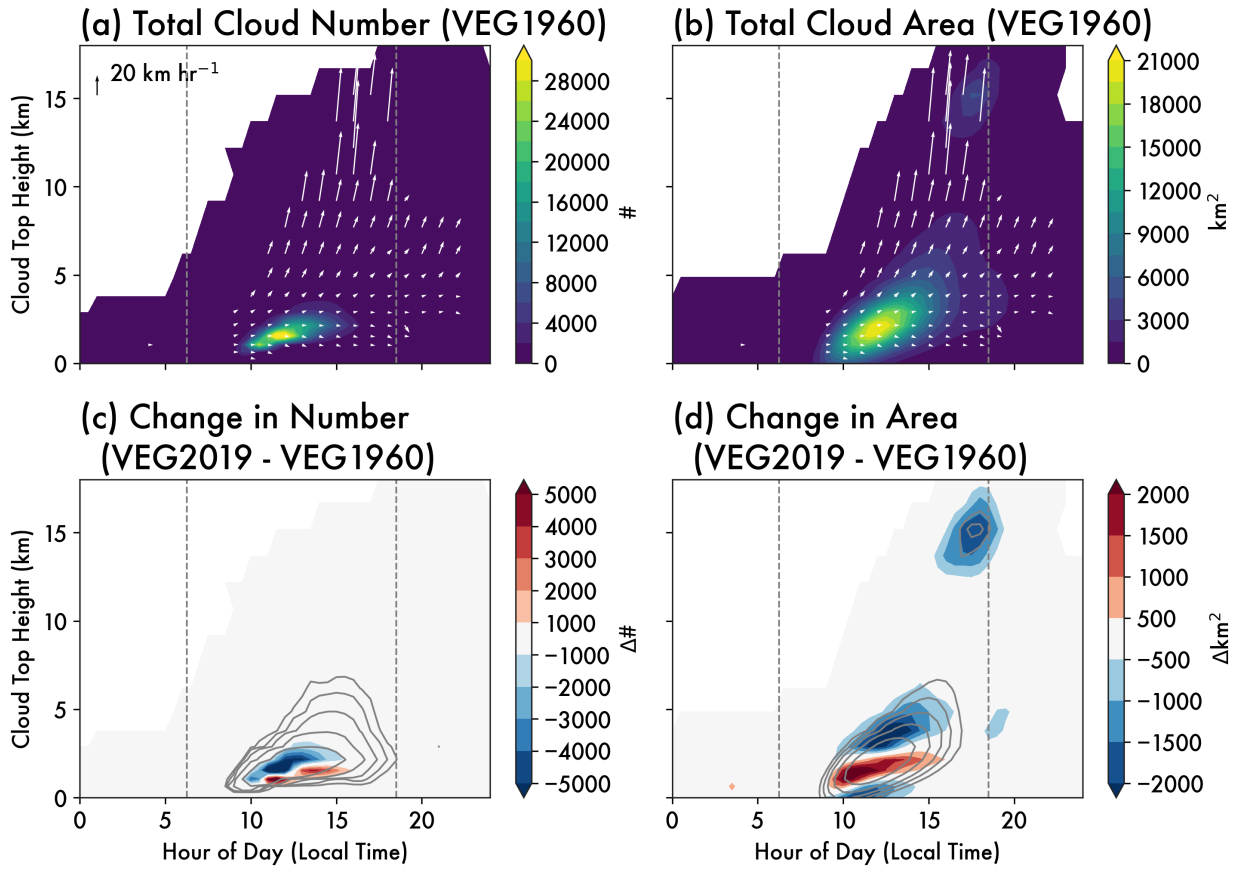

Figure 4.5. Diurnal cycle of total cloud number and area. Color contours show total (a) number and (b) area of *tobac*-tracked clouds for each joint hour of day and cloud top height (CTH) bin in VEG1960. Height of arrows indicate the mean change in CTH for a given (hour of day, CTH) bin, while the length of arrows is arbitrary and uniform. Difference between VEG2019 and VEG1960 is shown for cloud (c) number and (d) area, with the gray contours showing the 90-98th data percentiles from (a,b) to facilitate comparison. Gray vertical lines indicate sunrise and sunset.

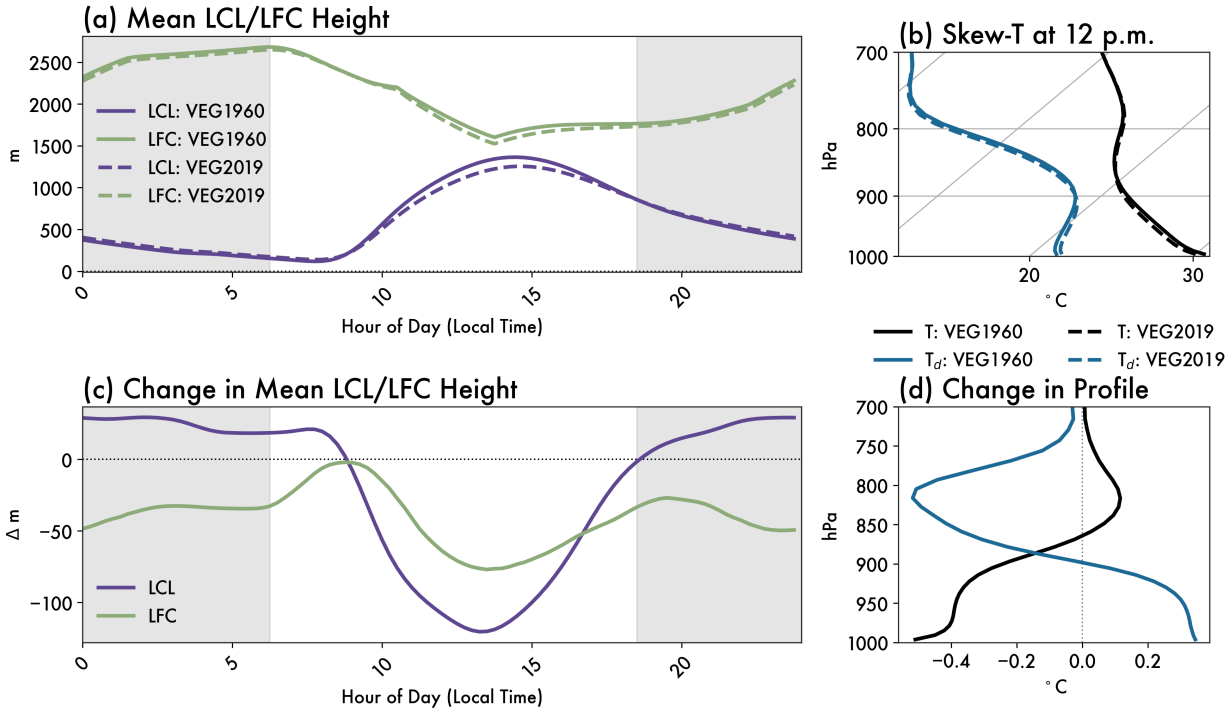

Figure 4.6. Diurnal evolution of the lifted condensation level (LCL) and level of free convection (LFC). (a) shows the LCL height in purple and LFC height in green, and (b) shows the mean skew-T profile at 12p.m., with temperature (black) and dewpoint (blue). Solid lines are VEG1960, and dashed lines are VEG2019. Differences between VEG2019 and VEG1960 are shown for (c) LCL/LFC evolution and (d) atmospheric profile. Gray shading in (a,c) shows nighttime.

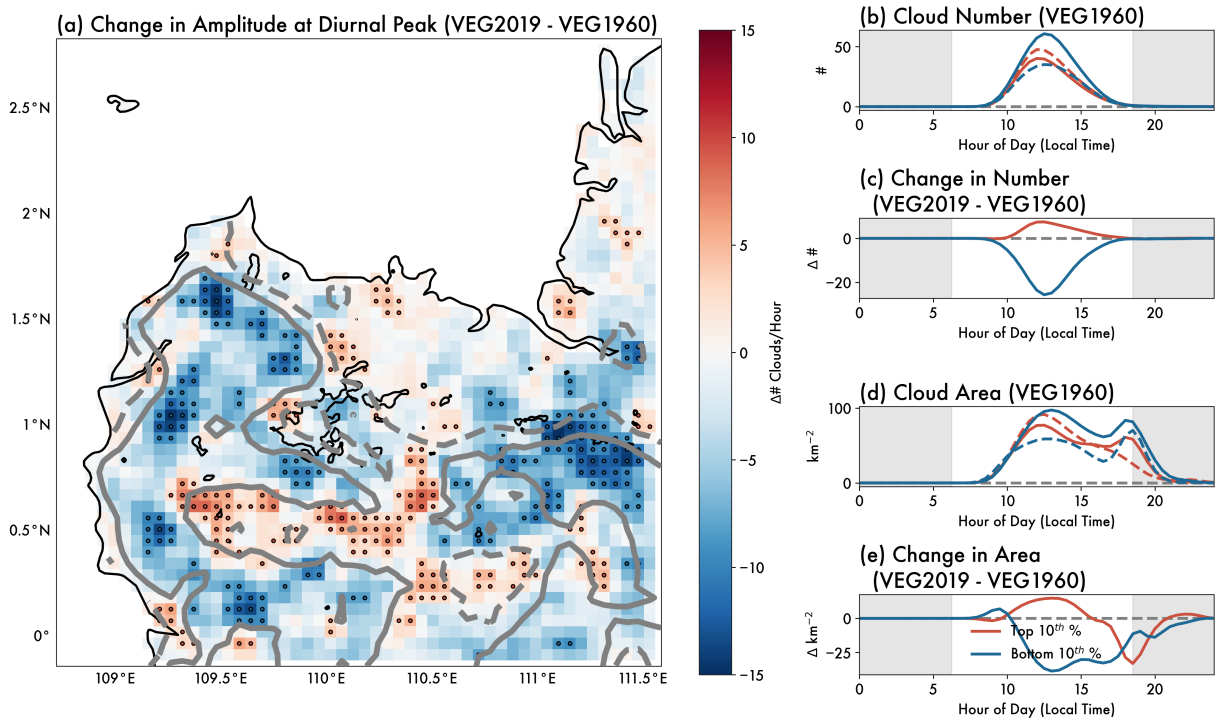

Figure 4.7. Spatial heterogeneity in cloud response to deforestation. (a) shows the difference in the amplitude of the diurnal peak in cloud number between VEG2019 and VEG1960, as described in text. Gray contours show 25% (dashed) and 50% (solid) forest loss between VEG1960 and VEG2019. Black contours show coastline and 500m a.s.l. Circles represent top (red) and bottom (blue) decile of points in terms of the change in the diurnal peak cloud number, which are used for averaging in (b-e). Mean diurnal cycle of cloud (b) number and (d) area are shown for the top / bottom decile of points, with the VEG1960 simulation in solid lines and VEG2019 simulation in dashed lines. Changes are shown as the difference between VEG2019 and VEG1960 for cloud (c) number and (d) area. Gray shading (b-e) shows nighttime.

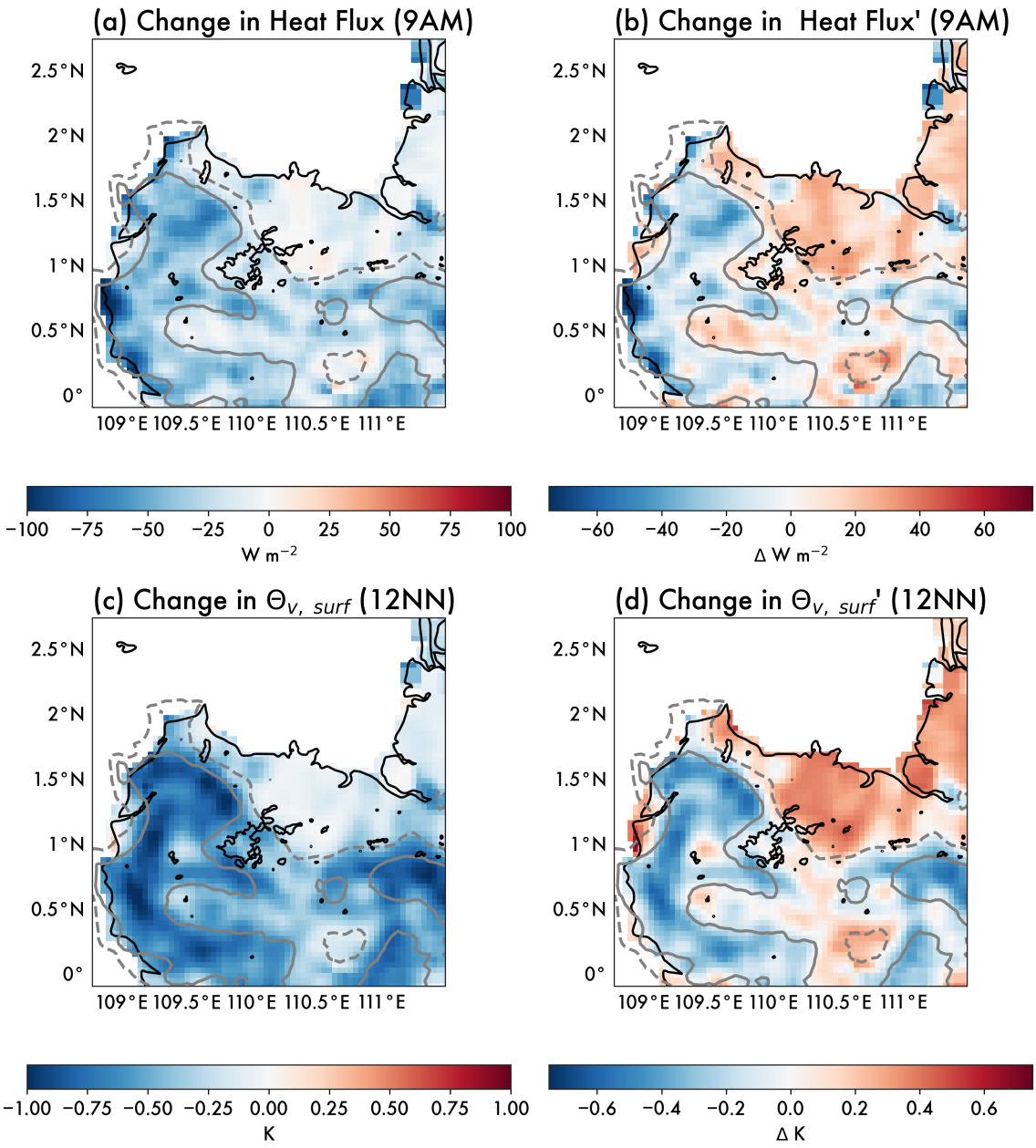

Figure 4.8. Mesoscale solenoidal circulations driven by gradients in surface heat flux and buoyancy. Maps of (a) mean turbulent heat flux (sensible + latent) and (b) perturbation heat flux (perturbation from the spatiotemporal mean for the given hour) from 8:30-9:30a.m., prior to the onset of convection. (c) and (d) show the same for the near surface virtual potential temperature from 11:30a.m.-12:30p.m. Gray contours show 25% (dashed) and 50% (solid) forest loss between VEG1960 and VEG2019. Black contours show coastline and 500m a.s.l.

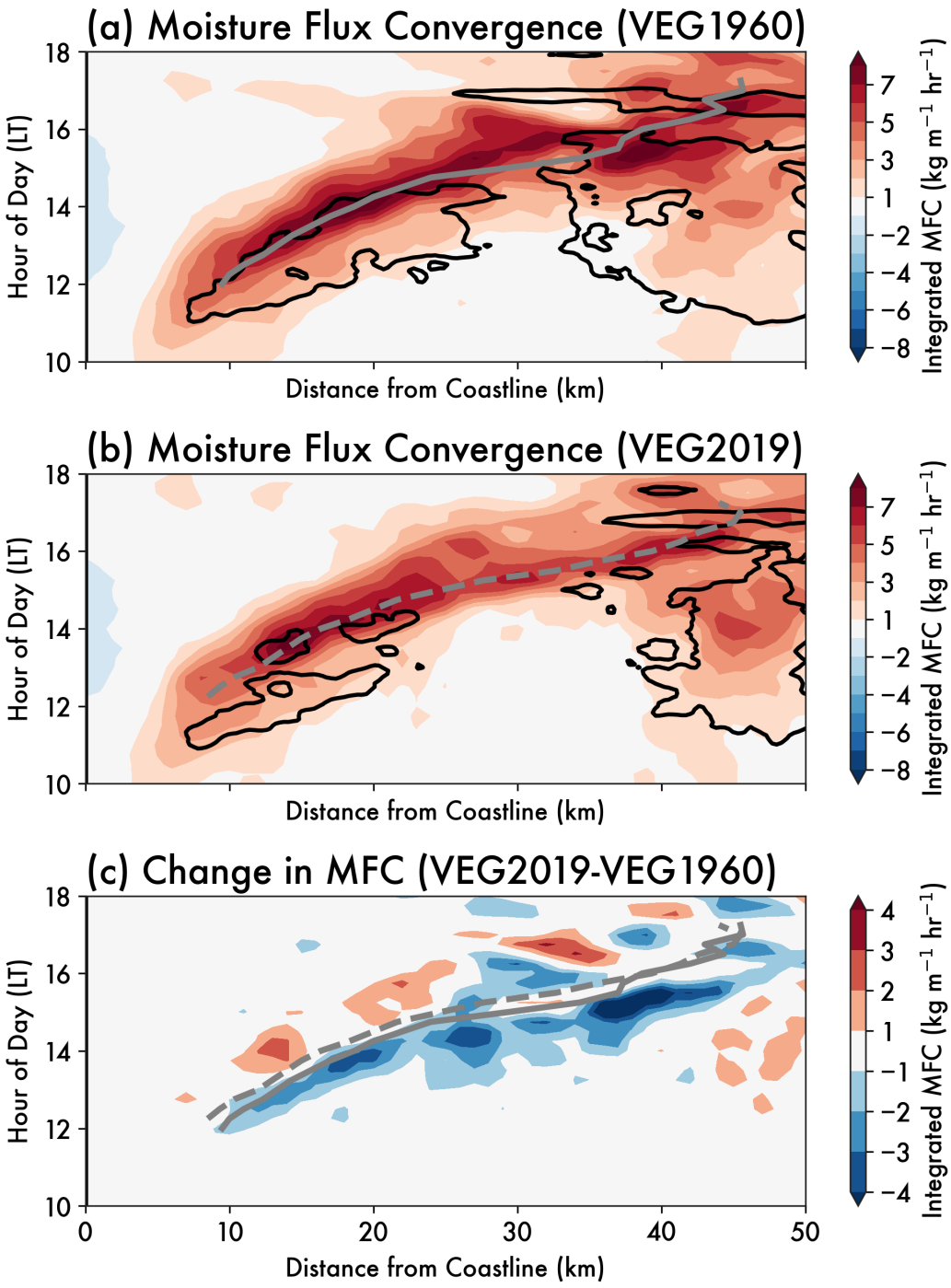

Figure 4.9. Hovmöller plot showing the sea breeze propagation and associated moisture flux convergence (MFC) and cloud cover for (a) VEG1960, (b) VEG2019, and (c) the difference between VEG2019 and VEG1960**.** Color shading in (a) and (b) shows integrated MFC (surface– 1km), as a function of distance from coastline and hour of the day. Black contours show the same for a cloud fraction of 0.075. Gray lines show the location of peak MFC for each time in VEG1960 (solid) and VEG2019 (dashed). Data are smoothed using a rolling 3km window for clarity.

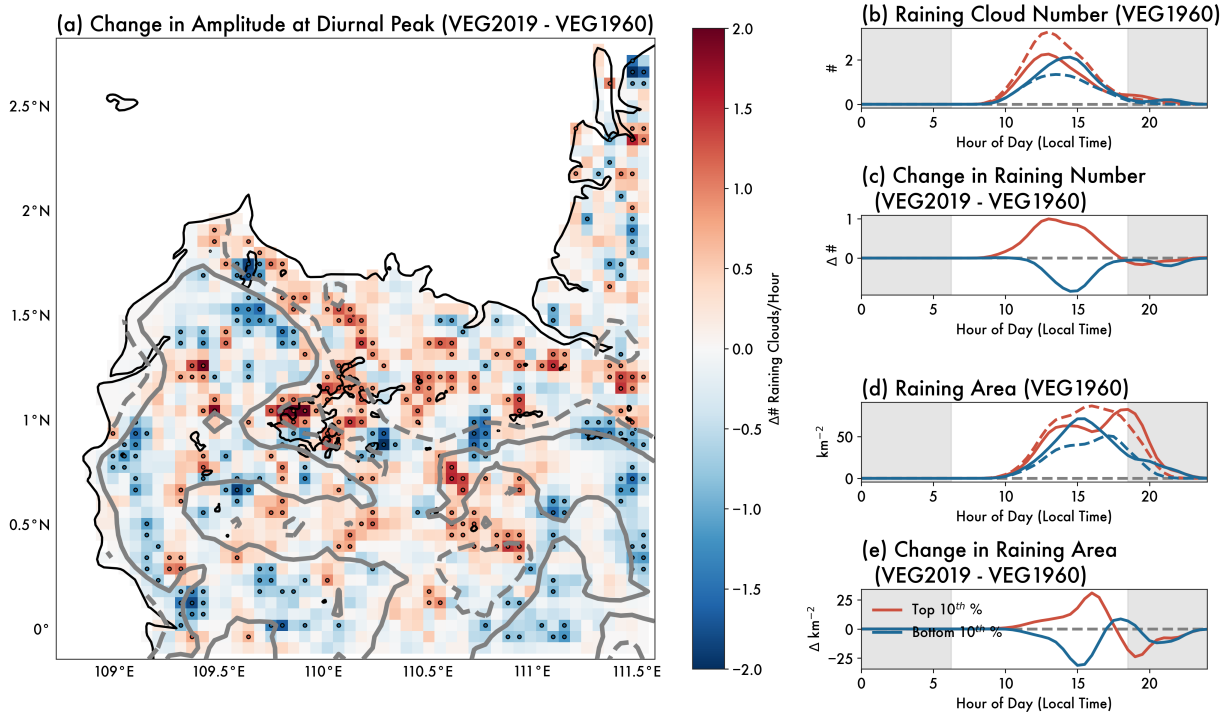

Figure 4.10. Spatial heterogeneity in raining cloud response to deforestation. As in Figure 4.7, but only for precipitating clouds (rain rate>0.01 mm hr^{-1}).

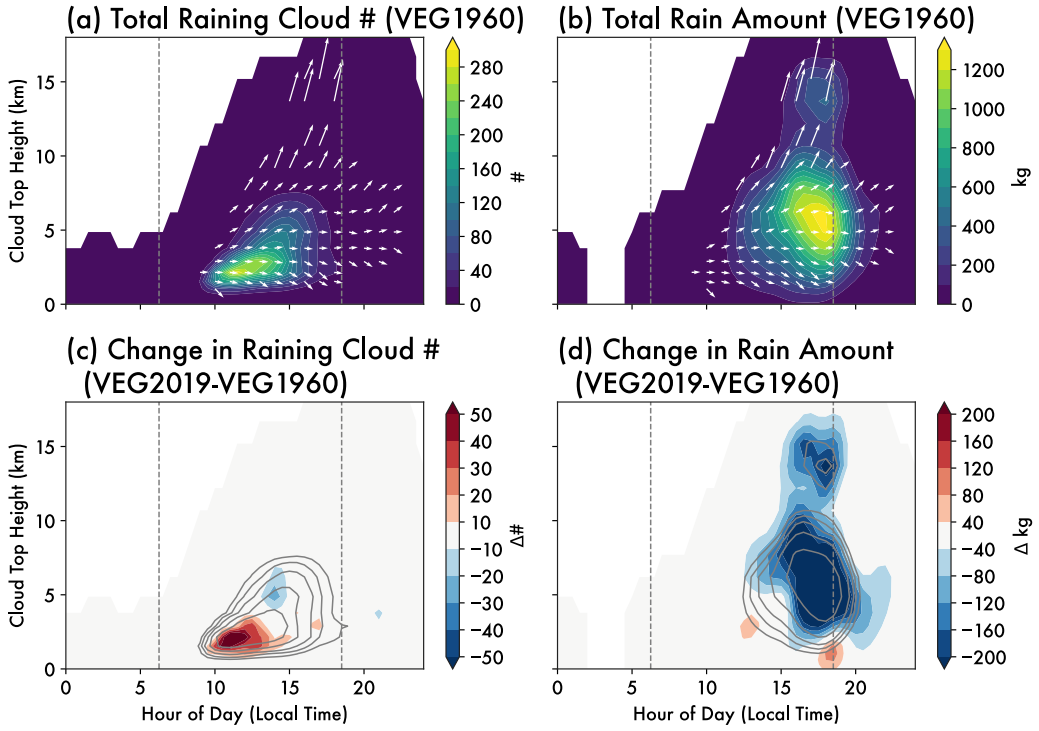

Figure 4.11. Diurnal cycle of (a) number of raining clouds and (b) total rain amount. As in Figure 4.5, but only for precipitating clouds (rain rate>0.01 mm hr^{-1}). Total rain amount (b,d) is integrated over cloud area.

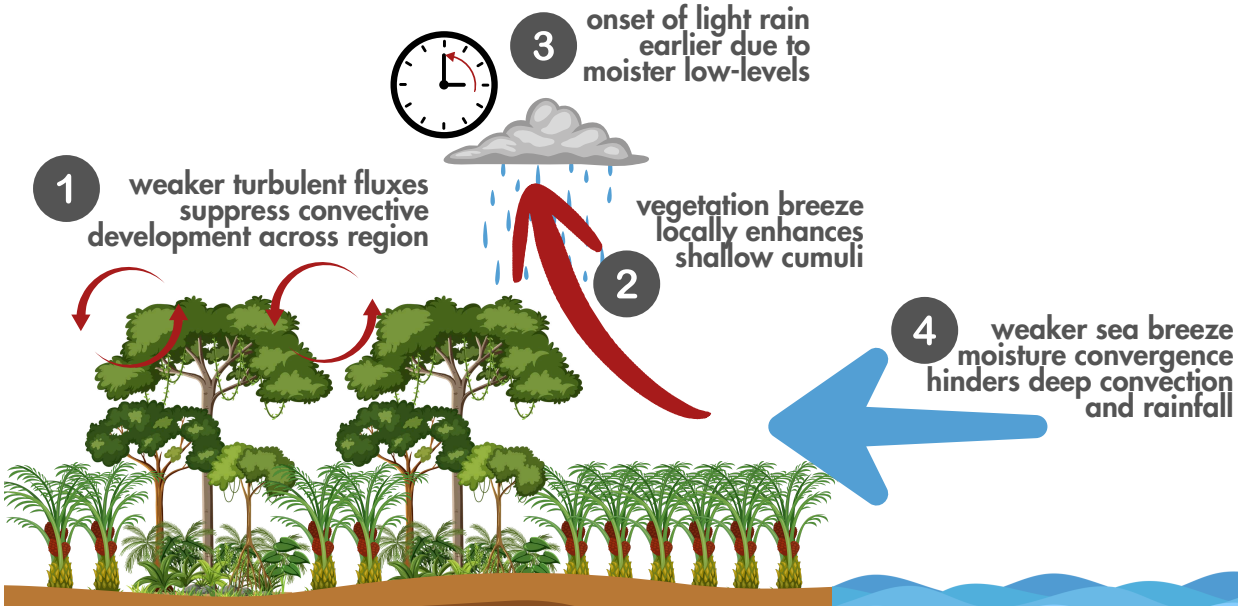

Figure 4.12. Schematic of major processes impacting the cloud response to deforestation over Borneo. As intact tropical rainforest is replaced by palm oil plantations, turbulent exchanges between the land and atmosphere are reduced across the region, which suppresses convective development overall (1). However, along the border of deforested areas, vegetation breezes can locally enhance midday shallow cumuli (2). Shallow cumuli which do form around midday tend to start raining earlier in the day (3) due to the moister low-level atmosphere from enhanced evapotranspiration. The large-scale changes to the near-surface atmosphere over land weaken moisture flux convergence from the sea breeze, which hinders the development of deep convection and associated precipitation in the evening (4).

CHAPTER 5 : CONCLUSIONS

5.1 Summary and implications of key findings

The overarching goal of this dissertation was to develop a more nuanced process-level understanding of how perturbations to aerosol and land surface properties impact tropical convection. We employ a range of approaches, from idealized model experiments (Chapter 2) to realistic large-domain simulations (Chapter 4) to analyses of long-term satellite data (Chapter 3). Across this dissertation, we use Lagrangian object-tracking techniques and sophisticated statistical frameworks to assess shifts in the overall cloud distribution in response to aerosol and land surface changes. In doing so, we not only aim to better quantify shifts in cloud processes but also assess when and where changes to land–aerosol–cloud interactions are the greatest and thus where aerosol and land surface perturbations have the greatest impact overall.

In Chapter 2, we assessed aerosol impacts on rainfall and aerosol convective transport using a suite of idealized simulations with varied aerosol loading and chemical composition. From this work, we drew the following conclusions:

1. Increasing aerosol loading has opposing impacts on precipitation from shallow cumulus and congestus: shallow cumuli tend to grow taller and rain less or not at all, whereas congestus tend to only grow slightly taller but have greater rain rates.
2. The trends in shallow cumulus and congestus rainfall are remarkably consistent across aerosol chemical compositions. However, the net precipitation response is mixed and, in many cases non-monotonic, since it depends on the relative proportion of shallow cumulus to congestus.

3. Regardless of the precipitation response, increasing aerosol loading hinders the ability of shallow cumulus and congestus to remove aerosol via rainout. In a polluted environment, the aerosol loading is not only greater than in a pristine environment, but clouds are also less able to regulate those aerosol loadings by rainout. Instead, boundary layer aerosol is convectively transported and detrained aloft in the free troposphere, where aerosol particles remain available for further aerosol–cloud interactions.

In Chapter 3, we turned our attention to quantifying deforestation impacts on clouds over Southeast Asia. The sign of this impact has been debated in many regional and climate modeling studies but remains poorly constrained in observations. We used two decades of MODIS data and a statistical attribution technique to quantify the cloud response and find the following:

1. On an annual timescale, forest loss in Southeast Asia drives a robust shift toward more widespread and shallower clouds during the daytime over deforested areas that are in close proximity to intact forests.
2. The cloud response to deforestation is amplified in dry, inland regions compared to moist, coastal regions. This suggests that in areas where moisture is more limited, mesoscale circulations arising from gradients in surface properties between forested and deforested regions can be important local drivers of moisture convergence driving cloud formation.
3. We find that the cloud fraction response to forest loss is not sensitive to aerosol optical depth (AOD) for the observed range of AODs. However, increased AOD can offset or mask deforestation impacts on cloud top heights.

The work in Chapter 3 quantified land surface impacts on cloud properties on an annual timescale. We then further investigated the physical mechanisms driving these impacts on daily scales in Chapter 4. We used a pair of high-resolution, large-domain simulations to explore the

interplay between convective and mesoscale processes that determine the cloud response to deforestation over northwestern Borneo. Based on this work, we conclude:

1. The widespread replacement of intact broadleaf forest with oil palm plantations drives a robust response in the surface energy budget associated with decreased surface roughness and weaker evaporative resistance. Deforestation decreases surface sensible heat fluxes, which is compensated by increased soil and vegetation warming and a corresponding enhancement of evapotranspiration and surface latent heat fluxes.
2. Over the whole domain, deforestation decreases shallow cloud cover due to reduced boundary layer growth and increased convective inhibition. However, cloudiness is enhanced in areas where there is a strong gradient in forest cover (i.e., the deforestation boundary) due to enhanced mesoscale vegetation breezes.
3. Deforestation also weakens sea breeze-driven moisture convergence, which hinders the transition from congestus to deep convection in the late afternoon and evening hours. Associated with this, we find that deforestation decreases precipitation overall, and shifts the diurnal peak in rainfall later into the evening.

5.2 Future work

The research in this dissertation has advanced our understanding of the physical processes driving land–aerosol–cloud interactions, particularly how these vary across cloud types in different environments. Our findings also raise numerous questions that could be the subject of future study, including:

- How do convective clouds respond to simultaneous perturbations to aerosol and land surface properties? What are the relative magnitudes of these effects?

- What is the role of convective organization and aggregation on the convective transport and removal of aerosol particles?
- On what timescales do clouds respond to aerosol and land surface perturbations? Are the cloud changes we observe herein transient (i.e., responses that tend to return the system to its initial state) or persistent (i.e., causing long-term shifts in the cloud population)?
- What spatiotemporal scales of aerosol and land surface perturbation are needed to drive responses in convective clouds? How does the degree of heterogeneity in those perturbations impact the cloud response?
- Under what thermodynamic environments do aerosols and land surface changes cause the biggest impact on clouds?
- Do deep convective clouds exhibit the same aerosol impacts on precipitation and convective transport as we see in shallow cumulus and congestus? How are changes to aerosol detrainment and transport different once ice microphysics is involved?
- Which land surface properties are the most important controls on tropical convection?
- How sensitive is the cloud response to deforestation to specific land management practices (e.g., irrigation, spatial pattern of deforestation)?
- Can we use geostationary satellite observations to robustly attribute deforestation impacts on cloud properties across the day?

Our results underscore that the cloud response to perturbations in aerosol and land cover is complex. Quantifying how clouds respond to such perturbations requires careful representation of countless processes which offset one another, many of which occur at spatiotemporal scales not explicitly represented in NWP or climate models. Though the advent of global kilometer-

scale models (Segura et al., 2025) suggests the potential for significant scientific advancement—particularly in resolving multiscale interactions—many of our results highlight the importance of shallow cumuli that are not sufficiently resolved at km-scale resolutions. For example, without representing the shallow cumulus mode, our results in Chapter 2 would not capture the non-monotonic precipitation response to aerosols or the associated feedbacks on aerosol removal. Similarly, we showed in Chapter 3 and 4 that shallow clouds are the most sensitive to changes in land cover; without including this shallow cloud response (and its spatial variability), our estimates for the cloud response to deforestation would be vastly different. Developing parameterizations that better capture these variable land–aerosol–cloud interactions is thus still of great importance. Characterizing the robust physical processes driving cloud responses—and quantifying the environmental and cloud properties that are most important for those processes—as we have done in this dissertation, is the first step towards building, assessing, and refining parameterizations that are able to account for differences in convective processes across cloud types and environments.

Additionally, observations of land–aerosol–cloud interactions are needed to evaluate the physical mechanisms driving these interactions that we propose in this dissertation. Using observations to robustly attribute changes in cloud properties to aerosol and land surface perturbations is challenging, but, as this dissertation has shown, is certainly possible—particularly by leveraging the ever-growing satellite data record. As cloud object identification and tracking tools advance, the work herein has developed new analytical frameworks to best leverage this object-based information towards improving process-level understanding. These methods will contribute to improving model–observation comparisons, which will be especially useful in the context of upcoming satellite missions like INCUS (NASA Investigating

Convective UpdraftS; van den Heever, 2021). INCUS will collect unprecedented data on convective dynamics in the tropics, and by taking an object-based, storm-centered approach, will provide new opportunities to address the questions on land–aerosol–cloud interactions raised by this dissertation (in addition to many other outstanding questions about the nature of tropical convection) across a wide array of environments.

REFERENCES

Ackerman, A. S., Toon, O. B., Stevens, D. E., Heymsfield, A. J., Ramanathan, V., & Welton, E. J. (2000). Reduction of Tropical Cloudiness by Soot. *Science*, *288*(5468), 1042–1047. https://doi.org/10.1126/science.288.5468.1042

Adler, R. F., & Mack, R. A. (1984). Thunderstorm Cloud Height–Rainfall Rate Relations for Use with Satellite Rainfall Estimation Techniques. *Journal of Climate and Applied Meteorology*, *23*(2), 280–296.

Aitken, J. (1917). Some nuclei of cloudy condensation. *Monthly Weather Review*. https://doi.org/10.1175/1520-0493(1917)45<452a:SNOCC>2.0.CO;2

Albrecht, B. A. (1989). Aerosols, Cloud Microphysics, and Fractional Cloudiness. *Science*, *245*(4923), 1227–1230. https://doi.org/10.1126/science.245.4923.1227

Altaratz, O., Koren, I., Remer, L. A., & Hirsch, E. (2014). Review: Cloud invigoration by aerosols—Coupling between microphysics and dynamics. *Atmospheric Research*, *140–141*, 38–60. https://doi.org/10.1016/j.atmosres.2014.01.009

Argüeso, D., Romero, R., & Homar, V. (2020). Precipitation Features of the Maritime Continent in Parameterized and Explicit Convection Models. https://doi.org/10.1175/JCLI-D-19-0416.1

Ascher, B. D., Saleeby, S. M., Marinescu, P. J., & Heever, S. C. van den. (2025). Forest Breeze–Cold Pool Interactions Drive Convective Organization over Heterogeneous Vegetation. https://doi.org/10.1175/JAS-D-24-0084.1

Atwater, M. A. (1970). Planetary Albedo Changes Due to Aerosols. *Science*, *170*(3953), 64–66.

Avila, F. B., Pitman, A. J., Donat, M. G., Alexander, L. V., & Abramowitz, G. (2012). Climate model simulated changes in temperature extremes due to land cover change. *Journal of Geophysical Research: Atmospheres*, *117*(D4). https://doi.org/10.1029/2011JD016382

Baidya Roy, S., & Avissar, R. (2002). Impact of land use/land cover change on regional hydrometeorology in Amazonia. *Journal of Geophysical Research: Atmospheres*, *107*(D20), LBA 4-1-LBA 4-12. https://doi.org/10.1029/2000JD000266

Bardakov, R., Krejci, R., Riipinen, I., & Ekman, A. M. L. (2022). The Role of Convective Up- and Downdrafts in the Transport of Trace Gases in the Amazon. *Journal of Geophysical Research: Atmospheres*, *127*(18), e2022JD037265. https://doi.org/10.1029/2022JD037265

Berg, W., L'Ecuyer, T., & van den Heever, S. (2008). Evidence for the impact of aerosols on the onset and microphysical properties of rainfall from a combination of satellite observations and cloud-resolving model simulations. *Journal of Geophysical Research: Atmospheres*, *113*(D14). https://doi.org/10.1029/2007JD009649

Boucher, O., Randall, D. A., Artaxo, P., Bretherton, C. S., Feingold, G., Forster, P., et al. (2013). Clouds and Aerosols. In *Climate Change 2013: The Physical Science Basis. Contribution of Working Group I to the Fifth Assessment Report of the Intergovernmental Panel on Climate Change* (pp. 571–658). Cambridge: Cambridge University Press. https://doi.org/10.1017/CBO9781107415324.016

Boysen, L. R., Brovkin, V., Pongratz, J., Lawrence, D. M., Lawrence, P., Vuichard, N., et al. (2020). Global climate response to idealized deforestation in CMIP6 models. *Biogeosciences*, *17*(22), 5615–5638. https://doi.org/10.5194/bg-17-5615-2020

Ceppi, P., Brient, F., Zelinka, M. D., & Hartmann, D. L. (2017). Cloud feedback mechanisms and their representation in global climate models. *WIREs Climate Change*, *8*(4), e465. https://doi.org/10.1002/wcc.465

Chen, C.-C., Lo, M.-H., Im, E.-S., Yu, J.-Y., Liang, Y.-C., Chen, W.-T., et al. (2019). Thermodynamic and Dynamic Responses to Deforestation in the Maritime Continent: A Modeling Study. *Journal of Climate*, *32*(12), 3505–3527. https://doi.org/10.1175/JCLI-D-18-0310.1

Chen, F., & Avissar, R. (1994a). Impact of Land-Surface Moisture Variability on Local Shallow Convective Cumulus and Precipitation in Large-Scale Models. *Journal of Applied Meteorology and Climatology*, *33*(12), 1382–1401. https://doi.org/10.1175/1520-0450(1994)033<1382:IOLSMV>2.0.CO;2

Chen, F., & Avissar, R. (1994b). The Impact of Land-Surface Wetness Heterogeneity on Mesoscale Heat Fluxes. *Journal of Applied Meteorology and Climatology*, *33*(11), 1323–1340. https://doi.org/10.1175/1520-0450(1994)033<1323:TIOLSW>2.0.CO;2

Chen, G., Xue, H., Feingold, G., & Zhou, X. (2012). Vertical transport of pollutants by shallow cumuli from large eddy simulations. *Atmospheric Chemistry and Physics*, *12*, 0238. https://doi.org/10.5194/acp-12-11319-2012

Chen, H.-C., & Lo, M.-H. (2023). Contrasting Responses of Surface Heat Fluxes to Tropical Deforestation. *Journal of Geophysical Research: Atmospheres*, *128*(12), e2022JD038118. https://doi.org/10.1029/2022JD038118

Chen, J., Hagos, S., Xiao, H., Fast, J., & Feng, Z. (2023). Multiscale Analysis of Surface Heterogeneity–Induced Convection on Isentropic Coordinates. https://doi.org/10.1175/JAS-D-21-0198.1

Chen, S., Woodcock, C., Dong, L., Tarrio, K., Mohammadi, D., & Olofsson, P. (2024). Review of drivers of forest degradation and deforestation in Southeast Asia. *Remote Sensing Applications: Society and Environment*, *33*, 101129. https://doi.org/10.1016/j.rsase.2023.101129

Cioni, G., & Hohenegger, C. (2017). Effect of Soil Moisture on Diurnal Convection and Precipitation in Large-Eddy Simulations. *Journal of Hydrometeorology*, *18*(7), 1885–1903. https://doi.org/10.1175/JHM-D-16-0241.1

Corr, C. A., Ziemba, L. D., Scheuer, E., Anderson, B. E., Beyersdorf, A. J., Chen, G., et al. (2016). Observational evidence for the convective transport of dust over the Central United States. *Journal of Geophysical Research: Atmospheres*, *121*(3), 1306–1319. https://doi.org/10.1002/2015JD023789

Cotton, W. R., Alexander, G. D., Hertenstein, R., Walko, R. L., McAnelly, R. L., & Nicholls, M. (1995). Cloud venting — A review and some new global annual estimates. *Earth-Science Reviews*, *39*(3–4), 169–206. https://doi.org/10.1016/0012-8252(95)00007-0

Cotton, W. R., Pielke Sr., R. A., Walko, R. L., Liston, G. E., Tremback, C. J., Jiang, H., et al. (2003). RAMS 2001: Current status and future directions. *Meteorology and Atmospheric Physics*, *82*(1). https://doi.org/10.1007/s00703-001-0584-9

Crompton, O., Corrêa, D., Duncan, J., & Thompson, S. (2021). Deforestation-induced surface warming is influenced by the fragmentation and spatial extent of forest loss in Maritime Southeast Asia. *Environmental Research Letters*, *16*(11), 114018. https://doi.org/10.1088/1748-9326/ac2fdc

Cui, Z., & Carslaw, K. S. (2006). Enhanced vertical transport efficiency of aerosol in convective clouds due to increases in tropospheric aerosol abundance. *Journal of Geophysical Research: Atmospheres*, *111*(D15). https://doi.org/10.1029/2005JD006781

Dagan, G. (2022). Equilibrium climate sensitivity increases with aerosol concentration due to changes in precipitation efficiency. *Atmospheric Chemistry and Physics*, *22*(24), 15767–15775. https://doi.org/10.5194/acp-22-15767-2022

Dagan, G., & Stier, P. (2020). Ensemble daily simulations for elucidating cloud–aerosol interactions under a large spread of realistic environmental conditions. *Atmospheric Chemistry and Physics*, *20*(11), 6291–6303. https://doi.org/10.5194/acp-20-6291-2020

Dagan, G., Koren, I., & Altaratz, O. (2015). Aerosol effects on the timing of warm rain processes. *Geophysical Research Letters*, *42*(11), 4590–4598. https://doi.org/10.1002/2015GL063839

Dagan, G., Koren, I., Altaratz, O., & Heiblum, R. H. (2017). Time-dependent, non-monotonic response of warm convective cloud fields to changes in aerosol loading. *Atmospheric Chemistry and Physics*, *17*(12), 7435–7444. https://doi.org/10.5194/acp-17-7435-2017

Dagan, G., Koren, I., Altaratz, O., & Lehahn, Y. (2018). Shallow Convective Cloud Field Lifetime as a Key Factor for Evaluating Aerosol Effects. *iScience*, *10*, 192–202. https://doi.org/10.1016/j.isci.2018.11.032

Davin, E. L., & de Noblet-Ducoudré, N. de. (2010). Climatic Impact of Global-Scale Deforestation: Radiative versus Nonradiative Processes. *Journal of Climate*, *23*(1), 97–112. https://doi.org/10.1175/2009JCLI3102.1

DeMott, P. J., Prenni, A. J., Liu, X., Kreidenweis, S. M., Petters, M. D., Twohy, C. H., et al. (2010). Predicting global atmospheric ice nuclei distributions and their impacts on climate. *Proceedings of the National Academy of Sciences*, *107*(25), 11217–11222. https://doi.org/10.1073/pnas.0910818107

Drager, A. J., Grant, L. D., & Heever, S. C. van den. (2020). Cold Pool Responses to Changes in Soil Moisture. *Journal of Advances in Modeling Earth Systems*, *12*(8), e2019MS001922. https://doi.org/10.1029/2019MS001922

Durieux, L., Machado, L. A. T., & Laurent, H. (2003). The impact of deforestation on cloud cover over the Amazon arc of deforestation. *Remote Sensing of Environment*, *86*(1), 132–140. https://doi.org/10.1016/S0034-4257(03)00095-6

Duveiller, G., Filipponi, F., Ceglar, A., Bojanowski, J., Alkama, R., & Cescatti, A. (2021). Revealing the widespread potential of forests to increase low level cloud cover. *Nature Communications*, *12*(1), 4337. https://doi.org/10.1038/s41467-021-24551-5

Eltahir, E. a. B., & Bras, R. L. (1993). On the response of the tropical atmosphere tio large-scale deforestation. *Quarterly Journal of the Royal Meteorological Society*, *119*(512), 779–793. https://doi.org/10.1002/qj.49711951209

Engström, A., Ekman, A. M. L., Krejci, R., Ström, J., Reus, M. de, & Wang, C. (2008). Observational and modelling evidence of tropical deep convective clouds as a source of mid-tropospheric accumulation mode aerosols. *Geophysical Research Letters*, *35*(23). https://doi.org/10.1029/2008GL035817

Ervens, B., Sorooshian, A., Aldhaif, A. M., Shingler, T., Crosbie, E., Ziemba, L., et al. (2018). Is there an aerosol signature of chemical cloud processing? *Atmospheric Chemistry and Physics*, *18*(21), 16099–16119. https://doi.org/10.5194/acp-18-16099-2018

Falk, N. M., Leung, G. R., Grant, L. D., & Van Den Heever, S. C. (2025). Cold pools reduce the impacts of deforestation on convective initiation.

Fan, J., Yuan, T., Comstock, J. M., Ghan, S., Khain, A., Leung, L. R., et al. (2009). Dominant role by vertical wind shear in regulating aerosol effects on deep convective clouds. *Journal of Geophysical Research: Atmospheres*, *114*(D22). https://doi.org/10.1029/2009JD012352

Fan, J., Wang, Y., Rosenfeld, D., & Liu, X. (2016). Review of Aerosol–Cloud Interactions: Mechanisms, Significance, and Challenges. *Journal of the Atmospheric Sciences*, *73*(11), 4221–4252. https://doi.org/10.1175/JAS-D-16-0037.1

FAO United Nations. (1974). Soil map of the world. Paris: Unesco.

Feingold, G., & Kreidenweis, S. (2000). Does cloud processing of aerosol enhance droplet concentrations? *Journal of Geophysical Research: Atmospheres*, *105*(D19), 24351–24361. https://doi.org/10.1029/2000JD900369

de Filho, F. J. B. O., & Metzger, J. P. (2006). Thresholds in landscape structure for three common deforestation patterns in the Brazilian Amazon. *Landscape Ecology*, *21*(7), 1061–1073. https://doi.org/10.1007/s10980-006-6913-0

Findell, K. L., & Eltahir, E. A. B. (2003). Atmospheric Controls on Soil Moisture–Boundary Layer Interactions. Part I: Framework Development. *Journal of Hydrometeorology*, *4*(3), 552–569. https://doi.org/10.1175/1525-7541(2003)004<0552:ACOSML>2.0.CO;2

Fowler, D., Nemitz, E., Misztal, P., Di Marco, C., Skiba, U., Ryder, J., et al. (2011). Effects of land use on surface–atmosphere exchanges of trace gases and energy in Borneo: comparing fluxes over oil palm plantations and a rainforest. *Philosophical Transactions of the Royal Society B: Biological Sciences*, *366*(1582), 3196–3209. https://doi.org/10.1098/rstb.2011.0055

Frey, R. A., Ackerman, S. A., Liu, Y., Strabala, K. I., Zhang, H., Key, J. R., & Wang, X. (2008). Cloud Detection with MODIS. Part I: Improvements in the MODIS Cloud Mask for Collection 5. *Journal of Atmospheric and Oceanic Technology*, *25*(7), 1057–1072. https://doi.org/10.1175/2008JTECHA1052.1

Friedl, M. A., McIver, D. K., Hodges, J. C. F., Zhang, X. Y., Muchoney, D., Strahler, A. H., et al. (2002). Global land cover mapping from MODIS: algorithms and early results. *Remote Sensing of Environment*, *83*(1), 287–302. https://doi.org/10.1016/S0034-4257(02)00078-0

Gentine, P., Holtslag, A. A. M., D'Andrea, F., & Ek, M. (2013). Surface and Atmospheric Controls on the Onset of Moist Convection over Land. *Journal of Hydrometeorology*, *14*(5), 1443–1462. https://doi.org/10.1175/JHM-D-12-0137.1

Gentine, P., Massmann, A., Lintner, B. R., Hamed Alemohammad, S., Fu, R., Green, J. K., et al. (2019). Land–atmosphere interactions in the tropics – a review. *Hydrology and Earth System Sciences*, *23*(10), 4171–4197. https://doi.org/10.5194/hess-23-4171-2019

Gero, A. F., & Pitman, A. J. (2006). The Impact of Land Cover Change on a Simulated Storm Event in the Sydney Basin. *Journal of Applied Meteorology and Climatology*, *45*(2), 283–300. https://doi.org/10.1175/JAM2337.1

Giambelluca, T. W., Mudd, R. G., Liu, W., Ziegler, A. D., Kobayashi, N., Kumagai, T., et al. (2016). Evapotranspiration of rubber (Hevea brasiliensis) cultivated at two plantation sites in Southeast Asia. *Water Resources Research*, *52*(2), 660–679. https://doi.org/10.1002/2015WR017755

Gibson, L., Lee, T. M., Koh, L. P., Brook, B. W., Gardner, T. A., Barlow, J., et al. (2011). Primary forests are irreplaceable for sustaining tropical biodiversity. *Nature*, *478*(7369), 378–381. https://doi.org/10.1038/nature10425

Glassmeier, F., & Lohmann, U. (2016). Constraining Precipitation Susceptibility of Warm-, Ice-, and Mixed-Phase Clouds with Microphysical Equations. *Journal of the Atmospheric Sciences*, *73*(12), 5003–5023. https://doi.org/10.1175/JAS-D-16-0008.1

Grant, L. D., & van den Heever, S. C. (2014). Aerosol-cloud-land surface interactions within tropical sea breeze convection. *Journal of Geophysical Research: Atmospheres*, *119*(13), 8340–8361. https://doi.org/10.1002/2014JD021912

Gryspeerdt, E., Stier, P., & Partridge, D. G. (2014). Satellite observations of cloud regime development: the role of aerosol processes. *Atmospheric Chemistry and Physics*, *14*(3), 1141–1158. https://doi.org/10.5194/acp-14-1141-2014

Hansen, M. C., Potapov, P. V., Moore, R., Hancher, M., Turubanova, S. A., Tyukavina, A., et al. (2013). High-Resolution Global Maps of 21st-Century Forest Cover Change. *Science*. https://doi.org/10.1126/science.1244693

Hardwick, S. R., Toumi, R., Pfeifer, M., Turner, E. C., Nilus, R., & Ewers, R. M. (2015). The relationship between leaf area index and microclimate in tropical forest and oil palm plantation: Forest disturbance drives changes in microclimate. *Agricultural and Forest Meteorology*, *201*, 187–195. https://doi.org/10.1016/j.agrformet.2014.11.010

Haywood, James M., & Boucher, O. (2000). Estimates of the direct and indirect radiative forcing due to tropospheric aerosols: A review. *Reviews of Geophysics*, *38*(4), 513–543. https://doi.org/10.1029/1999RG000078

Haywood, Jim M., Jones, A., Bellouin, N., & Stephenson, D. (2013). Asymmetric forcing from stratospheric aerosols impacts Sahelian rainfall. *Nature Climate Change*, *3*(7), 660–665. https://doi.org/10.1038/nclimate1857

van den Heever, S. C. (2021). NASA Selects New Mission to Study Storms, Impacts on Climate Models - NASA. Retrieved April 12, 2025, from https://www.nasa.gov/news-release/nasa-selects-new-mission-to-study-storms-impacts-on-climate-models/

van den Heever, S. C., Stephens, G. L., & Wood, N. B. (2011). Aerosol Indirect Effects on Tropical Convection Characteristics under Conditions of Radiative–Convective Equilibrium. *Journal of the Atmospheric Sciences*, *68*(4), 699–718. https://doi.org/10.1175/2010JAS3603.1

Hegg, D. A., Covert, D. S., Jonsson, H., Khelif, D., & Friehe, C. A. (2004). Observations of the impact of cloud processing on aerosol light-scattering efficiency. *Tellus B*, *56*(3), 285–293. https://doi.org/10.1111/j.1600-0889.2004.00099.x

Heikenfeld, M., Marinescu, P. J., Christensen, M., Watson-Parris, D., Senf, F., van den Heever, S. C., & Stier, P. (2019). tobac 1.2: towards a flexible framework for tracking and analysis of clouds in diverse datasets. *Geoscientific Model Development*, *12*(11), 4551–4570. https://doi.org/10.5194/gmd-12-4551-2019

Herbener, S. R., Saleeby, S. M., van den Heever, S. C., & Twohy, C. H. (2016). Tropical storm redistribution of Saharan dust to the upper troposphere and ocean surface. *Geophysical Research Letters*, *43*(19), 10,463-10,471. https://doi.org/10.1002/2016GL070262

Herbert, R., Stier, P., & Dagan, G. (2021). Isolating Large-Scale Smoke Impacts on Cloud and Precipitation Processes Over the Amazon With Convection Permitting Resolution. *Journal of Geophysical Research: Atmospheres*, *126*(13), e2021JD034615. https://doi.org/10.1029/2021JD034615

Hersbach, H., Bell, B., Berrisford, P., Hirahara, S., Horányi, A., Muñoz-Sabater, J., et al. (2020). The ERA5 global reanalysis. *Quarterly Journal of the Royal Meteorological Society*, *146*(730), 1999–2049. https://doi.org/10.1002/qj.3803

Hill, G. E. (1974). Factors Controlling the Size and Spacing of Cumulus Clouds as Revealed by Numerical Experiments. Retrieved from https://journals.ametsoc.org/view/journals/atsc/31/3/1520-0469_1974_031_0646_fctsas_2_0_co_2.xml

Houze Jr., R. A., Rasmussen, K. L., Zuluaga, M. D., & Brodzik, S. R. (2015). The variable nature of convection in the tropics and subtropics: A legacy of 16 years of the Tropical Rainfall Measuring Mission satellite. *Reviews of Geophysics*, *53*(3), 994–1021. https://doi.org/10.1002/2015RG000488

Igel, A. L., & van den Heever, S. C. (2021). Invigoration or Enervation of Convective Clouds by Aerosols? *Geophysical Research Letters*, *48*(16), e2021GL093804. https://doi.org/10.1029/2021GL093804

Jamaludin, J., De Alban, J. D. T., Carrasco, L. R., & Webb, E. L. (2022). Spatiotemporal analysis of deforestation patterns and drivers reveals emergent threats to tropical forest landscapes. *Environmental Research Letters*, *17*(5), 054046. https://doi.org/10.1088/1748-9326/ac68fa

Jiang, H., & Feingold, G. (2006). Effect of aerosol on warm convective clouds: Aerosol-cloud-surface flux feedbacks in a new coupled large eddy model. *Journal of Geophysical Research: Atmospheres*, *111*(D1). https://doi.org/10.1029/2005JD006138

Jiang, H., Feingold, G., & Sorooshian, A. (2010). Effect of Aerosol on the Susceptibility and Efficiency of Precipitation in Warm Trade Cumulus Clouds. *Journal of the Atmospheric Sciences*, *67*(11), 3525–3540. https://doi.org/10.1175/2010JAS3484.1

Jiang, J. H., Su, H., Huang, L., Wang, Y., Massie, S., Zhao, B., et al. (2018). Contrasting effects on deep convective clouds by different types of aerosols. *Nature Communications*, *9*(1), 3874. https://doi.org/10.1038/s41467-018-06280-4

Johnson, R. H., Rickenbach, T. M., Rutledge, S. A., Ciesielski, P. E., & Schubert, W. H. (1999). Trimodal Characteristics of Tropical Convection. *Journal of Climate*, *12*, 22.

Jones, W. K., Stengel, M., & Stier, P. (2024). A Lagrangian perspective on the lifecycle and cloud radiative effect of deep convective clouds over Africa. *Atmospheric Chemistry and Physics*, *24*(9), 5165–5180. https://doi.org/10.5194/acp-24-5165-2024

June, T., Meijide, A., Stiegler, C., Kusuma, A. P., & Knohl, A. (2018). The influence of surface roughness and turbulence on heat fluxes from an oil palm plantation in Jambi, Indonesia. *IOP Conference Series: Earth and Environmental Science*, *149*(1), 012048. https://doi.org/10.1088/1755-1315/149/1/012048

Kanae, S., Oki, T., & Musiake, K. (2001). Impact of Deforestation on Regional Precipitation over the Indochina Peninsula. *Journal of Hydrometeorology*, *2*(1), 51–70. https://doi.org/10.1175/1525-7541(2001)002<0051:IODORP>2.0.CO;2

Kaufman, Y. J., & Gao, B.-C. (1992). Remote sensing of water vapor in the near IR from EOS/MODIS. *IEEE Transactions on Geoscience and Remote Sensing*, *30*(5), 871–884. https://doi.org/10.1109/36.175321

Khain, A. P., BenMoshe, N., & Pokrovsky, A. (2008). Factors Determining the Impact of Aerosols on Surface Precipitation from Clouds: An Attempt at Classification. *Journal of the Atmospheric Sciences*, *65*(6), 1721–1748. https://doi.org/10.1175/2007JAS2515.1

Khanna, J., Medvigy, D., Fueglistaler, S., & Walko, R. (2017). Regional dry-season climate changes due to three decades of Amazonian deforestation. *Nature Climate Change*, *7*(3), 200–204. https://doi.org/10.1038/nclimate3226

Kim, D., Wang, C., Ekman, A. M. L., Barth, M. C., & Lee, D.-I. (2014). The responses of cloudiness to the direct radiative effect of sulfate and carbonaceous aerosols. *Journal of Geophysical Research: Atmospheres*, *119*(3), 1172–1185. https://doi.org/10.1002/2013JD020529

Kim, D.-H., Sexton, J. O., & Townshend, J. R. (2015a). Accelerated deforestation in the humid tropics from the 1990s to the 2000s. *Geophysical Research Letters*, *42*(9), 3495–3501. https://doi.org/10.1002/2014GL062777

Kim, D.-H., Sexton, J. O., & Townshend, J. R. (2015b). Accelerated deforestation in the humid tropics from the 1990s to the 2000s. *Geophysical Research Letters*, *42*(9), 3495–3501. https://doi.org/10.1002/2014GL062777

Kim, M. J., Yeh, S.-W., & Park, R. J. (2016). Effects of sulfate aerosol forcing on East Asian summer monsoon for 1985–2010. *Geophysical Research Letters*, *43*(3), 1364–1372. https://doi.org/10.1002/2015GL067124

Kipling, Z., Stier, P., Johnson, C. E., Mann, G. W., Bellouin, N., Bauer, S. E., et al. (2016). What controls the vertical distribution of aerosol? Relationships between process sensitivity in HadGEM3–UKCA and inter-model variation from AeroCom Phase II. *Atmospheric Chemistry and Physics*, *16*(4), 2221–2241. https://doi.org/10.5194/acp-16-2221-2016

Kuang, Z., & Bretherton, C. S. (2006). A Mass-Flux Scheme View of a High-Resolution Simulation of a Transition from Shallow to Deep Cumulus Convection. *Journal of the Atmospheric Sciences*, *63*(7), 1895–1909. https://doi.org/10.1175/JAS3723.1

Kummu, M., & Varis, O. (2011). The world by latitudes: A global analysis of human population, development level and environment across the north–south axis over the past half century. *Applied Geography*, *31*(2), 495–507. https://doi.org/10.1016/j.apgeog.2010.10.009

Laguë, M. M., Swann, A. L. S., & Boos, W. R. (2021). Radiative Feedbacks on Land Surface Change and Associated Tropical Precipitation Shifts. *Journal of Climate*, *34*(16), 6651–6672. https://doi.org/10.1175/JCLI-D-20-0883.1

Lawrence, D., & Vandecar, K. (2015). Effects of tropical deforestation on climate and agriculture. *Nature Climate Change*, *5*(1), 27–36. https://doi.org/10.1038/nclimate2430

L'Ecuyer, T. S., Hang, Y., Matus, A. V., & Wang, Z. (2019). Reassessing the Effect of Cloud Type on Earth's Energy Balance in the Age of Active Spaceborne Observations. Part I: Top of Atmosphere and Surface. *Journal of Climate*, *32*(19), 6197–6217. https://doi.org/10.1175/JCLI-D-18-0753.1

Lee, S. S., Feingold, G., McComiskey, A., Yamaguchi, T., Koren, I., Martins, J. V., & Yu, H. (2014). Effect of gradients in biomass burning aerosol on shallow cumulus convective circulations. *Journal of Geophysical Research: Atmospheres*, *119*(16), 9948–9964. https://doi.org/10.1002/2014JD021819

Lee, S.-S., & Feingold, G. (2010). Precipitating cloud-system response to aerosol perturbations. *Geophysical Research Letters*, *37*(23). https://doi.org/10.1029/2010GL045596

Lee, T.-H., & Lo, M.-H. (2021). The role of El Niño in modulating the effects of deforestation in the Maritime Continent. *Environmental Research Letters*, *16*(5), 054056. https://doi.org/10.1088/1748-9326/abe88e

Leung, G. R., & van den Heever, S. C. (2022). Controls on the Development and Circulation of Terminal versus Transient Congestus Clouds and Implications for Midlevel Aerosol Transport. *Journal of the Atmospheric Sciences*, *79*(11), 3083–3101. https://doi.org/10.1175/JAS-D-21-0314.1

Leung, G. R., & van den Heever, S. C. (2023). Aerosol breezes drive cloud and precipitation increases. *Nature Communications*, *14*(1), 1–8. https://doi.org/10.1038/s41467-023-37722-3

Leung, G. R., Saleeby, S. M., Sokolowsky, G. A., Freeman, S. W., & van den Heever, S. C. (2023). Aerosol–cloud impacts on aerosol detrainment and rainout in shallow maritime tropical clouds. *Atmospheric Chemistry and Physics*, *23*(9), 5263–5278. https://doi.org/10.5194/acp-23-5263-2023

Leung, G. R., Grant, L. D., & van den Heever, S. C. (2024). Deforestation-Driven Increases in Shallow Clouds Are Greatest in Drier, Low-Aerosol Regions of Southeast Asia. *Geophysical Research Letters*, *51*(10), e2023GL107678. https://doi.org/10.1029/2023GL107678

Levy, R. C., Mattoo, S., Munchak, L. A., Remer, L. A., Sayer, A. M., Patadia, F., & Hsu, N. C. (2013). The Collection 6 MODIS aerosol products over land and ocean. *Atmospheric Measurement Techniques*, *6*(11), 2989–3034. https://doi.org/10.5194/amt-6-2989-2013

Li, R. L., Studholme, J. H. P., Fedorov, A. V., & Storelvmo, T. (2022). Precipitation efficiency constraint on climate change. *Nature Climate Change*, *12*(7), 642–648. https://doi.org/10.1038/s41558-022-01400-x

Li, X., Tao, W.-K., Masunaga, H., Gu, G., & Zeng, X. (2013). Aerosol Effects on Cumulus Congestus Population over the Tropical Pacific: A Cloud-Resolving Modeling Study. *Journal of the Meteorological Society of Japan. Ser. II*, *91*(6), 817–833. https://doi.org/10.2151/jmsj.2013-607

Lilly, D. K. (1962). On the numerical simulation of buoyant convection. *Tellus*, *14*(2), 148–172. https://doi.org/10.1111/j.2153-3490.1962.tb00128.x

Liu, H., Guo, J., Koren, I., Altaratz, O., Dagan, G., Wang, Y., et al. (2019). Non-Monotonic Aerosol Effect on Precipitation in Convective Clouds over Tropical Oceans. *Scientific Reports*, *9*(1), 7809. https://doi.org/10.1038/s41598-019-44284-2

Luo, Z., Liu, G. Y., Stephens, G. L., & Johnson, R. H. (2009). Terminal versus transient cumulus congestus: A CloudSat perspective. *Geophysical Research Letters*, *36*(5). https://doi.org/10.1029/2008GL036927

Lutsko, N., Sherwood, S. C., & Zhao, M. (2021). *Precipitation Efficiency and Climate Sensitivity (Invited Chapter for the AGU Geophysical Monograph Series "Clouds and Climate")* (preprint). Climatology (Global Change). https://doi.org/10.1002/essoar.10507822.1

Mahmood, R., Pielke Sr., R. A., Hubbard, K. G., Niyogi, D., Dirmeyer, P. A., McAlpine, C., et al. (2014). Land cover changes and their biogeophysical effects on climate. *International Journal of Climatology*, *34*(4), 929–953. https://doi.org/10.1002/joc.3736

Malkus, J. S. (1952). Recent Advances in the Study of Convective Clouds and their Interaction with the Environment1. *Tellus*, *4*(2), 71–87. https://doi.org/10.1111/j.2153-3490.1952.tb00992.x

Margono, B. A., Potapov, P. V., Turubanova, S., Stolle, F., & Hansen, M. C. (2014). Primary forest cover loss in Indonesia over 2000–2012. *Nature Climate Change*, *4*(8), 730–735. https://doi.org/10.1038/nclimate2277

Marinescu, P. J., van den Heever, S. C., Heikenfeld, M., Barrett, A. I., Barthlott, C., Hoose, C., et al. (2021). Impacts of Varying Concentrations of Cloud Condensation Nuclei on Deep Convective Cloud Updrafts—A Multimodel Assessment. *Journal of the Atmospheric Sciences*, *78*(4), 1147–1172. https://doi.org/10.1175/JAS-D-20-0200.1

Marzuki, M., Yusnaini, H., Ramadhan, R., Tangang, F., Amirudin, A. A. B., Hashiguchi, H., et al. (2022). Characteristics of Precipitation Diurnal Cycle over a Mountainous Area of Sumatra Island including MJO and Seasonal Signatures Based on the 15-Year Optical Rain Gauge Data, WRF Model and IMERG. *Atmosphere*, *13*(1), 63. https://doi.org/10.3390/atmos13010063

Matsui, T., Zhang, S. Q., Lang, S. E., Tao, W.-K., Ichoku, C., & Peters-Lidard, C. D. (2020). Impact of radiation frequency, precipitation radiative forcing, and radiation column aggregation on convection-permitting West African monsoon simulations. *Climate Dynamics*, *55*(1), 193–213. https://doi.org/10.1007/s00382-018-4187-2

May, P. T., Bringi, V. N., & Thurai, M. (2011). Do We Observe Aerosol Impacts on DSDs in Strongly Forced Tropical Thunderstorms? *Journal of the Atmospheric Sciences*, *68*(9), 1902–1910. https://doi.org/10.1175/2011JAS3617.1

McCormick, R. A., & Ludwig, J. H. (1967). Climate Modification by Atmospheric Aerosols. *Science*, *156*(3780), 1358–1359. https://doi.org/10.1126/science.156.3780.1358

Meyers, M. P., Walko, R. L., Harrington, J. Y., & Cotton, W. R. (1997). New RAMS cloud microphysics parameterization. Part II: The two-moment scheme. *Atmospheric Research*, *45*(1), 3–39. https://doi.org/10.1016/S0169-8095(97)00018-5

van der Molen, M. K., Dolman, A., Waterloo, M., & Bruijnzeel, L. (2006). Climate is affected more by maritime than by continental land use change: A multiple scale analysis. *Global and Planetary Change*, *54*(1–2), 128–149. https://doi.org/10.1016/j.gloplacha.2006.05.005

Park, J. M., & van den Heever, S. C. (2022). Weakening of tropical sea breeze convective systems through interactions of aerosol, radiation, and soil moisture. *Atmospheric Chemistry and Physics*, *22*(16), 10527–10549. https://doi.org/10.5194/acp-22-10527-2022

Parker, D., Tosiani, A., Yazid, M., Sari, I. L., Kartika, T., Kustiyo, et al. (2024). Land in limbo: Nearly one third of Indonesia's cleared old-growth forests left idle. *Proceedings of the National Academy of Sciences*, *121*(28), e2318029121. https://doi.org/10.1073/pnas.2318029121

Pielke, R. A., Cotton, W. R., Walko, R. L., Tremback, C. J., Lyons, W. A., Grasso, L. D., et al. (1992). A comprehensive meteorological modeling system—RAMS. *Meteorology and Atmospheric Physics*, *49*(1), 69–91. https://doi.org/10.1007/BF01025401

Pincus, R., Mlawer, E. J., & Delamere, J. S. (2019). Balancing Accuracy, Efficiency, and Flexibility in Radiation Calculations for Dynamical Models. *Journal of Advances in Modeling Earth Systems*, *11*(10), 3074–3089. https://doi.org/10.1029/2019MS001621

Pitman, A. J., de Noblet-Ducoudré, N., Avila, F. B., Alexander, L. V., Boisier, J.-P., Brovkin, V., et al. (2012). Effects of land cover change on temperature and rainfall extremes in multi-model ensemble simulations. *Earth System Dynamics*, *3*(2), 213–231. https://doi.org/10.5194/esd-3-213-2012

Platnick, S., Meyer, K. G., King, M. D., Wind, G., Amarasinghe, N., Marchant, B., et al. (2017). The MODIS Cloud Optical and Microphysical Products: Collection 6 Updates and Examples From Terra and Aqua. *IEEE Transactions on Geoscience and Remote Sensing*, *55*(1), 502–525. https://doi.org/10.1109/TGRS.2016.2610522

Posselt, D. J., van den Heever, S. C., & Stephens, G. L. (2008). Trimodal cloudiness and tropical stable layers in simulations of radiative convective equilibrium. *Geophysical Research Letters*, *35*(8). https://doi.org/10.1029/2007GL033029

Qian, J.-H. (2008). Why Precipitation Is Mostly Concentrated over Islands in the Maritime Continent. *Journal of the Atmospheric Sciences*, *65*(4), 1428–1441. https://doi.org/10.1175/2007JAS2422.1

Rabin, R. M., Stadler, S., Wetzel, P. J., Stensrud, D. J., & Gregory, M. (1990). Observed Effects of Landscape Variability on Convective Clouds. *Bulletin of the American Meteorological Society*. https://doi.org/10.1175/1520-0477(1990)071<0272:OEOLVO>2.0.CO;2

Radke, L. F., Hobbs, P. V., & Eltgroth, M. W. (1980). Scavenging of Aerosol Particles by Precipitation. *Journal of Applied Meteorology (1962-1982)*, *19*(6), 715–722.

Randall, D. A., Bitz, C. M., Danabasoglu, G., Denning, A. S., Gent, P. R., Gettelman, A., et al. (2019). 100 Years of Earth System Model Development. *Meteorological Monographs*, *59*, 12.1-12.66. https://doi.org/10.1175/AMSMONOGRAPHS-D-18-0018.1

Reid, J. S., Maring, H. B., Narisma, G. T., Heever, S. van den, Girolamo, L. D., Ferrare, R., et al. (2023). The coupling between tropical meteorology, aerosol lifecycle, convection, and radiation, during the Cloud, Aerosol and Monsoon Processes Philippines Experiment (CAMP2Ex). *Bulletin of the American Meteorological Society*, *1*(aop). https://doi.org/10.1175/BAMS-D-21-0285.1

Renggono, F., Hashiguchi, H., Fukao, S., Yamanaka, M. D., Ogino, S.-Y., Okamoto, N., et al. (2001). Precipitating clouds observed by 1.3-GHz boundary layer radars in equatorial Indonesia. *Annales Geophysicae*, *19*(8), 889–897. https://doi.org/10.5194/angeo-19-889-2001

Reutter, P., Su, H., Trentmann, J., Simmel, M., Rose, D., Gunthe, S. S., et al. (2009). Aerosol- and updraft-limited regimes of cloud droplet formation: influence of particle number, size and hygroscopicity on the activation of cloud condensation nuclei (CCN). *Atmos. Chem. Phys.*, 14.

Riehl, H., & Malkus, J. S. (1958). On the heat balance in the equatorial trough zone. *Geophysica*, *6*(3–4), 503–558.

Rodell, M., Famiglietti, J. S., Wiese, D. N., Reager, J. T., Beaudoing, H. K., Landerer, F. W., & Lo, M.-H. (2018). Emerging trends in global freshwater availability. *Nature*, *557*(7707), 651–659. https://doi.org/10.1038/s41586-018-0123-1

Rosenfeld, D., Lohmann, U., Raga, G. B., O'Dowd, C. D., Kulmala, M., Fuzzi, S., et al. (2008). Flood or Drought: How Do Aerosols Affect Precipitation? *Science*, *321*(5894), 1309–1313. https://doi.org/10.1126/science.1160606

Rowell, D. P. (2012). Sources of uncertainty in future changes in local precipitation. *Climate Dynamics*, *39*(7), 1929–1950. https://doi.org/10.1007/s00382-011-1210-2

Ruijsch, J., Taylor, C. M., Hutjes, R. W. A., & Teuling, A. J. (2025). Scale-dependent cloud enhancement from land restoration in West African drylands. *Communications Earth & Environment*, *6*(1), 1–11. https://doi.org/10.1038/s43247-025-02154-y

Saad, S. I., Rocha, H. R. da, Dias, M. A. F. S., & Rosolem, R. (2010). Can the Deforestation Breeze Change the Rainfall in Amazonia? A Case Study for the BR-163 Highway Region. *Earth Interactions*. https://doi.org/10.1175/2010EI351.1

Sabajo, C. R., le Maire, G., June, T., Meijide, A., Roupsard, O., & Knohl, A. (2017). Expansion of oil palm and other cash crops causes an increase of land surface temperature in Indonesia. *Biogeosciences*. https://doi.org/10.5194/bg-2017-203

Saleeby, S. M., & Cotton, W. R. (2004). A Large-Droplet Mode and Prognostic Number Concentration of Cloud Droplets in the Colorado State University Regional Atmospheric Modeling System (RAMS). Part I: Module Descriptions and Supercell Test Simulations.

Journal of Applied Meteorology and Climatology, *43*(1), 182–195. https://doi.org/10.1175/1520-0450(2004)043<0182:ALMAPN>2.0.CO;2
Saleeby, S. M., & Cotton, W. R. (2008). A Binned Approach to Cloud-Droplet Riming Implemented in a Bulk Microphysics Model. *Journal of Applied Meteorology and Climatology*, *47*(2), 694–703.
Saleeby, S. M., & van den Heever, S. C. (2013). Developments in the CSU-RAMS Aerosol Model: Emissions, Nucleation, Regeneration, Deposition, and Radiation. *Journal of Applied Meteorology and Climatology*, *52*(12), 2601–2622. https://doi.org/10.1175/JAMC-D-12-0312.1
Saleeby, S. M., Herbener, S. R., Heever, S. C. van den, & L'Ecuyer, T. (2015). Impacts of Cloud Droplet–Nucleating Aerosols on Shallow Tropical Convection. *Journal of Atmospheric Sciences*, *72*(4), 1369–1385. https://doi.org/10.1175/JAS-D-14-0153.1
Samset, B. H., & Myhre, G. (2011). Vertical dependence of black carbon, sulphate and biomass burning aerosol radiative forcing. *Geophysical Research Letters*, *38*(24). https://doi.org/10.1029/2011GL049697
Savre, J. (2021). Formation and maintenance of subsiding shells around non-precipitating and precipitating cumulus clouds. *Quarterly Journal of the Royal Meteorological Society*, *147*(735), 728–745. https://doi.org/10.1002/qj.3942
Schneck, R., & Mosbrugger, V. (2011). Simulated climate effects of Southeast Asian deforestation: Regional processes and teleconnection mechanisms. *Journal of Geophysical Research: Atmospheres*, *116*(D11). https://doi.org/10.1029/2010JD015450
Segura, H., Pedruzo-Bagazgoitia, X., Weiss, P., Müller, S. K., Rackow, T., Lee, J., et al. (2025). nextGEMS: entering the era of kilometer-scale Earth system modeling. *EGUsphere*, 1–39. https://doi.org/10.5194/egusphere-2025-509
Sheffield, A. M., Saleeby, S. M., & van den Heever, S. C. (2015). Aerosol-induced mechanisms for cumulus congestus growth. *Journal of Geophysical Research: Atmospheres*, *120*(17), 8941–8952. https://doi.org/10.1002/2015JD023743
Smagorinsky, J. (1963). General Circulation Experiments with the Primitive Equations. *Monthly Weather Review*. https://doi.org/10.1175/1520-0493(1963)091<0099:GCEWTP>2.3.CO;2
Smalley, K. M., & Rapp, A. D. (2020). The Role of Cloud Size and Environmental Moisture in Shallow Cumulus Precipitation. *Journal of Applied Meteorology and Climatology*, *59*(3), 535–550. https://doi.org/10.1175/JAMC-D-19-0145.1
Sokolowsky, G. A., Freeman, S. W., & van den Heever, S. C. (2022). Sensitivities of Maritime Tropical Trimodal Convection to Aerosols and Boundary Layer Static Stability. *Journal of the Atmospheric Sciences*, *79*(10), 2549–2570. https://doi.org/10.1175/JAS-D-21-0260.1
Sokolowsky, G. A., Freeman, S. W., Jones, W. K., Kukulies, J., Senf, F., Marinescu, P. J., et al. (2024). *tobac* v1.5: introducing fast 3D tracking, splits and mergers, and other enhancements for identifying and analysing meteorological phenomena. *Geoscientific Model Development*, *17*(13), 5309–5330. https://doi.org/10.5194/gmd-17-5309-2024
Song, X.-P., Hansen, M. C., Stehman, S. V., Potapov, P. V., Tyukavina, A., Vermote, E. F., & Townshend, J. R. (2018). Global land change from 1982 to 2016. *Nature*, *560*(7720), 639–643. https://doi.org/10.1038/s41586-018-0411-9

Spill, G., Stier, P., Field, P. R., & Dagan, G. (2019). Effects of aerosol in simulations of realistic shallow cumulus cloud fields in a large domain. *Atmospheric Chemistry and Physics*, *19*(21), 13507–13517. https://doi.org/10.5194/acp-19-13507-2019

Spracklen, D. V., Baker, J. C. A., Garcia-Carreras, L., & Marsham, J. H. (2018). The Effects of Tropical Vegetation on Rainfall. *Annual Review of Environment and Resources*, *43*(1), 193–218. https://doi.org/10.1146/annurev-environ-102017-030136

Stier, P., van den Heever, S. C., Christensen, M. W., Gryspeerdt, E., Dagan, G., Saleeby, S. M., et al. (2024). Multifaceted aerosol effects on precipitation. *Nature Geoscience*, *17*(8), 719–732. https://doi.org/10.1038/s41561-024-01482-6

Storer, R. L., & Heever, S. C. van den. (2013). Microphysical Processes Evident in Aerosol Forcing of Tropical Deep Convective Clouds. *Journal of the Atmospheric Sciences*, *70*(2), 430–446. https://doi.org/10.1175/JAS-D-12-076.1

Strabala, K. I. (2004). MODIS cloud mask user's guide. Retrieved from http://cimss.ssec.wisc.edu/modis1/pdf/CMUSERSGUIDE.PDF

Stull, R. B. (1988). Boundary Layer Clouds. In R. B. Stull (Ed.), *An Introduction to Boundary Layer Meteorology* (pp. 545–585). Dordrecht: Springer Netherlands. https://doi.org/10.1007/978-94-009-3027-8_13

Takahashi, A., Kumagai, T., Kanamori, H., Fujinami, H., Hiyama, T., & Hara, M. (2017). Impact of Tropical Deforestation and Forest Degradation on Precipitation over Borneo Island. *Journal of Hydrometeorology*, *18*(11), 2907–2922. https://doi.org/10.1175/JHM-D-17-0008.1

Takahashi, H. G., Yoshikane, T., Hara, M., Takata, K., & Yasunari, T. (2010). High-resolution modelling of the potential impact of land surface conditions on regional climate over Indochina associated with the diurnal precipitation cycle. *International Journal of Climatology*, *30*(13), 2004–2020. https://doi.org/10.1002/joc.2119

Takanashi, S., Kosugi, Y., Ohkubo, S., Matsuo, N., Tani, M., & Nik, A. R. (2010). Water and heat fluxes above a lowland dipterocarp forest in Peninsular Malaysia. *Hydrological Processes*, *24*(4), 472–480. https://doi.org/10.1002/hyp.7499

Takayabu, Y. N., Shige, S., Tao, W.-K., & Hirota, N. (2010). Shallow and Deep Latent Heating Modes over Tropical Oceans Observed with TRMM PR Spectral Latent Heating Data. *Journal of Climate*, *23*(8), 2030–2046. https://doi.org/10.1175/2009JCLI3110.1

Tang, A. C. I., Stoy, P. C., Hirata, R., Musin, K. K., Aeries, E. B., Wenceslaus, J., et al. (2019). The exchange of water and energy between a tropical peat forest and the atmosphere: Seasonal trends and comparison against other tropical rainforests. *Science of The Total Environment*, *683*, 166–174. https://doi.org/10.1016/j.scitotenv.2019.05.217

Tao, W.-K., Chen, J.-P., Li, Z., Wang, C., & Zhang, C. (2012). Impact of aerosols on convective clouds and precipitation. *Reviews of Geophysics*, *50*(2). https://doi.org/10.1029/2011RG000369

Taylor, C. M., Klein, C., Parker, D. J., Gerard, F., Semeena, V. S., Barton, E. J., & Harris, B. L. (2022). "Late-stage" deforestation enhances storm trends in coastal West Africa. *Proceedings of the National Academy of Sciences*, *119*(2), e2109285119. https://doi.org/10.1073/pnas.2109285119

Ten Hoeve, J. E., Remer, L. A., & Jacobson, M. Z. (2011). Microphysical and radiative effects of aerosols on warm clouds during the Amazon biomass burning season as observed by MODIS: impacts of water vapor and land cover. *Atmospheric Chemistry and Physics*, *11*(7), 3021–3036. https://doi.org/10.5194/acp-11-3021-2011

Teuling, A. J., Taylor, C. M., Meirink, J. F., Melsen, L. A., Miralles, D. G., van Heerwaarden, C. C., et al. (2017). Observational evidence for cloud cover enhancement over western European forests. *Nature Communications*, *8*(1), 14065. https://doi.org/10.1038/ncomms14065

Thriving on Our Changing Planet: A Decadal Strategy for Earth Observation from Space. (2018). Washington, D.C.: National Academies Press. https://doi.org/10.17226/24938

Tokinaga, H., Xie, S.-P., Timmermann, A., McGregor, S., Ogata, T., Kubota, H., & Okumura, Y. M. (2012). Regional Patterns of Tropical Indo-Pacific Climate Change: Evidence of the Walker Circulation Weakening. *Journal of Climate*, *25*(5), 1689–1710. https://doi.org/10.1175/JCLI-D-11-00263.1

Tölle, M. H., Engler, S., & Panitz, H.-J. (2017). Impact of Abrupt Land Cover Changes by Tropical Deforestation on Southeast Asian Climate and Agriculture. *Journal of Climate*, *30*(7), 2587–2600. https://doi.org/10.1175/JCLI-D-16-0131.1

Turubanova, S., Potapov, P. V., Tyukavina, A., & Hansen, M. C. (2018). Ongoing primary forest loss in Brazil, Democratic Republic of the Congo, and Indonesia. *Environmental Research Letters*, *13*(7), 074028. https://doi.org/10.1088/1748-9326/aacd1c

Twohy, C. H., Anderson, B. E., Ferrare, R. A., Sauter, K. E., L'Ecuyer, T. S., van den Heever, S. C., et al. (2017). Saharan dust, convective lofting, aerosol enhancement zones, and potential impacts on ice nucleation in the tropical upper troposphere. *Journal of Geophysical Research: Atmospheres*, *122*(16), 8833–8851. https://doi.org/10.1002/2017JD026933

Twomey, S. (1977). The Influence of Pollution on the Shortwave Albedo of Clouds. *Journal of the Atmospheric Sciences*, *34*(7), 1149–1152. https://doi.org/10.1175/1520-0469(1977)034<1149:TIOPOT>2.0.CO;2

Varble, A. C., Igel, A. L., Morrison, H., Grabowski, W. W., & Lebo, Z. J. (2023). Opinion: A critical evaluation of the evidence for aerosol invigoration of deep convection. *Atmospheric Chemistry and Physics*, *23*(21), 13791–13808. https://doi.org/10.5194/acp-23-13791-2023

Villalba-Pradas, A., & Tapiador, F. J. (2022). Empirical values and assumptions in the convection schemes of numerical models. *Geoscientific Model Development*, *15*(9), 3447–3518. https://doi.org/10.5194/gmd-15-3447-2022

Walko, R. L., Band, L. E., Baron, J., Kittel, T. G. F., Lammers, R., Lee, T. J., et al. (2000). Coupled Atmosphere–Biophysics–Hydrology Models for Environmental Modeling. *Journal of Applied Meteorology and Climatology*, *39*(6), 931–944. https://doi.org/10.1175/1520-0450(2000)039<0931:CABHMF>2.0.CO;2

Wang, J., Chagnon, F. J. F., Williams, E. R., Betts, A. K., Renno, N. O., Machado, L. A. T., et al. (2009). Impact of deforestation in the Amazon basin on cloud climatology. *Proceedings of the National Academy of Sciences*, *106*(10), 3670–3674. https://doi.org/10.1073/pnas.0810156106

Wang, Y., Xia, W., Liu, X., Xie, S., Lin, W., Tang, Q., et al. (2021). Disproportionate control on aerosol burden by light rain. *Nature Geoscience*, *14*(2), 72–76. https://doi.org/10.1038/s41561-020-00675-z

Wang, Y., Xia, W., & Zhang, G. J. (2021). What rainfall rates are most important to wet removal of different aerosol types? *Atmospheric Chemistry and Physics*, *21*(22), 16797–16816. https://doi.org/10.5194/acp-21-16797-2021

Werth, D., & Avissar, R. (2005). The local and global effects of Southeast Asian deforestation. *Geophysical Research Letters*, *32*(20). https://doi.org/10.1029/2005GL022970

Williams, A. I. L., Stier, P., Dagan, G., & Watson-Parris, D. (2022). Strong control of effective radiative forcing by the spatial pattern of absorbing aerosol. *Nature Climate Change*, *12*(8), 735–742. https://doi.org/10.1038/s41558-022-01415-4

Winckler, J., Reick, C. H., & Pongratz, J. (2017). Robust Identification of Local Biogeophysical Effects of Land-Cover Change in a Global Climate Model. *Journal of Climate*, *30*(3), 1159–1176. https://doi.org/10.1175/JCLI-D-16-0067.1

Winkler, K., Fuchs, R., Rounsevell, M., & Herold, M. (2021). Global land use changes are four times greater than previously estimated. *Nature Communications*, *12*(1), 2501. https://doi.org/10.1038/s41467-021-22702-2

Xu, R., Li, Y., Teuling, A. J., Zhao, L., Spracklen, D. V., Garcia-Carreras, L., et al. (2022). Contrasting impacts of forests on cloud cover based on satellite observations. *Nature Communications*, *13*(1), 670. https://doi.org/10.1038/s41467-022-28161-7

Xue, H., Feingold, G., & Stevens, B. (2008). Aerosol Effects on Clouds, Precipitation, and the Organization of Shallow Cumulus Convection. *Journal of the Atmospheric Sciences*, *65*(2), 392–406. https://doi.org/10.1175/2007JAS2428.1

Yang, G.-Y., & Slingo, J. (2001). The Diurnal Cycle in the Tropics. *Monthly Weather Review*. https://doi.org/10.1175/1520-0493(2001)129<0784:TDCITT>2.0.CO;2

Zipperer, W. C. (1993). Deforestation patterns and their effects on forest patches. *Landscape Ecology*, *8*(3), 177–184. https://doi.org/10.1007/BF00125349

APPENDIX 1: SUPPLEMENTAL FIGURES FOR CHAPTER 2

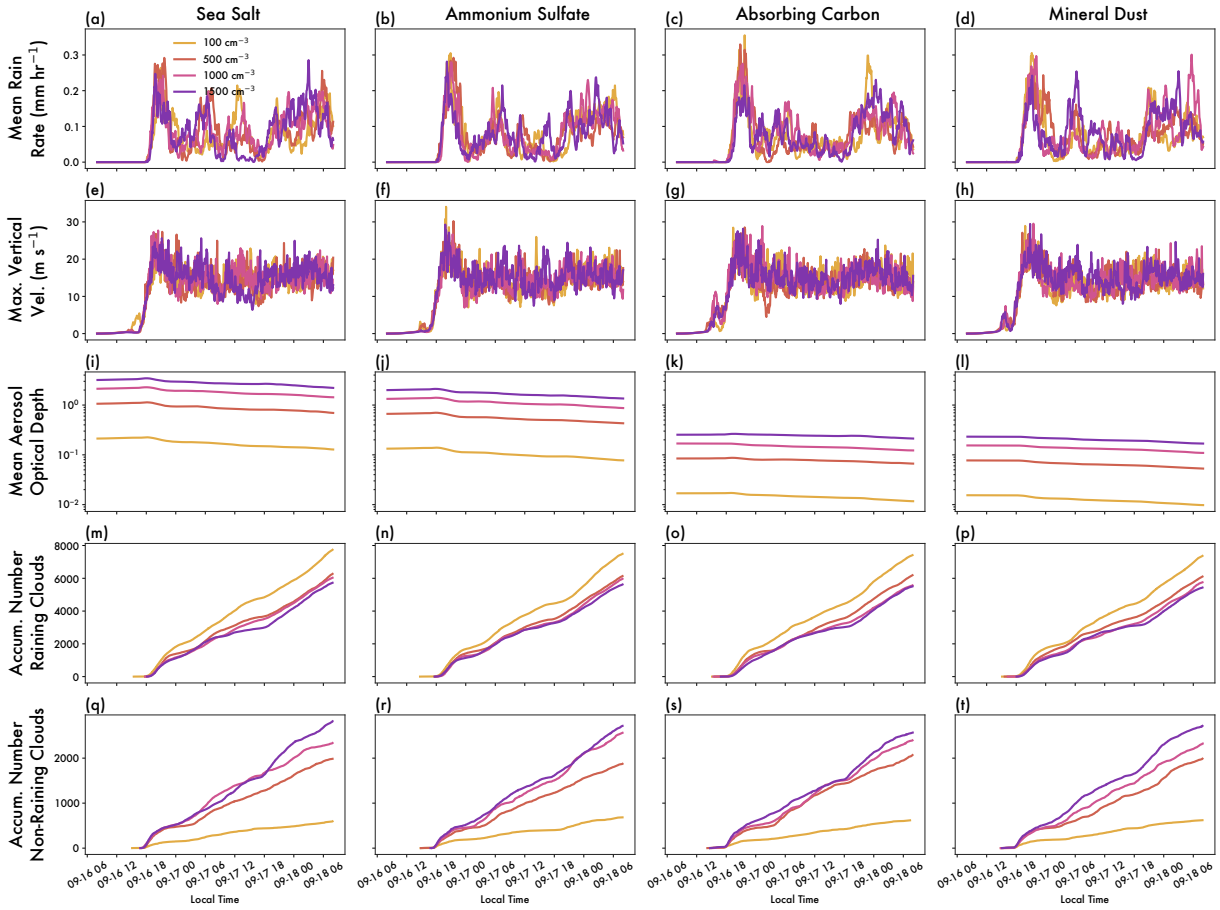

Figure A1.1. Time series of domain-wide properties for each run. Each column represents the indicated aerosol type, and each line represents the indicated initial aerosol loading. Properties shown are (a-d) mean rain rate (mm hr^{-1}), (e-h) maximum vertical velocity (m s^{-1}), (i-l) mean aerosol optical depth, (m-p) accumulated number of raining clouds, and (q-t) accumulated number of non-raining clouds.

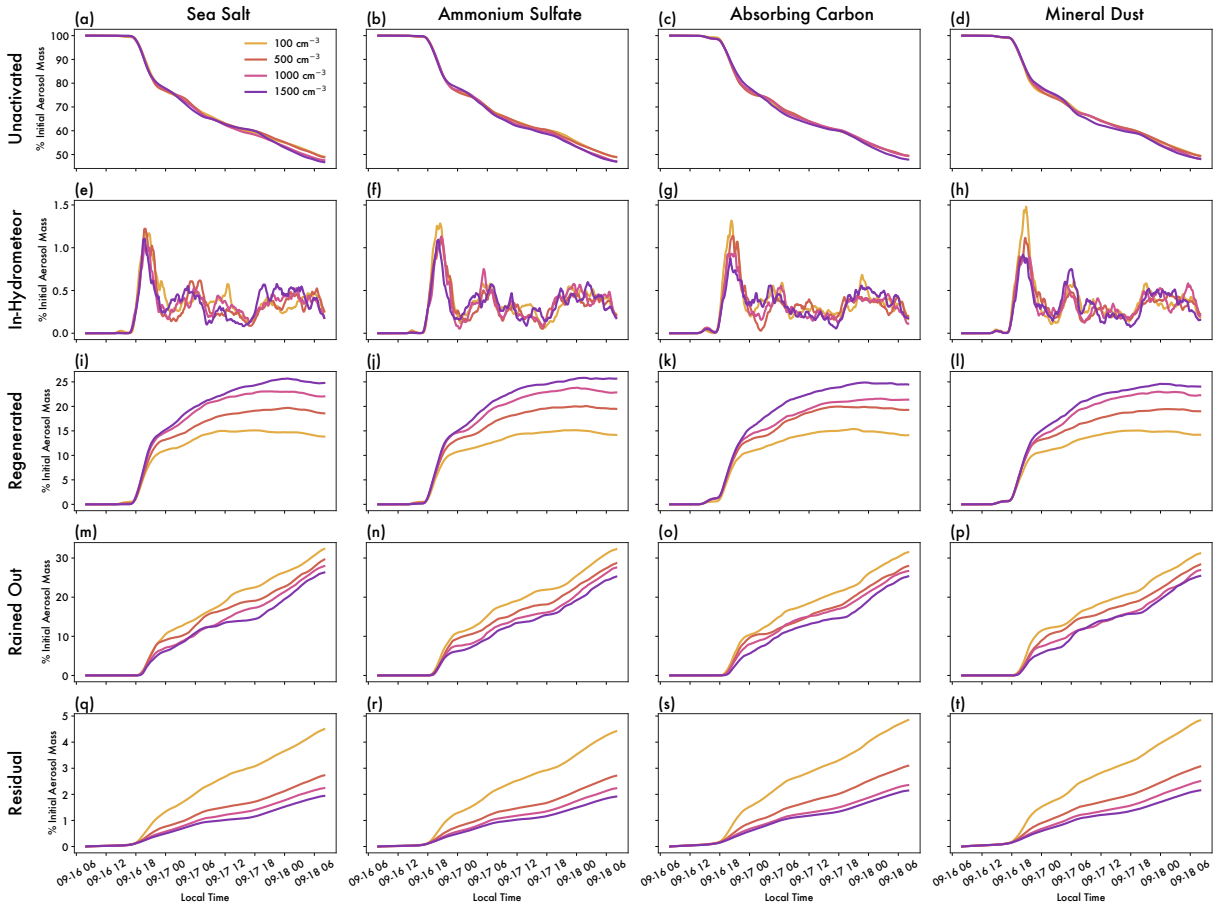

Figure A1.2. Time series of aerosol budget for each run. Each column represents the indicated aerosol type, and each line represents the indicated initial aerosol loading. Properties shown are (a-d) unactivated, (e-h) in-hydrometeor (i-l) regenerated, (m-p) rained-out, and (q-t) residual aerosol. Each aerosol budget term is the domain-integrated aerosol mass in a given category normalized by the total aerosol mass at initialization time.

APPENDIX 2: SUPPORTING INFORMATION FOR CHAPTER 3

A2.1 Detailed methods

A2.1.1 Data sources

We used atmospheric data from the Moderate Resolution Imaging Spectrometer (MODIS) instrument onboard the Terra and Aqua satellites. Terra has an overpass time of 10:30 a.m./p.m., while Aqua has an overpass time of 1:30 a.m./p.m. The four MODIS products utilized were: cloud fraction (CF), cloud top height (CTH), aerosol optical depth (AOD), and precipitable water (PWAT). The cloud retrievals were available at ~1km horizontal resolution during both daytime and nighttime swaths (Platnick et al., 2017). We only use pixels where the cloud mask is confidently or probably cloudy (Frey et al., 2008; Strabala, 2004), though we do acknowledge that clouds potentially missed in this cloud mask (e.g., thin or very small clouds) represent a source of uncertainty in our estimates. The aerosol data are available at ~3km horizontal resolution during daytime swaths using the Dark Target retrieval (Levy et al., 2013), and the moisture data are available at ~1km horizontal resolution during daytime swaths using the near-infrared retrieval (Kaufman & Gao, 1992). We obtained Level 2 swaths for the full time period available (Terra: 2001-2020, Aqua: 2003-2020), and then reprojected the data onto a common grid (with a grid spacing of 0.008º or ~1km at the equator) to calculate the annual averages for each overpass time.

In addition, we used forest cover data from the University of Maryland Global Forest Cover (GFC) dataset (Hansen et al., 2013). The GFC data were derived from 30m-resolution Landsat imagery, which is used to provide both the percent of land covered by forest in 2000 and the year in which a deforestation event occurred. We resampled the GFC data and reprojected it onto the same grid as the MODIS data by taking the percent of forested GFC pixels within a

given MODIS grid box each year to obtain the annual forest cover at 1km spatial resolution for the entire Southeast Asia region (**Figure 3.1**). Pixels where the European Council Joint Research Center (EC JRC) Global Surface Water (GSW) water occurrence (Pekel et al. 2016) was greater than 1% were excluded. By comparing year-to-year differences in forest cover for a given pixel, the forest loss could then be determined and deforestation events could be identified.

A2.1.2 "Difference-in-differences" statistical analysis

In order to understand the impact of deforestation on cloud properties, we needed to separate changes driven by the forest loss itself from changes driven by other sources of interannual variability using the "difference-in-differences" method (Crompton et al., 2021). First, across the two decades of data examined here, we identified any pixels which had undergone a deforestation event, defined as a >50% loss in forest cover from one year to the next. This definition intentionally excludes gradual changes in forest cover and focuses the analysis on dramatic changes in forest cover that are most likely to impact the cloud field on an annual timescale. It should also be noted that the changes in the cloud field are only considered in the years directly before and after the deforestation event (i.e., a given pixel can only be deforested one time), and thus exclude potential impacts from forest regrowth. Deforested pixels and any pixel within a 10km radius from them (**Figure A2.1**) were defined as *assessment pixels* that may potentially experience deforestation-driven changes in cloud properties. Such a change in a cloud property C for an assessment pixel during the year t is given by:

$$\Delta C_{assessment} = C_{assessment,t+1} - C_{assessment,t-1}$$

which is the temporal change in the given cloud property across the year before and after the deforestation event. We tested the sensitivity of these results to varying the radius for

defining an assessment pixel between 10 and 25km and found there were no qualitative changes in our results.

Secondly, for each assessment pixel, we identified a matching set of *control pixels* that experienced similar synoptic weather forcing as the assessment pixel but did not directly experience the effects of deforestation. Control pixels were between 10-25km from a deforested pixel (i.e., not assessment pixels) and consisted of intact forest (>90% forest cover remaining and <2% accumulated forest loss since 2000). We tested the sensitivity of these results to varying distance definitions (up to 5km closer or further) and found there were no qualitative changes in our results. For the same deforestation event described above, the corresponding change in C for a control pixel is similarly written as:

$$\Delta C_{control} = C_{control,t+1} - C_{control,t-1}$$

Thirdly, we calculated the deforestation-induced changes in the cloud field. Both the control and assessment pixels will have similar changes in C driven by large-scale interannual variability since they are in close proximity, but only the assessment pixels will have a change in C driven by deforestation. The effect of deforestation ε is thus given by the "difference-in-differences":

$$\varepsilon = \Delta C_{assessment} - \Delta C_{control}$$

which we use as a metric of deforestation impacts on cloud properties.

Finally, we aggregated the millions of qualifying pixels across the entire region and time period as a function of forest loss. The pixels were aligned in time relative to the year in which the deforestation event took place. There were no significant trends in the cloud response to deforestation across the different sample years (**Figure A2.2**). As the mean forest loss within a 1km radius of an assessment point increases (i.e., as its surface properties becomes more

different from the control points), we would expect a magnification in the cloud response if these changes are being driven in a monotonic way by the deforestation itself. We calculated the mean forest loss within a 1km radius of each assessment pixel and grouped the pixels into 10 forest loss bins (ranging from 0 or no forest loss to 1 or total forest loss). The number of points in each forest loss bin are shown in **Figure A2.3**. Since each bin has a different population size, to sample equally across different forest losses, we calculated the bootstrapped estimate (sample size of 100 repeated 5000 times) of the mean and the 25th and 75th percentile confidence intervals.

A2.1.3 Environmental analysis

To explore the environmental modulation of land-convection interactions, we further calculated the deforestation effect on cloud properties for different environmental subgroups. Specifically, we contrasted the impacts of high versus low precipitable water (PWAT) and aerosol optical depth (AOD). For each assessment point, we represented the nearby environment by calculating the mean value of PWAT and AOD within a 10km radius in the year that the deforestation event occurred. We tested the sensitivity of our results to other averaging radii (1km, 5km, and 10km) and other time periods (during the year of the deforestation event, the year prior, the year after, and the mean across all three years) for defining the environmental parameters, and found the trends presented in this study are not sensitive to the averaging radii or time period.

Once these environmental parameters were calculated for each assessment pixel, we divided them according to their percentile values across all assessment pixels for the entire time period. In doing so, we separated the “low” and “high” categories of each environmental variable

by taking the bottom and top quartiles, respectively. We then repeated the difference-in-differences calculation for the low and high categories separately.

A2.2 Supplemental figures

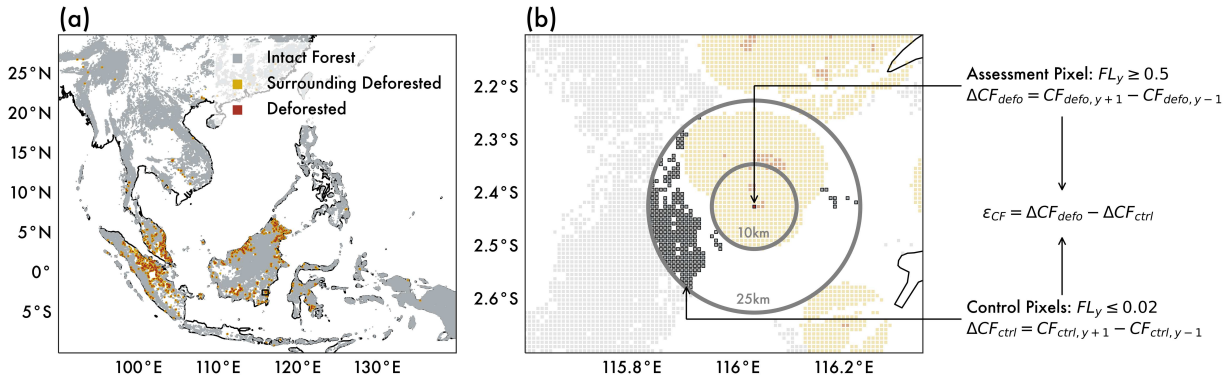

Figure A2.1. Illustration of the "difference-in-differences" method for year 2004. (a) shows all forest pixels. Gray pixels are the potential control sample, defined as intact forest points (with total prior forest loss, FL2000-2004<0.02) that are more than 10km away from a deforested point. Red pixels are deforested areas (FL2004>0.5). Yellow pixels are those which do not satisfy the deforestation criteria but are less than 10km from a point which does. Together, the "deforested" and "surrounding deforested" pixels make up the assessment points. (b) shows a closer view of the boxed region in (a) along the southeast coast of Borneo, with a single assessment pixel and corresponding control pixels highlighted in black outline. The gray range circles show the definition of the control pixels as being between 10 and 25km from the assessment pixel they are controlling for. The calculation of epsilon (deforestation effect) is described by the inset equations.

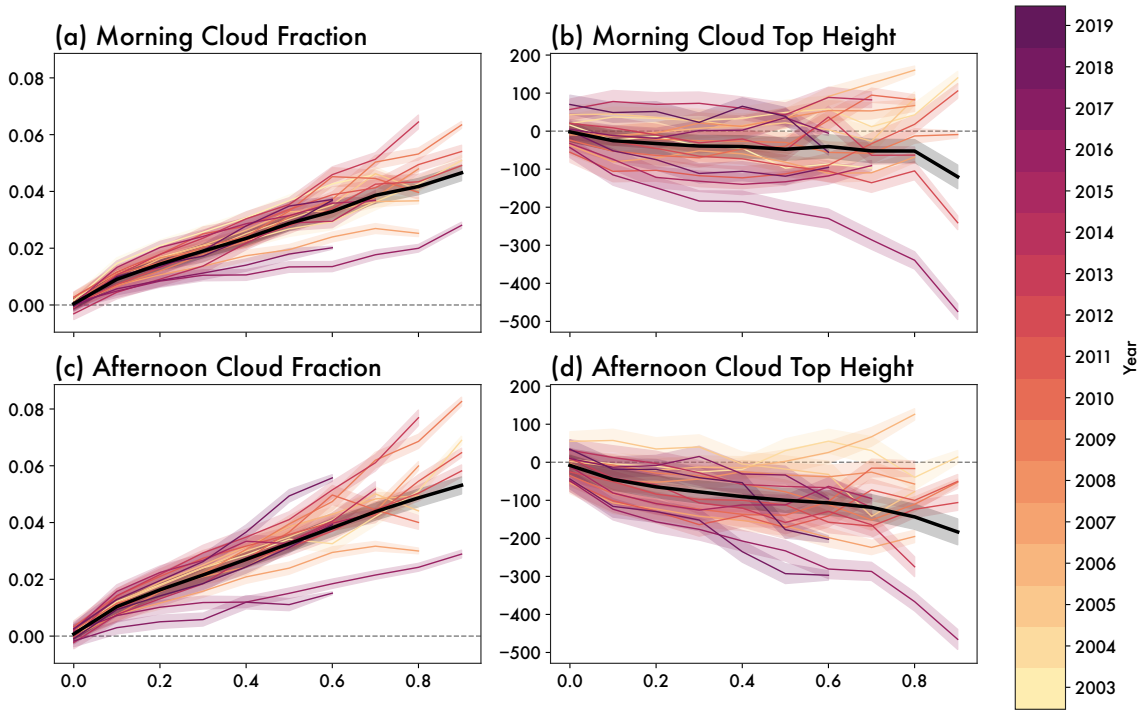

Figure A2.2. Estimated cloud response (ε) to mean forest loss within a 1km radius for the annual mean (a,c) cloud fraction and (b,d) cloud top height (m). (a,b) show the Terra daytime overpasses (10:30AM) and (c,d) show the Aqua daytime overpasses (1:30PM). Black lines indicate the mean response over the full time period, identical to Figure 3.2. Colored lines are the response estimated separately for each year. Solid lines indicate the bootstrapped estimate of the mean (n=1000) and shaded areas span the 25th to 75th percent confidence interval.

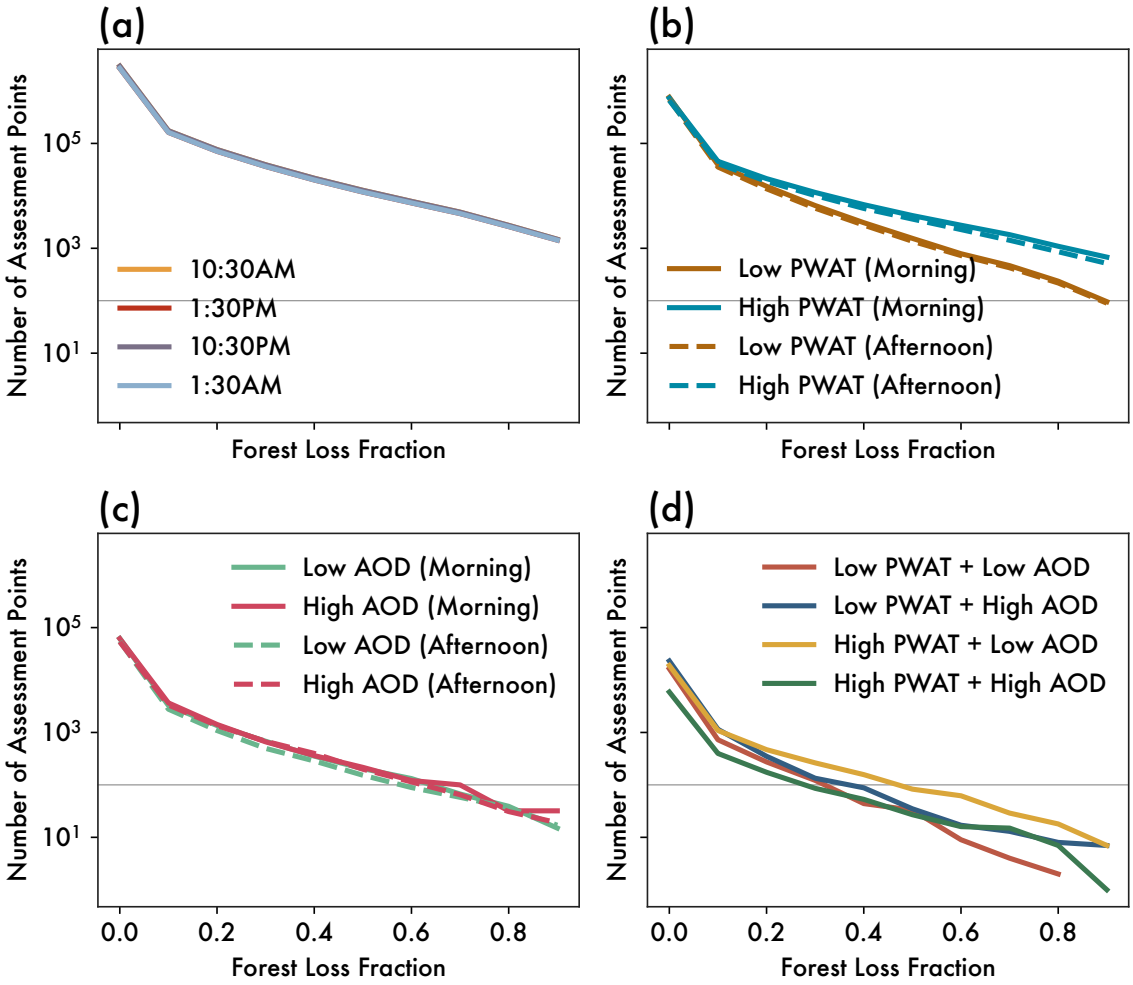

Figure A2.3. Population size of each forest loss bin, where the population size is the total number of assessment points falling into each bin. (a), (b), and (c) show the population size corresponding to Figures 3.2, 3.3, and 3.4, respectively. (d) shows the population size of the cross-terms between PWAT and AOD quartiles. The horizontal gray line shows the cut-off range of n=100; if there are less than 100 points in the bin, we do not include these trends in our analysis for statistical robustness.

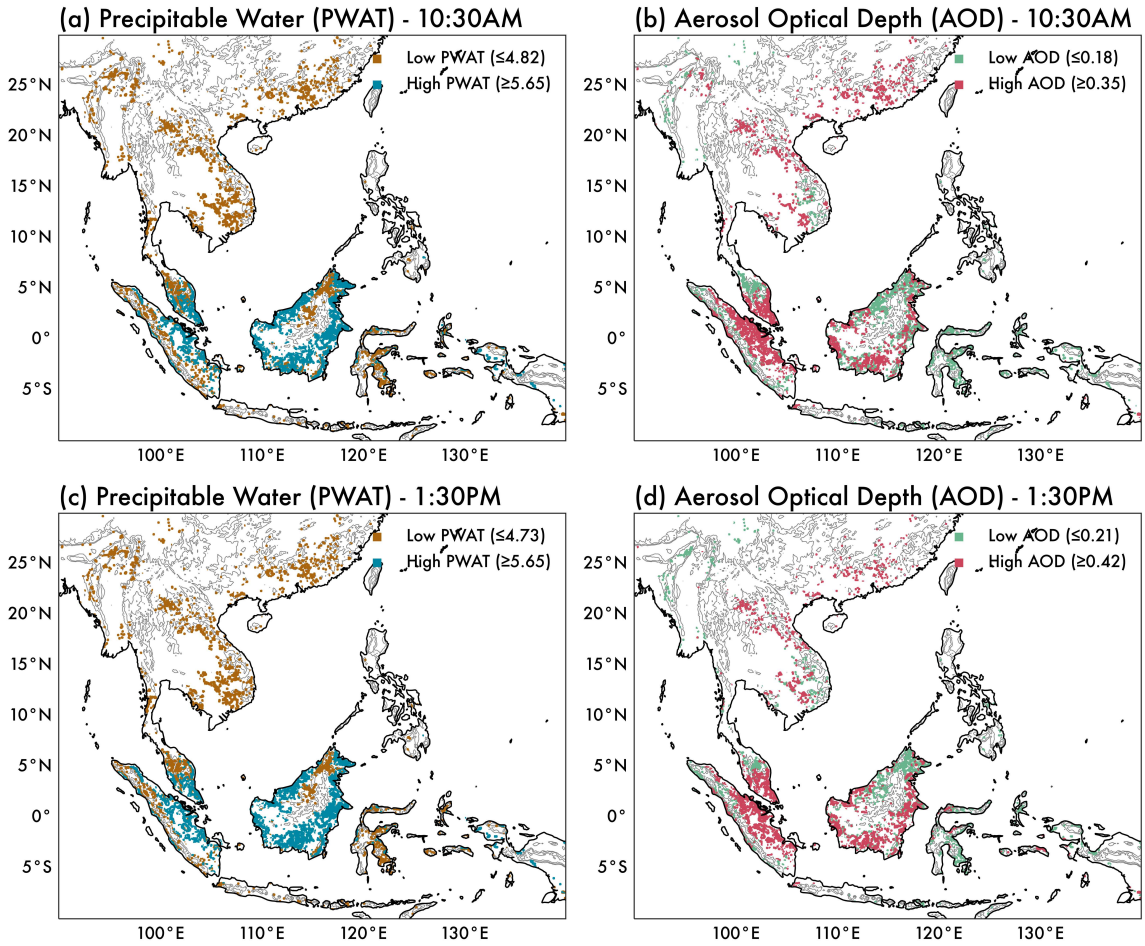

Figure A2.4. Spatial distribution of environmental parameters tested in the study. Spatial distribution of points assigned to the low/high (a,c) precipitable water (PWAT) and (b,d) aerosol optical depth (AOD) quartiles. (a,b) show the Terra daytime overpasses (10:30AM) and (c,d) show the Aqua daytime overpasses (1:30PM). Gray contours indicate elevations of 500, 1000, and 2000 m ASL to show topography.

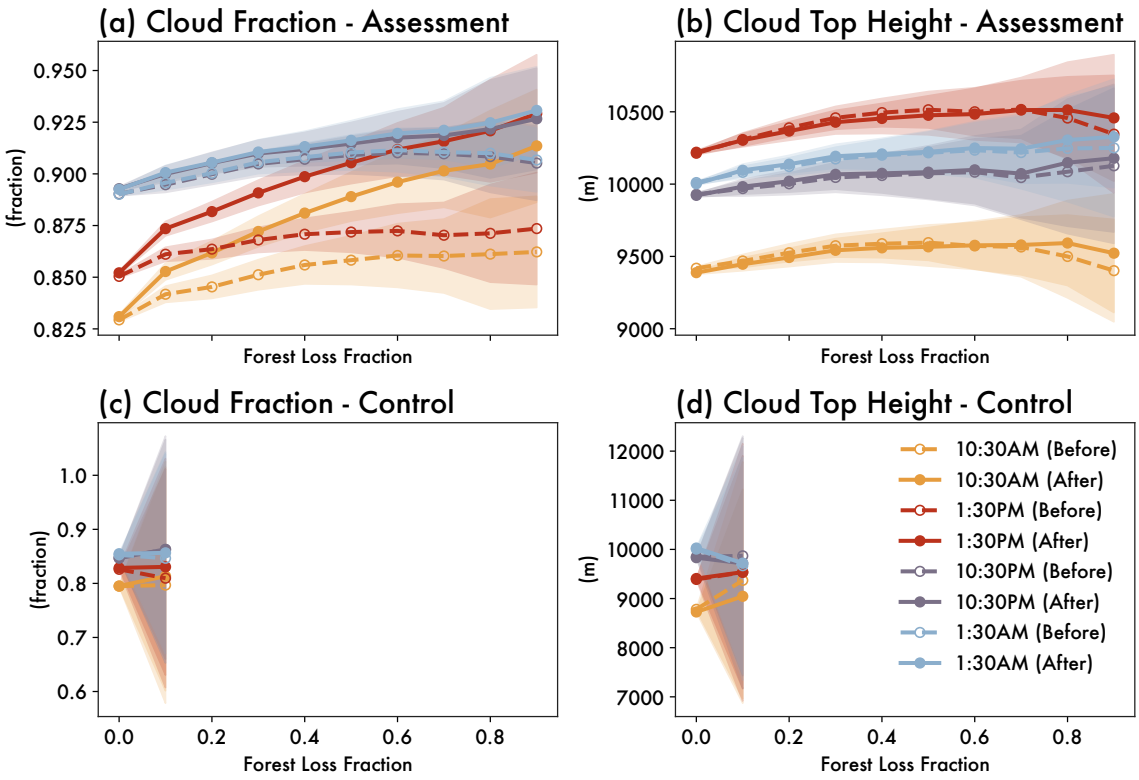

Figure A2.5. Absolute magnitude of (a,c) cloud fraction and (b,d) cloud top height as a function of mean forest loss within a 1km radius. (a-b) represent the full set of assessment pixels (as described in Section A.1) and (c-d) represent the full set of control pixels. Solid lines correspond to the years prior to forest loss occurring, while dashed lines correspond to the years following forest loss. Dark lines represent the mean value, while shaded area represents the 25th to 75th percentile values.